THE INFLUENCE OF REGCM4 LATERAL BOUNDARY SCHEMES ON EAST AFRICAN RAINFALL

BY

TAMENE MEKONNEN

SUBMITTED IN PARTIAL FULFILLMENT OF THE
REQUIREMENTS FOR THE DEGREE OF
MASTER OF SCIENCE
IN ATMOSPHERIC

PHYSICS

AT

ADDIS ABABA UNIVERSITY

ADDIS ABABA, ETHIOPIA

June 2012

ADDIS ABABA UNIVERSITY
DEPARTMENT OF
PHYSICS

Supervisor: _____
Dr. Gizaw Mengistu

Examiners: _____
Dr. Lemi Demeyou

_____
Dr. Elias Lewi

ADDIS ABABA UNIVERSITY

Date: **JUNE 2012**

Author: **TAMENE MEKONNEN**

Title: **THE INFLUENCE OF REGCM4 LATERAL BOUNDARY SCHEMES ON EAST AFRICAN RAINFALL**

Department: **Physics**

Degree: **M.Sc.** Convocation: **June** Year: **2012**

Abstract

The latest version of the International Center for Theoretical Physics (ICTP) Regional climate model version 4 (RegCM4) is used to study the influences of five different Lateral Boundary Schemes (LBSs) on the simulated rainfall for a period of 20 years. The rainfall from RegCM4 simulations under the five LBSs are compared with the observed rainfall in Climate Research Unit (CRU) and Global Precipitation Climatology Project (GPCP) dataset. The spatial domain encompasses the whole continental Africa and includes the Indian and south Atlantic ocean basins to capture the major circulation features dominating eastern Africa. The comparison of the model results of rainfall with observations from CRU and GPCP indicates a wet bias over east African highlands while a dry bias is observed over the east African lowlands for all cases. The mean annual cycle of rainfall is well captured over east African subregions for each LBSs. The mean annual cycle also indicates that some part of the east African countries are characterized by bimodal rainfall trend which is well captured by all simulations. The observed precipitation inter-annual variability is well reproduced by the regional model over most regions, although RegCM4 simulations show some deficiencies. It is found that the use of sponge as well as the exponential LBSs reproduces realistic rainfall as exhibited by good agreement with GPCP and CRU rainfall.

I would like to dedicate this thesis to **MCD**

Acknowledgements

And I am grateful to my advisor Dr. Gizaw Mengistu for his unlimited and helpful suggestions and valuable discussions during the study as well as for his computer support to accomplish this work. With out his restless effort the thesis should not be completed timely.

Contents

List of Figures

List of Tables

List of Acronyms

BATS Biosphere-Atmosphere Transfer Scheme

BATS1e Biosphere-Atmosphere Transfer Scheme version 1e

CCM Community Climate Model

CCM1 Community Climate Model version 1

CCM2 Community Climate Model version 2

CCM3 Community Climate Model version 3

CRU Climate Research Unit

DJF December, January, and February

ECMWF European Center for Medium-Range Weather Forecasts

ERAIN ERA-interim Reanalysis

ERA40 ECMWF 40-year Reanalysis

GCM General Circulation Model

GPCP Global Precipitation climatology Project

ICBC Initial and Boundary Condition

ICTP Abdus Salam International Center for Theoretical Physics

ITCZ Inter-tropical convergence zone

JJA June, July, and August

LAMs Limited area models

LBCs Lateral boundary conditions

LBSs Lateral boundary Schemes

MAM March, April, and May

MM4 Mesoscale Model version 4

MM5 Mesoscale Model version 5

NNRP2 NCEP/NCAR Reanalysis Product version 2

NCAR National Center for Atmospheric Research

NCEP National Centers for Environmental Prediction

OISST Optimum interpolation SST

PBL Planetary boundary layer

PSU Pennsylvania State University

RCM Regional Climate Model

RegCM2 REGional Climate Model version 2

RegCM3 REGional Climate Model version 3

RegCM4 REGional Climate Model version 4

SIMEX Simple EXplicit moisture scheme

SON September, October, and November

SST Sea surface temperature

SUBEX SUB-grid EXplicit moisture scheme

USGS United States Geological Survey

Chapter 1

Introduction

Regional climate models (RCMs) have been widely used as a dynamical downscaling tools to study regional climate processes, regional climate changes and impacts for prediction of seasonal climate variability (Sylla *et al.*, 2009; Anyah & Semazzi, 2007). RCMs are used to increase our understanding of mesoscale and regional-scale climate processes that play great role in shaping the atmospheric response to surface and lateral boundary forcing (Segele *et al.*, 2008) that do not resolved with the help of coarse horizontal resolution General Circulation models(GCMs).

Rainfall is the most driving factor of climate in the tropics and needs to be properly represented within a climate model (Davis *et al.*, 2009). However, relatively few studies on rainfall climatologies have focused on the African continent, especially on East Africa. East Africa is characterized by complex topographical variation and marked gradients of vegetation and land-cover (Sylla *et al.*, 2009). Land cover influences surface climate, both through biophysical interactions that affect surface energy balance due to the influences exerted by both human-dominated and natural landscapes and through biogeochemical interactions that affect the carbon cycle (Diffenbaugh, 2009). East Africa is also covered by a variety regions known for their unreliable rainfall which has a large impact on the spatial climate variability that is mainly associated with the occurrence of mesoscale convective systems and with the forcing of mountain complexes. The temporal variability may be seen as a modulation of the seasonal cycle linked to the meridional displacement of the rain belt associated with the Inter-tropical Convergence Zone (ITCZ) and the African monsoon (Bowden & Semazzi, 2007). The ITCZ , which is the region of low pressure where the northeasterly and southeasterly trade winds coverage, is a primary driver of

the seasonal cycle of rainfall over eastern Africa and is mainly responsible for the distinct bimodal rainfall seasons over the region (Anyah & Semazzi, 2007).

Davis *et al.* (2009) performed customization of RegCM3 simulations using Grell with closures Arakawa-Schubert (Grell-AS)/Fritch-Chappel (Grell-FC) and Massachusetts Institute of Technology-Emanuel (MIT-EMAN) convective schemes over eastern Africa and a tropical Indian ocean domain with particular focus on precipitation fields and to investigate the physical processes responsible for the changes in model output. They found that the model underestimates total precipitation throughout the area average regions for Grell-AS and overestimates for MIT-EMAN by large dry and wet biases respectively where as Grell-FC show moderate overestimation rainfall in Kenya and Tanzania and underestimation elsewhere. Gianotti *et al.* (2012) also performed an other RegCM3 simulations over the Maritime Continent using different cumulus parameterization and land surface schemes. Gianotti *et al.* (2012) found that Grell-FC is the best in performing the convection schemes, having the smallest error magnitudes in both the rainfall histogram and average diurnal cycle, and also having good representation of the land surface energy and evapotranspiration components.

Gianotti *et al.* (2012) also analysed the dependency of rainfall on the choice of lateral boundary conditions using the 40-years European Center for Medium-Range Weather Forecasts (ECMWF) Re-Analysis (ERA-40) dataset and NCEP/NCAR Reanalysis Product version 2 (NNRP2). They found ERA-40 to produce better simulations of observed rainfall when used as lateral boundary conditions than NNRP2. While Sylla *et al.* (2009) performed a multiyear simulation of the African climate using a regional climate model (RegCM3) over a large African domain encompassing the entire African continent and adjacent ocean water using the high resolution ERA-interim reanalysis that corrects some of the errors of the ERA-40 reanalysis, particularly in the hydrologic cycle variables over the tropics. They found a relatively good performance of the RegCM3 over such large domain indicating that part of this relatively good performance is due to the use of ERA-interim to produce improved lateral boundary conditions.

The treatment of different lateral boundary schemes (LBSs) is an intrinsic and distinctive problem associated with the formulation of regional weather prediction models (Davies, 1983). The problems on the issue of how to treat the lateral boundary schemes when computing within limited domains has received a great deal of attention (Lavelle & Thacker, 2008). Information from outside the computational domain essential to the

solution must be allowed to enter, and what should leave the domain must be allowed to depart from the computational domain without reflection back from the artificial boundary. This implies that large-scale atmospheric conditions must be provided to a regional climate model (RCM), and that spurious interactions between the model solution and the lateral boundaries must be avoided (Marbaix *et al.*, 2003).

This paper focuses on different statistics (mean climatology, mean seasonal and annual cycle, and inter-annual variability) to determine the influence of RegCM4 lateral boundary schemes (LBSs) on the relevant features of east African rainfall climatology. The mean and mean seasonal cycles of rainfall climatologies are examined over the entire domain based on the spatial distribution and bias from the observations, where as the annual and inter-annual rainfall variability is examined over different sub-regions of east Africa. The performance of the RegCM4 lateral boundary condition schemes over different east African sub-regions for inter-annual rainfall variability is examined quantitatively by analysing the correlation, bias, and root mean square error (RMSE) of the simulations for each LBSs relative to observations.

The main objective of this study is to evaluate the influence of forcing fields from different Lateral Boundary Schemes (LBSs) on the performance of the International Center for Theoretical Physics (ICTP) regional climate model version 4 (RegCM4) in reproducing the observed rainfall climatologies over east Africa.

The specific objectives of the study are: (1) to find out LBS that best reproduces the east African rainfall climatology over the large east African domain; (2) to examine the influence of the LBSs on the circulation system of east Africa rainfall climatology; (3) to examine the east African climate variability; (4) for further study on climate projection over east Africa using the best LBS that reproduce the observed rainfall climatology very well.

In order to achieve the above general objective and listed specific objectives, the results obtained from RegCM4 simulations for different LBSs has been compared with observed data from the Climate Research Unit (CRU) rainfall data which is a high resolution rainfall data with 0.5^o latitude-longitude grid spacing (Tchotchou & Kamga, 2009) and Global Precipitation climatology Project (GPCP) with 2.5^o latitude-longitude grid spacing (Adler *et al.*, 2003; Huffman *et al.*, 2009). The analysis is integrated for a period of 20 years from 1989-2008. The period of simulation was chosen in order to connect the present climate to the future for climate projection.

The general descriptions of the atmospheric dynamical equations of basic conservation laws of mas, momentum, and energy is presented in chapter 2. The implementation of dynamical and physical core model equation of RegCM4 is given in chapter 3 where as the regional model description, experimental design and configuration of model simulations and methodology used to examine the influences of different LBSs on east African rainfall climatology is given in chapter 4. The data analysis is presented in chapter 5 and followed by conclusion in chapter 6.

Chapter 2

Atmospheric Dynamics

This chapter describes the fundamental dynamical equations that govern the atmospheric circulation system mainly the basic governing model equations for RegCM4.

2.1 Basic Conservation Laws

The Atmosphere is governed by fundamental physical principles of conservation laws. These are:

1. Conservation of mass,
2. Conservation of momentum, and
3. Conservation of energy.

The mathematical relations that express these laws may be derived by considering the budgets of mass, momentum, and energy for an infinitesimal control volume in the fluid. Two types of control volume are commonly used in fluid dynamics: the **Eulerian** and **Lagrangian** (see Holton, 2004 and Jacobson, 2005).

In the **Eulerian frame of reference**, the control volume consists of a parallelepiped of sides δx, δy, δz, whose position is fixed relative to the coordinate axes. Mass, momentum, and energy budgets will depend on fluxes caused by the flow of fluid through the boundaries of the control volume.

In the **Lagrangian frame**, however, the control volume consists of an infinitesimal mass of tagged fluid particles. Thus, the control volume moves following the motion of the fluid, always containing the same fluid particles.

The Lagrangian frame is particularly useful for deriving conservation laws, as such laws may be stated most simply in terms of a particular mass element of the fluid. The Eulerian system is, however, more convenient for solving most problems because in that system the field variables are related by a set of partial differential equations in which the independent variables are the coordinates x, y, z, and t.

In the Lagrangian system, however, it is necessary to follow the time evolution of the fields for various individual fluid parcels. Thus the independent variables are x_0, y_0, z_0 and t, where x_0, y_0 and z_0 are the position that a particular parcel passed through at a reference time t_0 .

2.2 Conservation of Mass

The principle of conservation of mass simply states that the mass of a closed system remains constant. This applies to all closed systems for which no mass is created or destroyed. The same principle can applied to an open system that may be stated as, the net mass flux into the system equals the rate of increase of mass of the system.

2.2.1 The Continuity Equation

The mathematical relationship that expresses conservation of mass for a fluid is called the continuity equation. This section develops the continuity equation using both an Eulerian and Lagrangian control volume.

2.2.2 An Eulerian Derivation

Considering an Eulerian volume element with sides δx, δy, and δz that is fixed in a Cartesian coordinate frame as shown in Fig 2.1. For such a fixed control volume the net rate of mass inflow through the sides must equal the rate of accumulation of mass within the volume. The rate of inflow of mass through the left-hand face per unit area is

$$[\rho u - \frac{\partial}{\partial x}(\rho u)\frac{\delta x}{2}], \tag{2.1}$$

whereas the rate of outflow per unit area through the right-hand face is

$$[\rho u + \frac{\partial}{\partial x}(\rho u)\frac{\delta x}{2}], \tag{2.2}$$

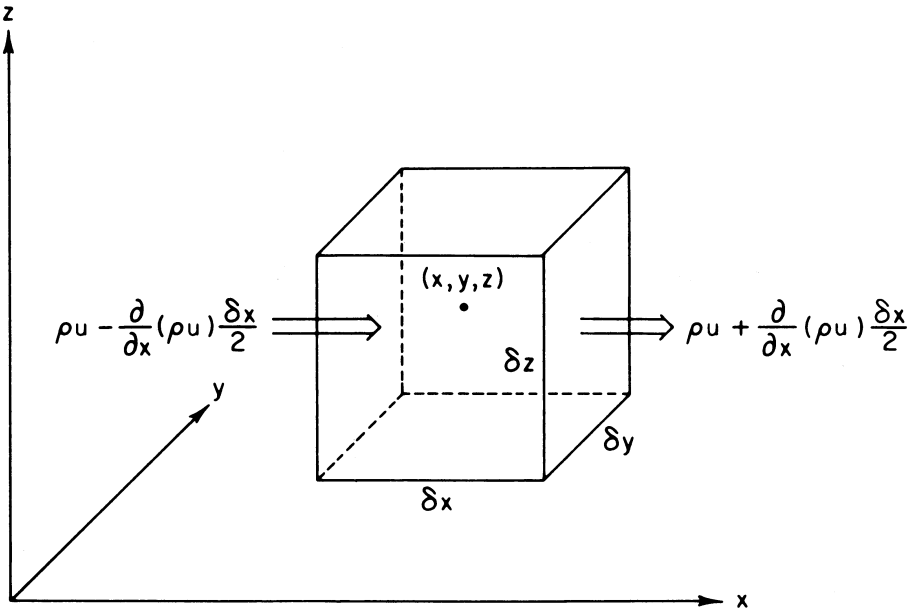

Figure 2.1: Mass inflow into a fixed (Eulerian) control volume due to motion parallel to the x axis.

Because the area of each of these faces is $\delta y \delta z$, the net rate of flow into the volume due to the x velocity component is

$$[\rho u - \frac{\partial}{\partial x}(\rho u)\frac{\delta x}{2}]\delta y \delta z - [\rho u + \frac{\partial}{\partial x}(\rho u)\frac{\delta x}{2}]\delta y \delta z = -\frac{\partial}{\partial x}(\rho u)\delta x \delta y \delta z \tag{2.3}$$

Similar expressions obviously hold for the y and z directions. Thus, the net rate of mass inflow is

$$-[\frac{\partial}{\partial x}(\rho u) + \frac{\partial}{\partial y}(\rho v) + \frac{\partial}{\partial z}(\rho w)]\delta x \delta y \delta z \tag{2.4}$$

where u , v and w are the velocity components along x , y and z respectively.

The mass inflow per unit volume (-$\nabla \cdot (\rho \mathbf{U})$) must equal the rate of mass increase per unit volume and $\mathbf{U} = \mathbf{i}u + \mathbf{j}v + \mathbf{k}w$. Now the increase of mass per unit volume is just the local density change $\partial\rho/\partial t$. Therefore,

$$\frac{\partial \rho}{\partial t} + \nabla \cdot (\rho \mathbf{U}) = 0 \tag{2.5}$$

Equation(2.5) is the mass divergence form of the continuity equation. An alternative form of the continuity equation is obtained by applying the vector identity ($\nabla \cdot (\rho \mathbf{U}) = \rho\nabla\cdot\mathbf{U}+\mathbf{U}\cdot\nabla\rho$) on the divergence term in Equation(2.5) and the relationship $\frac{d}{dt} \equiv \frac{\partial}{\partial t}+\mathbf{U}\cdot\nabla$ which is given by:

$$\frac{\partial \rho}{\partial t} = -\rho(\nabla \cdot \mathbf{U}) - (\mathbf{U} \cdot \nabla)\rho \tag{2.6}$$

Equation (2.6) is the continuity equation for total air mass density. $\mathbf{U}$ can be also decomposed into the horizontal and vertical wind components $\mathbf{V}_h$ and $\mathbf{V}_v$ respectively as $\mathbf{U} = \mathbf{V}_h + \mathbf{V}_v$. Thus equation (2.6) becomes

$$\left(\frac{\partial \rho}{\partial t}\right)_z = -\rho(\nabla_z \cdot \mathbf{V}_h + \frac{\partial \mathbf{V}_v}{\partial z}) - (\mathbf{V}_h \cdot \nabla_z)\rho - \mathbf{V}_v \frac{\partial \rho}{\partial z} \tag{2.7}$$

where $\mathbf{V}_h = \mathbf{i}u + \mathbf{j}v$ and $\mathbf{V}_v = \mathbf{k}w$ are the horizontal and vertical wind components respectively.

Applying the conversion from altitude to pressure coordinate ($\nabla_z = \nabla_p + \nabla_z p \frac{\partial}{\partial p}$) to the horizontal wind component $\mathbf{V}_h$,

$$\nabla_z \cdot \mathbf{V}_h = \nabla_p \cdot \mathbf{V}_h + \nabla_z p \frac{\partial \mathbf{V}_h}{\partial p} \tag{2.8}$$

Substituting equation (2.8) into equation (2.7) and using hydrostatic equation ($dz = \frac{-dp}{\rho g}$), the continuity equation becomes

$$\left(\frac{\partial \rho}{\partial t}\right)_z = -\rho \left(\nabla_p \cdot \mathbf{V}_h + \nabla_z(p)\frac{\partial \mathbf{V}_h}{\partial p}\right) - (\mathbf{V}_h \cdot \nabla_z)\rho + \rho g \frac{\partial w\rho}{\partial p} \tag{2.9}$$

Using the partial derivative of the vertical velocity component ($w_p = dp/dt$) in pressure coordinate and substituting the hydrostatic equation throughout, which gives

$$\rho \frac{\partial w_p}{\partial p} = \left(\frac{\partial \rho}{\partial t}\right)_z + \rho \nabla_z(p) \cdot \frac{\partial \mathbf{V}_h}{\partial p} + (\mathbf{V}_h \cdot \nabla_z)\rho - \rho g \frac{\partial (w\rho)}{\partial p} \tag{2.10}$$

Adding equations (2.9) and (2.10), the continuity equation for air in Cartesian-pressure coordinates rewritten as;

$$\nabla_p \cdot \mathbf{V}_h + \frac{\partial w_p}{\partial p} = 0 \tag{2.11}$$

Applying the gradient conversion from pressure to sigma coordinate ($\nabla_p = \nabla_\sigma - \frac{\sigma}{p^*}\nabla_\sigma(p^*)\frac{\partial}{\partial \sigma}$) and $\frac{\partial p}{\partial \sigma} = p^*$ to equation (2.11);

$$\nabla_\sigma \cdot \mathbf{V}_h - \frac{\sigma}{p^*}\nabla_\sigma(p^*)\frac{\partial \mathbf{V}_h}{\partial \sigma} + \frac{1}{p^*}\frac{\partial w_p}{\partial \sigma} = 0 \tag{2.12}$$

But

$$\frac{\partial w_p}{\partial \sigma} = \left(\frac{\partial p^*}{\partial t}\right)_\sigma + (\mathbf{V}_h \cdot \nabla_\sigma)p^* + \sigma \nabla_\sigma (p^*) \cdot \frac{\partial \mathbf{V}_h}{\partial \sigma} + p^* \frac{\partial \dot{\sigma}}{\partial \sigma} \tag{2.13}$$

Substituting equation (2.13) into equation (2.12) and rearranging,

$$\left(\frac{\partial p^*}{\partial t}\right)_\sigma = -\nabla_\sigma \cdot (\mathbf{V}_h p^*) - p^* \frac{\partial \dot{\sigma}}{\partial \sigma} \tag{2.14}$$

Expanding the divergence term in equation (2.14),

$$\left(\frac{\partial p^*}{\partial t}\right)_\sigma = -\left(\frac{\partial u p^*}{\partial x} + \frac{\partial v p^*}{\partial y}\right) - p^* \frac{\partial \dot{\sigma}}{\partial \sigma} \tag{2.15}$$

This is the required form of continuity equation in sigma(σ) coordinates.

2.2.3 A Lagrangian Derivation

The physical meaning of divergence can be illustrated by the following alternative derivation of equation (2.8). Consider a control volume of fixed mass M that moves with the fluid. Letting $\delta \mathrm{V} = \delta \mathrm{x} \delta \mathrm{y} \delta \mathrm{z}$ be the volume and $\delta \mathrm{M} = \rho \delta \mathrm{V} = \rho \delta \mathrm{x} \delta \mathrm{y} \delta \mathrm{z}$ is conserved following the motion;

$$\frac{1}{\delta M}\frac{d}{dt}(\delta M) = \frac{1}{\rho \delta V}\frac{d}{dt}(\rho \delta V) = \frac{1}{\rho}\frac{d\rho}{dt} + \frac{1}{\delta V}\frac{d}{dt}(\delta V) = 0 \tag{2.16}$$

but

$$\frac{1}{\delta V}\frac{d}{dt}(\delta V) = \frac{1}{\delta x}\frac{d}{dt}(\delta x) + \frac{1}{\delta y}\frac{d}{dt}(\delta y) + \frac{1}{\delta z}\frac{d}{dt}(\delta z) \tag{2.17}$$

Referring to Fig. (2.2), the faces of the control volume in the y and z plane (designated A and B) are advected with the flow in the x direction at speeds $u_A = \frac{dx}{dt}$ and $u_B = \frac{d(x+\delta x)}{dt}$, respectively. Thus, the difference in speeds of the two faces is $\delta u = u_B - u_A = \frac{d(x+\delta x)}{dt} - \frac{dx}{dt}$ or $\delta u = \frac{d(\delta x)}{dt}$. Similarly, $\delta v = \frac{d(\delta y)}{dt}$ and $\delta w = \frac{d(\delta z)}{dt}$. Therefore,

$$\lim_{\delta x, \delta y, \delta z \to 0} [\frac{1}{\delta V}\frac{d}{dt}(\delta V)] = \frac{\partial u}{\partial x} + \frac{\partial v}{\partial y} + \frac{\partial w}{\partial z} = \nabla \cdot \mathbf{U} \tag{2.18}$$

So that in the limit $\delta V \to 0$, equation (2.16) reduces to the continuity equation (2.5). The divergence of the three-dimensional velocity field is equal to the fractional rate of change of volume of a fluid parcel in the limit $\delta V \to 0$.

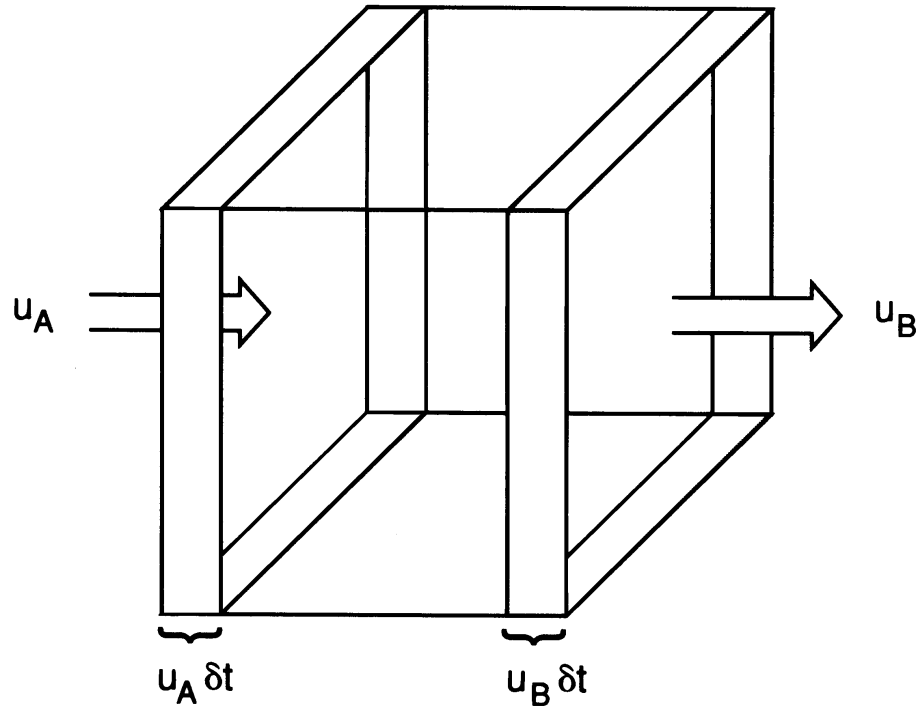

Figure 2.2: Change in Lagrangian control volume (shown by shading) due to fluid motion parallel to the x axis.

2.3 Conservation of Momentum

Newton's second law of motion (in an inertial reference frame) may be written symbolically as

$$\frac{d_a \mathbf{U}_a}{dt} = \sum \mathbf{F} \tag{2.19}$$

The left-hand side represents the rate of change of the absolute velocity $\mathbf{U}_a$, following the motion as viewed in an inertial system. The right-hand side represents the sum of the real forces acting per unit mass. When the motion is viewed in a rotating coordinate system certain additional apparent forces must be included if Newton's second law is to be valid. The same result may be obtained by a formal transformation of coordinates in (2.19).

In order to transform this expression to rotating coordinates, first find a relationship between $\mathbf{U}_a$ and the velocity relative to the rotating system $\mathbf{U}$. This relationship is obtained by applying the total derivative to the position vector $\mathbf{r}$ for an air parcel on the

rotating earth:

$$\frac{d_a\mathbf{r}}{dt} = \frac{d\mathbf{r}}{dt} + \boldsymbol{\Omega} \times \mathbf{r} \tag{2.20}$$

but $d_a\mathbf{r}/dt \equiv U_a$, $d\mathbf{r}/dt \equiv \mathbf{U}$, and $\boldsymbol{\Omega}$ is angular velocity. Therefore (2.20) may be written as

$$\mathbf{U}_a = \mathbf{U} + \Omega \times \mathbf{r} \tag{2.21}$$

which states simply that the absolute velocity of an object on the rotating earth is equal to its velocity relative to the earth plus the velocity due to the rotation of the earth. Now applying (2.20) to the velocity vector $\mathbf{U}_a$,

$$\frac{d_a\mathbf{U}_a}{dt} = \frac{d\mathbf{U}_a}{dt} + \boldsymbol{\Omega} \times \mathbf{U}_a \tag{2.22}$$

Substituting from (2.21) into the right-hand side of (2.22) gives

$$\frac{d_a\mathbf{U}_a}{dt} = \frac{d}{dt}(\mathbf{U} + \boldsymbol{\Omega} \times \mathbf{r}) + \boldsymbol{\Omega} \times (\mathbf{U} + \boldsymbol{\Omega} \times \mathbf{r}) = \frac{d\mathbf{U}}{dt} + 2\boldsymbol{\Omega} \times \mathbf{U} - \Omega^2\mathbf{R} \tag{2.23}$$

where Ω is assumed to be constant. Here $\mathbf{R}$ is a vector perpendicular to the axis of rotation, with magnitude equal to the distance to the axis of rotation, so that with the aid of a vector identity,

$$\boldsymbol{\Omega} \times (\boldsymbol{\Omega} \times \mathbf{r}) = \boldsymbol{\Omega} \times (\boldsymbol{\Omega} \times \mathbf{R}) = -\Omega^2\mathbf{R} \tag{2.24}$$

Equation (2.23) states that the acceleration following the motion in an inertial system equals the rate of change of relative velocity following the relative motion in the rotating frame plus the Coriolis acceleration due to relative motion in the rotating frame plus the centripetal acceleration caused by the rotation of the coordinates. If one assume that the only real forces acting on the atmosphere are the pressure gradient force, gravitation, and friction, then Newton's second law (2.19) can be rewritten with the aid of (2.23) as

$$\frac{d\mathbf{U}}{dt} = -2\boldsymbol{\Omega} \times \mathbf{U} - \frac{1}{\rho}\nabla p + \mathbf{g} + \mathbf{F}_r \tag{2.25}$$

where $\mathbf{F}_r$ designates the frictional force, and the centrifugal force has been combined with gravitation in the gravity term $\mathbf{g}$. Equation (2.25), which is the vectorial form of momentum equation, is the statement of Newton's second law for motion relative to a rotating coordinate frame. It states that the acceleration following the relative motion in the rotating frame equals the sum of the Coriolis force, the pressure gradient force,

effective gravity, and friction. This form of the momentum equation is basic to most work in dynamic meteorology.

By considering the departure of the earth-atmosphere system from sphericity is negligible for meteorological purpose, the vector form of momentum equation (2.25) can be expanded in spherical coordinates with the coordinate axes (λ, ϕ, z), where λ is longitude, ϕ is latitude, and z is the vertical distance above the surface of earth as in Fig. (2.3).

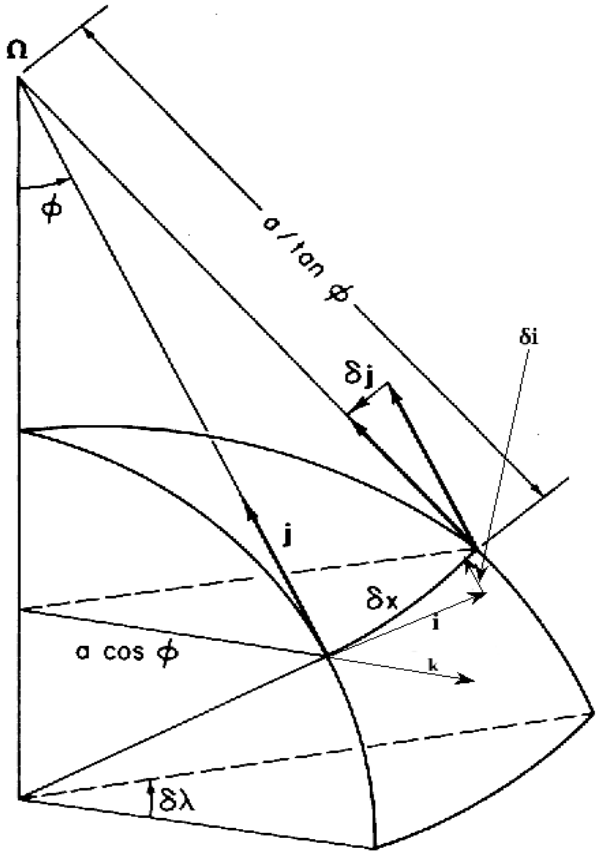

Figure 2.3: Spherical representation of Earth's coordinates system.

Depending on figure (2.3) and taking the unit vectors **i**, **j**, and **k** as directed along east, north, and vertically upward respectively, the relative velocity can be written as

$$\mathbf{U} = \mathbf{i}u + \mathbf{j}v + \mathbf{k}w \tag{2.26}$$

where u, v, and w are the eastward, northward, and upward velocities respectively, which

can be written in spherical coordinates with the help of Fig. (2.3) as

$$u \equiv r\cos\phi\frac{d\lambda}{dt},\ v \equiv r\frac{d\phi}{dt},\ w \equiv \frac{dz}{dt} \tag{2.27}$$

where r is the distance from the center of earth which is $r = a + z$, and a and z are the radius of earth and vertical height respectively.

Since $z << a$, $r = a$ is a good approximation for the regions of the atmosphere for meteorological interest. Defining x and y as eastward and northward distance, $dx = a\cos\phi d\lambda$ and $dy = ad\phi$ with the horizontal velocity components $u \equiv dx/dt$ and $v \equiv dy/dt$ in the eastward and northward directions and also the unit vectors $\mathbf{i}$, $\mathbf{j}$, and $\mathbf{k}$ are functions of position on spherical earth, $(x,\ y,\ z)$ are not Cartesian coordinates. Based on this information:

$$\frac{d\mathbf{U}}{dt} = \mathbf{i}\frac{du}{dt} + \mathbf{j}\frac{dv}{dt} + \mathbf{k}\frac{dw}{dt} + u\frac{d\mathbf{i}}{dt} + v\frac{d\mathbf{j}}{dt} + w\frac{d\mathbf{k}}{dt} \tag{2.28}$$

Depending on Fig. (2.3) and applying total differentiation technique, the time derivatives of unit vectors can be written as;

$$\frac{d\mathbf{i}}{dt} = \frac{u}{a\cos\phi}(\mathbf{j}\sin\phi - \mathbf{k}\cos\phi) \tag{2.29}$$

$$\frac{d\mathbf{j}}{dt} = \frac{-u\tan\phi}{a}\mathbf{i} - \frac{v}{a}\mathbf{k} \tag{2.30}$$

$$\frac{d\mathbf{k}}{dt} = \mathbf{i}\frac{u}{a} + \mathbf{j}\frac{v}{a} \tag{2.31}$$

Substituting equations (2.29)-(2.31) into equation (2.28) and rearranging some terms, the expansion of acceleration in spherical polar coordinate becomes

$$\begin{aligned}\frac{d\mathbf{U}}{dt} = &\left(\frac{du}{dt} - \frac{uv\tan\phi}{a} + \frac{uw}{a}\right)\mathbf{i} + \\ &\left(\frac{dv}{dt} + \frac{u^2\tan\phi}{a} + \frac{vw}{a}\right)\mathbf{j} \\ &+ \left(\frac{dw}{dt} - \frac{u^2+v^2}{a}\right)\mathbf{k}\end{aligned} \tag{2.32}$$

The component expansion of the force terms in equation (2.25) can be rewritten as:

$$-2\boldsymbol{\Omega}\times\mathbf{U} = -(2\Omega w\cos\phi - 2\Omega v\sin\phi)\mathbf{i} - 2\Omega u\sin\phi\mathbf{j} + 2\Omega u\cos\phi\mathbf{k} \tag{2.33}$$

for the Coriolis term;

$$\nabla p = \mathbf{i}\frac{\partial p}{\partial x} + \mathbf{j}\frac{\partial p}{\partial y} + \mathbf{k}\frac{\partial p}{\partial z} \tag{2.34}$$

for the pressure gradient; and

$$\mathbf{g} = -g\mathbf{k} \tag{2.35}$$

for gravity.

Finally the frictional force is

$$\mathbf{F}_r = \mathbf{i}F_{rx} + \mathbf{j}F_{ry} + \mathbf{k}F_{rz} \tag{2.36}$$

Substituting equations (2.33)-(2.36) into equation (2.25) and comparing all terms in the **i**, **j**, and **k** directions from equation (2.32), the eastward, northward, and vertical component of momentum equations can be written respectively as

$$\frac{du}{dt} - \frac{uv\tan\phi}{a} + \frac{uw}{a} = -\frac{1}{\rho}\frac{\partial p}{\partial x} + 2\Omega v\sin\phi - 2\Omega w\cos\phi + F_{rx} \tag{2.37}$$

$$\frac{dv}{dt} - \frac{u^2\tan\phi}{a} + \frac{vw}{a} = -\frac{1}{\rho}\frac{\partial p}{\partial y} - 2\Omega u\sin\phi + F_{ry} \tag{2.38}$$

$$\frac{dw}{dt} - \frac{u^2+v^2}{a} = -\frac{1}{\rho}\frac{\partial p}{\partial z} - g + 2\Omega u\cos\phi + F_{ry} \tag{2.39}$$

The terms that is proportional to $\frac{1}{a}$ in the above three consquative equations are the curvature terms that arise due to the curvature of earth. Since the curvature terms, $2\Omega w\cos\phi$, and frictional forces are unimportant and negligible as compared to the remaining terms, the horizontal momentum equations can be rewritten as

$$\frac{du}{dt} = -\frac{1}{\rho}\frac{\partial p}{\partial x} + fv \tag{2.40}$$

and

$$\frac{dv}{dt} = -\frac{1}{\rho}\frac{\partial p}{\partial y} - fu \tag{2.41}$$

where $f \equiv 2\Omega\sin\phi$ which is the Coriolis force.

Expanding the total derivatives into their local and advective parts, we get

$$\frac{d}{dt} = \frac{\partial}{\partial t} + u\frac{\partial}{\partial x} + v\frac{\partial}{\partial y} + w\frac{\partial}{\partial z} \tag{2.42}$$

The horizontal wind speeds and the vertical wind speed can be rewritten in vector form respectively as

$$\mathbf{V_h} = u\mathbf{i} + v\mathbf{j}$$

and

$$\mathbf{V_v} = w\mathbf{k} \tag{2.43}$$

Applying the total derivative in equation(2.42) to the horizontal wind speeds in equation (2.43), gives

$$\frac{d\mathbf{V_h}}{dt} = \frac{\partial \mathbf{V_h}}{\partial t} + (\mathbf{V_h} \cdot \nabla)\,\mathbf{V_h} \tag{2.44}$$

Multiplying equations (2.44) and the continuity equation (2.6) by ρ and $\mathbf{V_h}$ respectively, we obtain

$$\rho\frac{\mathbf{V_h}}{dt} = \rho\frac{\partial \mathbf{V_h}}{\partial t} + \rho\,(\mathbf{V_h} \cdot \nabla)\,\mathbf{V_h} \tag{2.45}$$

and

$$\mathbf{V_h}\frac{\partial \rho}{\partial t} = -\mathbf{V_h}\rho\,(\nabla \cdot \mathbf{V_h}) - \mathbf{V_h}\,(\mathbf{V_h} \cdot \nabla)\,\rho \tag{2.46}$$

Adding equations (2.45) and (2.46) then gives

$$\rho\frac{d\mathbf{V_h}}{dt} = \rho\left(\frac{\partial \mathbf{V_h}}{\partial t} + (\mathbf{V_h} \cdot \nabla)\mathbf{V_h}\right) + \mathbf{V_h}\left(\frac{\partial \rho}{\partial t} + \nabla \cdot (\mathbf{V_h}\rho)\right) \tag{2.47}$$

where $\rho(\nabla \cdot \mathbf{V_h}) + (\mathbf{V_h} \cdot \nabla)\rho = \nabla \cdot (\mathbf{V_h}\rho)$

The field variables $\mathbf{V_h}$ and ρ can be decomposed into their perturbation form as $\mathbf{V_h} = \overline{\mathbf{V_h}} + \mathbf{V'_h}$ and $\rho = \overline{\rho} + \rho'$. Since density perturbations are generally very small ($\rho' << \overline{\rho}$), $\rho \approx \overline{\rho}$, equation (2.47) becomes

$$\begin{aligned}\overline{\rho}\frac{d\mathbf{V_h}}{dt} = \overline{\rho}\Bigg(&\frac{\partial(\overline{\mathbf{V_h}} + \mathbf{V_h}')}{\partial t} + [(\overline{\mathbf{V_h}} + \mathbf{V_h}') \cdot \nabla](\overline{\mathbf{V_h}} + \mathbf{V_h}')\Bigg) \\ &+(\overline{\mathbf{V_h}} + \mathbf{V_h}')\left(\frac{\partial \overline{\rho}}{\partial t} + \nabla[(\overline{\mathbf{V_h}} + \mathbf{V_h}')\overline{\rho}]\right)\end{aligned} \tag{2.48}$$

Taking the time and grid volume average of this equations, eliminating zero value terms

and removing unnecessary over bars, equation (2.48) becomes

$$\overline{\rho}\frac{d\mathbf{V_h}}{dt} = \overline{\rho}\left(\underbrace{\frac{\partial(\overline{\mathbf{V_h}})}{\partial t} + (\overline{\mathbf{V_h}}\cdot\nabla)\overline{\mathbf{V_h}}}_{\frac{d\overline{\mathbf{V}}_h}{dt}}\right) + \overline{\mathbf{V_h}}\left(\frac{\partial\overline{\rho}}{\partial t} + \nabla\cdot(\overline{\mathbf{V_h}}\overline{\rho})\right) + \underbrace{\overline{\overline{\rho}(\mathbf{V_h}'\cdot\nabla)\mathbf{V_h}' + \mathbf{V_h}'\nabla\cdot(\mathbf{V_h}'\overline{\rho})}}_{\overline{\rho}\frac{d\mathbf{V_h}'}{dt}} \tag{2.49}$$

The last term is treated as a force per unit mass (turbulent-flux divergence) which can be expanded as

$$\begin{aligned}\frac{d\mathbf{V_h}'}{dt} = \mathbf{i}\frac{1}{\rho}\left(\frac{\partial}{\partial x}(\rho\overline{u'u'}) + \frac{\partial}{\partial y}(\rho\overline{v'u'}) + \frac{\partial}{\partial z}(\rho\overline{w'u'})\right)\\ +\mathbf{j}\frac{1}{\rho}\left(\frac{\partial}{\partial x}(\rho\overline{u'v'}) + \frac{\partial}{\partial y}(\rho\overline{v'v'}) + \frac{\partial}{\partial z}(\rho\overline{w'v'})\right)\\ +\mathbf{k}\frac{i}{\rho}\left(\frac{\partial}{\partial x}(\rho\overline{u'w'}) + \frac{\partial}{\partial y}(\rho\overline{v'w'}) + \frac{\partial}{\partial z}(\rho\overline{w'w'})\right)\end{aligned} \tag{2.50}$$

Averages such as $\overline{u'u'}$ and $\overline{w'u'}$ are kinematic turbulent fluxes of momentum.

Applying k-theory, one can write

$\overline{w'u'} = -k_{m,zx}\frac{\partial\overline{u'}}{\partial z}$, $\overline{w'v'} = -k_{m,zy}\frac{\partial\overline{v'}}{\partial z}$, etc.

where $k_m's$ are eddy diffusion coefficients and equation (2.50) can be rewritten as

$$\begin{aligned}\frac{d\mathbf{V_h}'}{dt} = -\mathbf{i}\frac{1}{\rho}\left(\frac{\partial}{\partial x}(\rho k_{m,xx}\frac{\partial\overline{u'}}{\partial x}) + \frac{\partial}{\partial y}(\rho k_{m,yx}\frac{\partial\overline{u'}}{\partial y}) + \frac{\partial}{\partial z}(\rho k_{m,zx}\frac{\partial\overline{u'}}{\partial z})\right)\\ -\mathbf{j}\frac{1}{\rho}\left(\frac{\partial}{\partial x}(\rho k_{m,xy}\frac{\partial\overline{v'}}{\partial x}) + \frac{\partial}{\partial y}(\rho k_{m,yy}\frac{\partial\overline{v'}}{\partial y}) + \frac{\partial}{\partial z}(\rho k_{m,zy}\frac{\partial\overline{v'}}{\partial z})\right)\\ -\mathbf{k}\frac{1}{\rho}\left(\frac{\partial}{\partial x}(\rho k_{m,xz}\frac{\partial\overline{w'}}{\partial x}) + \frac{\partial}{\partial y}(\rho k_{m,yz}\frac{\partial\overline{w'}}{\partial y}) + \frac{\partial}{\partial z}(\rho k_{m,zz}\frac{\partial\overline{w'}}{\partial z})\right)\end{aligned} \tag{2.51}$$

The eddy diffusion coefficients in the above equation (2.51) can be written in tensor form

for u ,v ,and w respectively as

$$
\begin{aligned}
k_m &= \begin{bmatrix} k_{m,xx} & 0 & 0 \\ 0 & k_{m,yx} & 0 \\ 0 & 0 & k_{m,zx} \end{bmatrix} \text{ for } u, \\
k_m &= \begin{bmatrix} k_{m,xy} & 0 & 0 \\ 0 & k_{m,yy} & 0 \\ 0 & 0 & k_{m,zy} \end{bmatrix} \text{ for } v, \\
k_m &= \begin{bmatrix} k_{m,xz} & 0 & 0 \\ 0 & k_{m,yz} & 0 \\ 0 & 0 & k_{m,zz} \end{bmatrix} \text{ for } w,
\end{aligned}
\tag{2.52}
$$

Now equation (2.51) can be rewritten in vector and tensor notation as

$$
\frac{d\mathbf{V'_h}}{dt} = -\frac{1}{\rho}(\nabla \cdot \rho \mathbf{k}_m \nabla)\mathbf{V}_h \tag{2.53}
$$

Removing over bars for simplicity and substituting the above relations into equation (2.25) and also considering that the effects of air viscosity is negligible for most atmospheric scales leads to

$$
\frac{d\mathbf{V_h}}{dt} = -f\mathbf{k} \times \mathbf{V}_h - \nabla\Phi - \frac{1}{\rho}\nabla p + \frac{1}{\rho}(\nabla \cdot \rho \mathbf{k}_m \nabla)\mathbf{V}_h \tag{2.54}
$$

where $-\nabla\Phi$ is the effective gravity and the total derivatives in equation (2.54) can be converted to sigma pressure coordinate using

$$
\frac{d}{dt} = \left(\frac{\partial}{\partial t}\right)_\sigma + \mathbf{V}_h \cdot \nabla_\sigma + \dot{\sigma}\frac{\partial}{\partial \sigma} \tag{2.55}
$$

Applying equation (2.55) to the horizontal momentum equation (2.54) yields

$$
\left(\frac{\partial \mathbf{V}_h}{\partial t}\right)_\sigma + \mathbf{V}_h \cdot \nabla_\sigma \mathbf{V}_h + \dot{\sigma}\frac{\partial \mathbf{V}_h}{\partial \sigma} + f\mathbf{k} \times \mathbf{V}_h = -\frac{1}{\rho}\nabla_z p + \frac{1}{\rho}(\nabla \cdot \rho \mathbf{k}_m \nabla)\mathbf{V}_h \tag{2.56}
$$

But the gradient in altitude coordinate ($\frac{1}{\rho}\nabla_z p = \nabla_p \Phi$) can be converted to sigma coordinate using $\nabla_p = \nabla_\sigma - \frac{\sigma}{p^*}\nabla_\sigma(p^*)\frac{\partial}{\partial\sigma}$ as

$$
\frac{1}{\rho}\nabla_z p = \nabla_p \Phi = \nabla_\sigma \Phi - \frac{\sigma}{p^*}\nabla_\sigma(p^*)\frac{\partial}{\partial\sigma}\Phi \tag{2.57}
$$

Substituting this equation into equation(2.56), the vector form of horizontal momentum equations in sigma-pressure coordinates becomes

$$\begin{aligned}\left(\frac{\partial \mathbf{V}_h}{\partial t}\right)_\sigma + \mathbf{V}_h \cdot \nabla_\sigma \mathbf{V}_h + \dot{\sigma}\frac{\partial \mathbf{V}_h}{\partial \sigma} + f\mathbf{k} \times \mathbf{V}_h = -\nabla_\sigma \Phi \\ + \frac{\sigma}{p^*}\nabla_\sigma(p^*)\frac{\partial}{\partial \sigma}\Phi + \frac{1}{\rho}(\nabla \cdot \rho \mathbf{k}_m \nabla)\mathbf{V}_h\end{aligned} \tag{2.58}$$

The hydrostatic equation in the sigma-pressure coordinate is $\frac{\partial \Phi}{\partial \sigma} = \frac{-p^* RT_v}{p_a}$. Thus,

$$\frac{\sigma}{p^*}\frac{\partial \Phi}{\partial \sigma} = -\frac{RT_v}{p^* + p_t} \tag{2.59}$$

Substituting equation (2.59) into equation (2.58)

$$\begin{aligned}\left(\frac{\partial \mathbf{V}_h}{\partial t}\right)_\sigma + \mathbf{V}_h \cdot \nabla_\sigma \mathbf{V}_h + \dot{\sigma}\frac{\partial \mathbf{V}_h}{\partial \sigma} + f\mathbf{k} \times \mathbf{V}_h = -\nabla_\sigma \Phi \\ - \frac{RT_v}{p^* + p_t/\sigma}\nabla_\sigma(p^*) + \frac{1}{\rho}(\nabla \cdot \rho \mathbf{k}_m \nabla)\mathbf{V}_h\end{aligned} \tag{2.60}$$

The vector form of momentum equation (2.60) can be decomposed into its components like

$$\begin{aligned}\frac{\partial u}{\partial t} = -\left(\frac{u\partial u}{\partial x} + \frac{v\partial u}{\partial y}\right) - \dot{\sigma}\frac{\partial u}{\partial \sigma} - \left(\frac{RT_v}{p^* + p_t/\sigma}\nabla_\sigma(p^*)\frac{\partial p^*}{\partial x} + \frac{\partial \Phi}{\partial x}\right) \\ + fv + \frac{(\nabla \cdot \rho \mathbf{k}_m \nabla)}{\rho}u\end{aligned} \tag{2.61}$$

and

$$\begin{aligned}\frac{\partial v}{\partial t} = -\left(\frac{u\partial v}{\partial x} + \frac{v\partial v}{\partial y}\right) - \dot{\sigma}\frac{\partial v}{\partial \sigma} - \left(\frac{RT_v}{p^* + p_t/\sigma}\nabla_\sigma(p^*)\frac{\partial p^*}{\partial x} + \frac{\partial \Phi}{\partial y}\right) \\ + fu + \frac{(\nabla \cdot \rho \mathbf{k}_m \nabla)}{\rho}v\end{aligned} \tag{2.62}$$

Multiplying equations (2.61) and (2.62) by p^* on both sides, the flux form of the momentum equations becomes

$$\begin{aligned}\frac{\partial up^*}{\partial t} = -\left(\frac{u\partial up^*}{\partial x} + \frac{v\partial up^*}{\partial y}\right) - \dot{\sigma}\frac{\partial up^*}{\partial \sigma} - p^*\left(\frac{RT_v}{p^* + p_t/\sigma}\nabla_\sigma(p^*)\frac{\partial p^*}{\partial x} + \frac{\partial \Phi}{\partial x}\right) \\ + p^* fv + F_H u + F_V u\end{aligned} \tag{2.63}$$

and

$$\frac{\partial vp^*}{\partial t} = -\left(\frac{u\partial vp^*}{\partial x} + \frac{v\partial vp^*}{\partial y}\right) - \dot{\sigma}\frac{\partial vp^*}{\partial \sigma} - p^*\left(\frac{RT_v}{p^* + p_t/\sigma}\nabla_\sigma(p^*)\frac{\partial p^*}{\partial x} + \frac{\partial \Phi}{\partial y}\right) + p^* f u + F_H v + F_V v \tag{2.64}$$

where $F_H u + F_V u = p^* \frac{(\nabla \cdot \rho k_m \nabla)}{\rho} u$ and $F_H v + F_V v = p^* \frac{(\nabla \cdot \rho k_m \nabla)}{\rho} v$ are the horizontal and vertical diffusion terms respectively.

2.4 Conservation of Energy

Air temperature is affected by energy transfer and work. Energy transfer processes include conduction, mechanical turbulence, thermal turbulence, advection, and radiation. Energy is released to the air during condensation of water vapor, deposition of water vapor, freezing of liquid water, exothermic chemical reactions, and radioactive decay. Energy is removed from the air upon melting of ice, sublimation of ice, and evaporation of liquid water. Energy exchange may also occur upon the change of state of substances other than water. Because the quantities of non-water substances changing state are relatively small, resulting energy exchanges are small. Energy, like air density and species concentrations, is conserved in a system.

An equation describing energy changes in the atmosphere can be derived by combining the first law of thermodynamics with the continuity equation for air. The first law of thermodynamics is usually derived by considering a system in thermodynamic equilibrium, that is, a system that is initially at rest and after exchanging heat with its surroundings and doing work on the surroundings is again at rest. For such a system the first law states that the change in internal energy of the system is equal to the difference/sum between the heat added to the system and the work done by/on the system. The first law in terms of energy per unit mass of air (J kg^{-1}) as

$$dU = dQ \mp dW \tag{2.65}$$

The rate of change of this total thermodynamic energy is equal to the rate of diabatic heating minus/plus the rate at which work is done on the fluid parcel by external forces.

The external forces that act on a fluid element may be divided into surface forces, such as pressure and viscosity, and body forces, such as gravity or the Coriolis force.

The work done per unit mass of air (dW) is given by a relation as

$$dW = \frac{pdV}{M} = pd\alpha \tag{2.66}$$

where p is pressure of air, dV is the change in volume of the air, and $\alpha = \frac{V}{M}$ is the specific volume of air.

The change in internal energy of the air is its change in temperature multiplied by the energy required to change its temperature one degree Celsius (1 K) without affecting the volume or work done by or on the air which is given by

$$DU = \left(\frac{\partial Q}{\partial T}\right)_v = c_{v,m}dT \tag{2.67}$$

where $c_{v,m} = \left(\frac{\partial Q}{\partial T}\right)_v$ is the specific heat of moist air at constant volume.

Substituting (2.67) and (2.66) into (2.65) which gives the first law of thermodynamics for the atmosphere as

$$dQ = c_{v,m}dT + pd\alpha \tag{2.68}$$

From equation of state, $p = \rho R_m T$, with $\alpha = \frac{1}{\rho}$ which gives $p\alpha = R_m T$ and can be differentiated to get

$$pd\alpha + \alpha dp = R_m dT \tag{2.69}$$

where R_m is gas constant for moist air.

Rearranging and substituting equation(2.69) into equation(2.68) for $pd\alpha$ which yields another form of first law as

$$dQ = c_{p,m}dT - \frac{1}{\rho}dp \tag{2.70}$$

where $\alpha = \frac{1}{\rho}$ and $c_{p,m} = c_{v,m} + R_m$ is the specific heat capacity for moist air at constant pressure.

Differentiating equation (2.70) with respect to time and rearranging gives

$$\frac{dT}{dt} = \frac{1}{c_{p,m}}\frac{dQ}{dt} + \frac{1}{c_{p,m}\rho}dp \tag{2.71}$$

Using the total derivative $\frac{d}{dt} = \frac{\partial}{\partial t} + (\mathbf{V} \cdot \nabla)$, equation (2.71) can be rewritten as

$$\frac{\partial T}{\partial t} + (\mathbf{V} \cdot \nabla)T = \frac{1}{c_{p,m}}\frac{dQ}{dt} + \frac{1}{c_{p,m}\rho}\frac{dp}{dt} \tag{2.72}$$

The field variables ($T, \mathbf{V}$, and ρ) can be decomposed into their perturbation form as ($T = \overline{T} + T'$, $\mathbf{V} = \overline{\mathbf{V}} + \mathbf{V}'$, and $\rho = \overline{\rho} + \rho'$). Since density perturbations are very small ($\rho' << \overline{\rho}$, $\rho = \overline{\rho}$). Substituting this relations, equation (2.72) is rewritten as

$$\frac{\partial(\overline{T} + T')}{\partial t} + ((\overline{\mathbf{V}} + \mathbf{V}') \cdot \nabla)(\overline{T} + T') = \frac{1}{c_{p,m}} \frac{dQ}{dt} + \frac{1}{c_{p,m}\overline{\rho}} \frac{dp}{dt} \tag{2.73}$$

taking the time and grid-volume averaging one can obtain

$$\frac{\partial\overline{(\overline{T} + T')}}{\partial t} + \overline{((\overline{\mathbf{V}} + \mathbf{V}') \cdot \nabla)(\overline{T} + T')} = \frac{1}{c_{p,m}} \frac{\overline{dQ}}{dt} + \frac{1}{c_{p,m}\overline{\rho}} \frac{\overline{dp}}{dt} \tag{2.74}$$

which can be rearranged to

$$\frac{\partial\overline{(\overline{T} + T')}}{\partial t} + (\overline{\nabla \cdot [\overline{\mathbf{V}}\overline{\mathbf{T}} + \overline{\mathbf{V}}\mathbf{T}' + \mathbf{V}'\overline{\mathbf{T}} + \mathbf{V}'T'} = \frac{1}{c_{p,m}} \frac{\overline{dQ}}{dt} + \frac{1}{c_{p,m}\overline{\rho}} \frac{\overline{dp}}{dt} \tag{2.75}$$

Removing zero-value time and spatial derivatives and unnecessary over bars gives

$$\frac{\partial\overline{T}}{\partial t} + \nabla \cdot (\overline{\mathbf{V}T} + \overline{\nabla \cdot (\mathbf{V}'T')}) = \frac{1}{c_{p,m}} \frac{\overline{dQ}}{dt} + \frac{1}{c_{p,m}\overline{\rho}} \frac{\overline{dp}}{dt} \tag{2.76}$$

which can also be rearranged to

$$\frac{\partial\overline{T}}{\partial t} + (\overline{\mathbf{V}} \cdot \nabla)\overline{T} + \nabla \cdot (\overline{\mathbf{V}'T'}) = \frac{1}{c_{p,m}} \frac{\overline{dQ}}{dt} + \frac{1}{c_{p,m}\overline{\rho}} \frac{\overline{dp}}{dt} \tag{2.77}$$

The kinematic turbulent sensible heat flux ($\overline{\mathbf{V}'T'}$) can be parametrized as $\overline{u'T'} = -k_{h,xx}\frac{\partial\overline{T}}{\partial x}$, $\overline{v'T'} = -k_{h,yy}\frac{\partial\overline{T}}{\partial y}$, and $\overline{w'T'} = -k_{h,zz}\frac{\partial\overline{T}}{\partial z}$. Where the k_h's are the eddy diffusion coefficients which can be written in vector form as

$$\overline{\mathbf{V}'T'} = -\mathbf{K}_h \nabla\overline{T} \tag{2.78}$$

Now substituting equation(2.78) into (2.77) and rearranging, we get

$$\frac{\partial\overline{T}}{\partial t} + (\overline{\mathbf{V}} \cdot \nabla)\overline{T} = \frac{1}{\overline{\rho}}(\nabla \cdot \overline{\rho}\mathbf{K}_h \nabla)\overline{T} + \frac{1}{c_{p,m}} \frac{\overline{dQ}}{dt} + \frac{1}{c_{p,m}\overline{\rho}} \frac{\overline{dp}}{dt} \tag{2.79}$$

Applying the total derivative in Cartesian sigma coordinates ($\frac{d}{dt} = \left(\frac{\partial}{\partial t}\right)_\sigma + \mathbf{V}_h \cdot \nabla + \dot{\sigma}\frac{\partial}{\partial\sigma}$) where $\mathbf{V}_h$ is the horizontal component of wind speed ($\mathbf{V}$) gives

$$\left(\frac{\partial\overline{T}}{\partial t}\right)_\sigma + (\overline{\mathbf{V}} \cdot \nabla_\sigma)\overline{T} + \dot{\sigma}\frac{\partial\overline{T}}{\partial\sigma} = \frac{1}{\overline{\rho}}(\nabla \cdot \overline{\rho}\mathbf{K}_h \nabla)\overline{T} + \frac{1}{c_{p,m}} \frac{\overline{dQ}}{dt} + \frac{1}{c_{p,m}\overline{\rho}} \frac{\overline{dp}}{dt} \tag{2.80}$$

Multiplying equation (2.80) by p^*, the continuity equation (2.14) by $\overline{T}$, adding the two equations and rearranging leads to

$$\left(\frac{\partial \overline{T} p^*}{\partial t}\right)_\sigma + \nabla_\sigma \cdot (\mathbf{V}_h p^* \overline{T}) + p^* \frac{\dot{\sigma} \partial \overline{T}}{\partial \sigma} = \frac{p^*}{\overline{\rho}} (\nabla \cdot \overline{\rho} \mathbf{K}_h \nabla) \overline{T} + \frac{p^*}{c_{p,m}} \overline{\frac{dQ}{dt}} + \frac{p^*}{c_{p,m} \overline{\rho}} \overline{\frac{dp}{dt}} \tag{2.81}$$

Removing over bars for simplicity, using $p = \sigma p^*$, $\frac{dp_t}{dt} > 0$ and rearranging again yields

$$\begin{aligned}\left(\frac{\partial T p^*}{\partial t}\right)_\sigma + \underbrace{\nabla_\sigma \cdot (\mathbf{V}_h p^* T)}_{\frac{\partial u p^* T}{\partial x} + \frac{\partial v p^* T}{\partial y}} + p^* \frac{\dot{\sigma} \partial T}{\partial \sigma} = \underbrace{\frac{p^*}{\rho} (\nabla \cdot \rho \mathbf{K}_h \nabla) T}_{F_H T + F_V T} \\ + \frac{p^*}{c_{p,m}} \frac{dQ}{dt} + \frac{R T_v \omega}{c_{p,m} (\sigma + p_t / p^*)}\end{aligned} \tag{2.82}$$

The complete thermodynamic Equation in cartecian-sigma coordinates is, therefore written as

$$\begin{aligned}\left(\frac{\partial T p^*}{\partial t}\right)_\sigma = -\left(\frac{\partial u p^* T}{\partial x} + \frac{\partial v p^* T}{\partial y}\right) - p^* \frac{\dot{\sigma} \partial T}{\partial \sigma} + \frac{R T_v \omega}{c_{p,m} (\sigma + p_t / p^*)} \\ + \frac{p^*}{c_{p,m}} \frac{dQ}{dt} + F_H T + F_V T\end{aligned} \tag{2.83}$$

where $F_H T$ represents the effect of horizontal diffusion, $F_V T$ represents the effect of vertical mixing and dry convective adjustment and the rest as defined before.

Chapter 3

Regional Climate Model Version 4 (RegCM4)

The idea that Limited Area Models (LAMs) could be used for regional studies was originally proposed by Dickinson *et al.* (1989) and Giorgi (1990). This idea was based on the concept of one-way nesting, in which large scale meteorological fields from General Circulation Model (GCM) runs provide initial and time- dependent meteorological lateral boundary conditions (LBCs) for high resolution Regional Climate Model (RCM) simulations, with no feedback from the RCM to the driving GCM.

The first generation National Center for Atmospheric Research (NCAR) RegCM was built upon the NCAR-Pennsylvania State University (PSU) Mesoscale Model version 4 (MM4) in the late 1980s (Dickinson *et al.*, 1989; Giorgi, 1989). The dynamical component of the model originated from the MM4, which is a compressible, finite difference model with hydrostatic balance and vertical -coordinates. Later, the use of a split-explicit time integration scheme was added along with an algorithm for reducing horizontal diffusion in the presence of steep topographical gradients (Giorgi *et al.*, 1993a and Giorgi *et al.*, 1993b). As a result, the dynamical core of the RegCM is similar to that of the hydrostatic version of Mesoscale Model version 5 (MM5) (Grell *et al.*, 1994).

For application of the MM4 to climate studies, a number of physics parameterizations were replaced, mostly in the areas of radiative transfer and land surface physics, which led to the first generation RegCM (Dickinson *et al.*, 1989; Giorgi, 1990). The first generation RegCM included the Biosphere-Atmosphere Transfer Scheme (BATS) (Dickinson

et al., 1986) for surface process representation, the radiative transfer scheme of the Community Climate Model version 1 (CCM1), a medium resolution local planetary boundary layer scheme, the Kuo-type cumulus convection scheme of Anthes (1977) and the explicit moisture scheme of Hsie *et al.* (1984).

A first major upgrade of the model physics and numerical schemes was documented by Giorgi *et al.* (1993a) and Giorgi *et al.* (1993b), and resulted in a second generation Regional Climate Model version 2 (RegCM2). The physics of RegCM2 was based on that of the NCAR Community Climate Model version 2 (CCM2) (Hack *et al.*, 1993), and the mesoscale model MM5 (Grell *et al.*, 1994). In particular, the CCM2 radiative transfer package (Briegleb1992) was used for radiation calculations, the non local boundary layer scheme of Holtslag *et al.* (1990) replaced the older local scheme, the mass flux cumulus cloud scheme of Grell (1993) was added as an option, and the latest version of BATS1E (Dickinson *et al.*, 1993) was included in the model.

In the last few years, some new physics schemes have become available for use in the RegCM, mostly based on physics schemes of the latest version of the Community Climate Model (CCM), Community Climate Model version 3 (CCM3) (Kiehl *et al.*, 1996). First, the CCM2 radiative transfer package has been replaced by that of the CCM3. In the CCM2 package, the effects of H_2O, O_3, O_2, CO_2 and clouds were accounted for by the model. Solar radiative transfer was treated with δ-Eddington approach and cloud radiation depended on three cloud parameters, the cloud fractional cover, the cloud liquid water content, and the cloud effective droplet radius. The CCM3 scheme retains the same structure as that of the CCM2, but it includes new features such as the effect of additional greenhouse gases (NO_2, CH_4, CFCs), atmospheric aerosols, and cloud ice.

The other primary changes are in the areas of cloud and precipitation processes. The original explicit moisture scheme of Hsie *et al.* (1984) has been substituted with a simplified version because the original scheme was computationally too expensive to be run in climate mode. In the simplified scheme only a prognostic equation for cloud water is included, which accounts for cloud water formation, advection and mixing by turbulence, re-evaporation in sub-saturated conditions, and conversion into rain via a bulk auto-conversion term. The main novelty of this scheme does not reside of course in the simplistic micro-physics, but in the fact that the prognosed cloud water variable is directly used in the cloud radiation calculations. In the previous versions of the model, cloud water variables for radiation calculations were diagnosed in terms of the local relative humidity.

This new feature adds a very important and far reaching element of interaction between the simulated hydrologic cycle and energy budget calculations.

Changes in the model physics include a large-scale cloud and precipitation scheme which accounts for the sub-grid scale variability of clouds (Pal *et al.*, 2000), new parameterizations for ocean surface fluxes (Zeng *et al.*, 1998), and a cumulus convection scheme (Emanuel, 1991; Emanuel & Zivkovic-Rothman, 1999). Also new in the model is a mosaic-type parameterization of sub grid scale heterogeneity in topography and land use (Giorgi *et al.*, 2003b). Other improvements in RegCM3 involve the input data. The United States Geological Survey (USGS) global land cover characterization and global 30 Arc-second elevation datasets are now used to create the terrain files. In addition, National Centers for Environmental Prediction (NCEP) and European Centre for Medium-Range Weather Forecasts (ECMWF) global reanalysis datasets are used for the initial and boundary conditions. Lastly, improvements in the user-friendliness of the model have been made.

The RegCM modeling system has four components: Terrain, ICBC, RegCM, and Post-processor. Terrain and ICBC are the two components of RegCM preprocessor. Terrestrial variables (including elevation, land-use and sea surface temperature) and three-dimensional isobaric meteorological data are horizontally interpolated from a latitude-longitude mesh to a high-resolution domain on either a Rotated (and Normal) Mercator, Lambert Conformal, or Polar Stereographic projection. Vertical interpolation from pressure levels to the σ coordinate system of RegCM is also performed. σ surfaces near the ground closely follow the terrain, and the higher-level σ surfaces tend to approximate isobaric surfaces.

Since the vertical and horizontal resolution and domain size can vary, the modeling package programs employ parameterized dimensions requiring a variable amount of core memory, and the requisite hard-disk storage amount is varied accordingly.

3.1 The RegCM Model Grid

3.1.1 The Vertical Grid

The modeling system usually gets and analyzes its data on pressure surfaces, but these have to be interpolated to the model's vertical coordinate before input to the model. The vertical coordinate is terrain-following (Fig. 3.1) meaning that the lower grid levels follow

the terrain while the upper surface is flatter. Intermediate levels progressively flatten as the pressure decreases toward the top of the model. A dimensionless σ coordinate is used to define the model levels where p is the pressure, p_t is a specified constant top pressure, p_s is the surface pressure. Thus,

$$\sigma = \frac{(p - p_t)}{(p_s - p_t)} \tag{3.1}$$

It can be seen from equation (3.1) and Fig. (3.1) that σ is zero at the top and one at the surface, and each model level is defined by a value of σ. The model vertical resolution is defined by a list of values between zero and one that do not necessarily have to be evenly spaced. Commonly the resolution in the boundary layer is much finer than above, and the number of levels may vary upon the user demand.

3.1.2 The Horizontal Grid

The horizontal grid has an Arakawa-Lamb B-staggering of the velocity variables with respect to the scalar variables. This is shown in Fig. 3.2 where it can be seen that the scalars (T, q, p, etc) are defined at the center of the grid box, while the eastward (u) and northward (v) velocity components are collocated at the corners. The center-points of grid squares will be referred to as cross points, and the corner points are dot points. Hence horizontal velocity is defined at dot points. Data is input to the model, the preprocessors do the necessary interpolation to assure consistency with the grid.

All the above variables are defined in the middle of each model vertical layer, referred to as half-levels and represented by the dashed lines in Fig. (3.1). Vertical velocity is carried at the full levels (solid lines). In defining the sigma levels it is the full levels that are listed, including levels at $\sigma = 0$ and 1. The number of model layers is therefore always one less than the number of full sigma levels.

The finite differencing in the model is, of course, crucially dependent upon the grid staggering wherever gradients or averaging are represented terms in the equation.

3.2 Conservation Laws as in RegCM4

The model dynamic equations and numerical discretization are described by Grell *et al.* (1994) as a function of map scale factors. The relationship between the dynamical equations and the map scale factors will be presented in detail in this section.

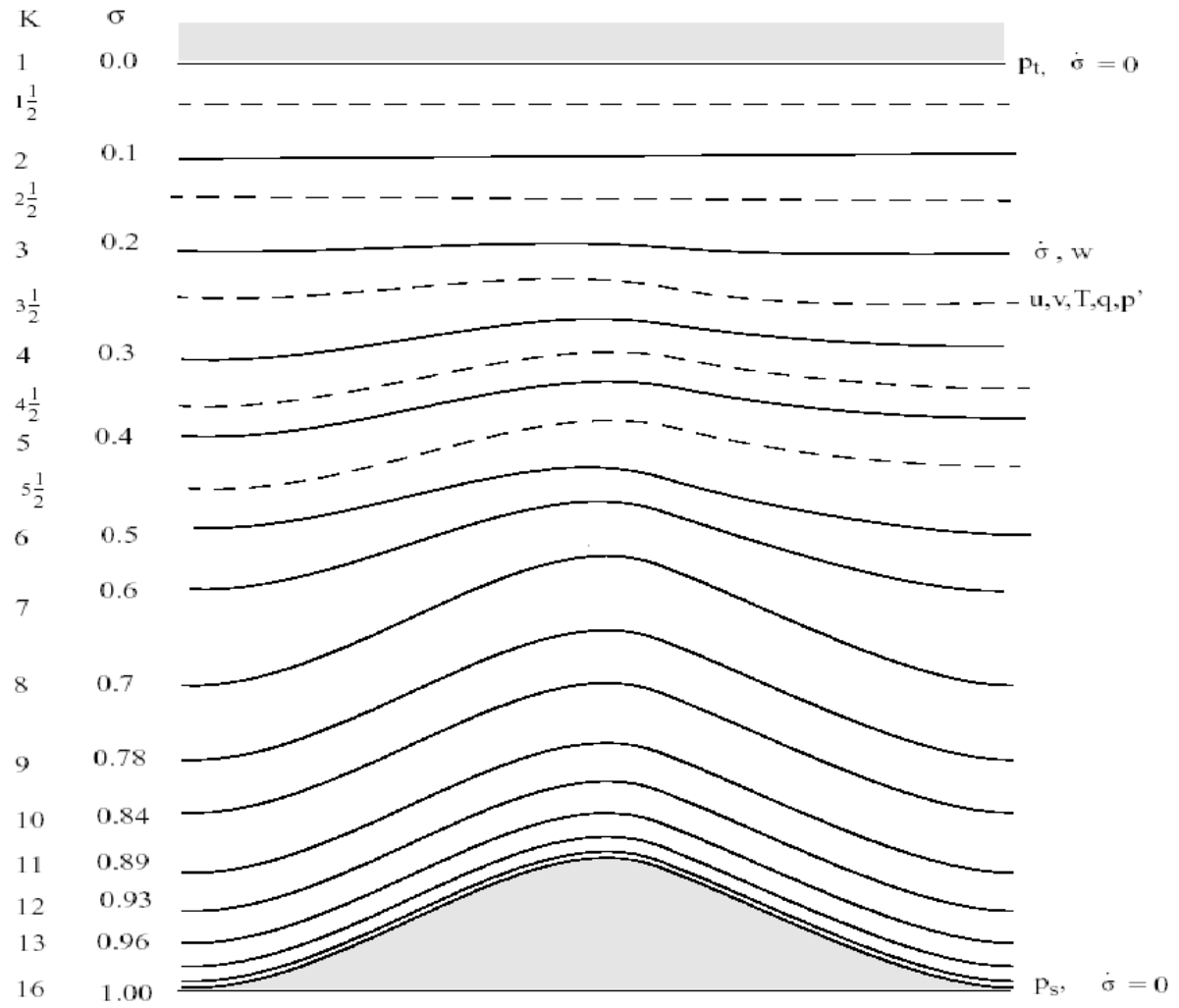

Figure 3.1: Schematic representation of the vertical structure of the model. This example is for 16 vertical layers. Dashed lines denote half-sigma levels, solid lines denote full-sigma levels (From RegCM4 User's Guide)

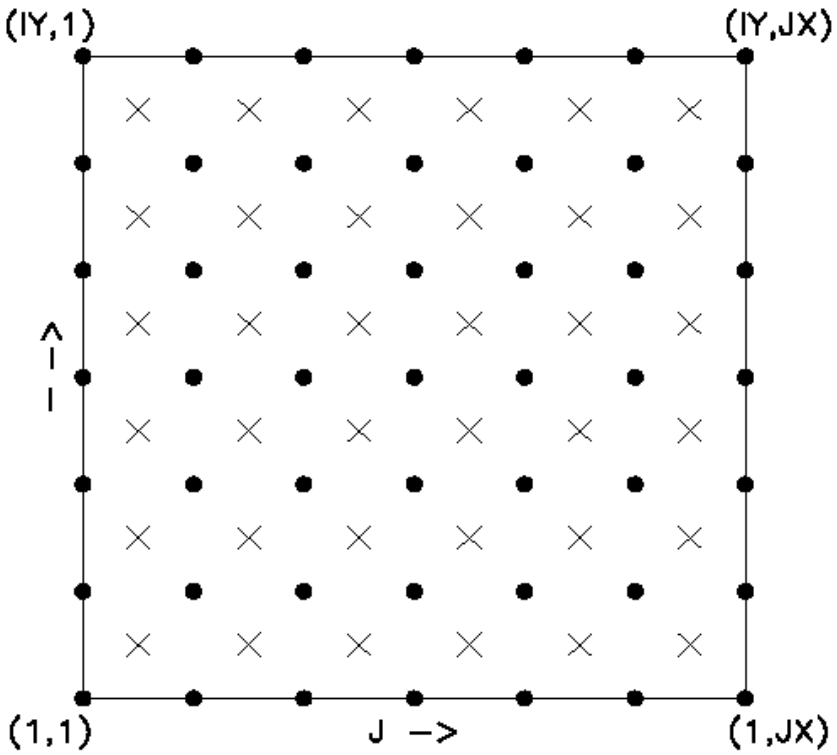

Figure 3.2: Schematic representation showing the horizontal Arakawa B-grid staggering of the dot and cross grid points (From RegCM4 User's Guide)

3.2.1 Dynamical Conservation Equations, including Map Scale Factors

The dynamical equations for the regional climate modeling can be presented with the use of two directional map scale factors (Richardson *et al.*, 2007) as follows.

Let

- X, Y, and Z are curvilinear earth coordinates which are directed (positive) along the eastward, northward, and upward respectively;
- x, y, and z are map coordinates (projected systems);
- U, V, and W are the velocity components relative to earth along the X, Y, and Z directions respectively, and
- u, v, and w are the velocity components relative to earth along the x, y, and z directions respectively.

For a non-orthogonal generalized map projections in which there is no rotation of axes, the curvilinear earth coordinates and the map coordinates are related as

$$x \equiv m_x X, \qquad y \equiv m_Y Y, \qquad and \qquad z = Z \tag{3.2}$$

Since motion along the z-direction is orthogonal, $m = 1$

From equation(3.2) one can relate that

$$dx \equiv m_x dX \qquad dy \equiv m_y dY \qquad and \qquad dz \equiv dZ$$

$$or$$

$$\frac{\partial}{\partial X} \equiv m_x \frac{\partial}{\partial x}, \qquad \frac{\partial}{\partial Y} \equiv m_y \frac{\partial}{\partial y}, \qquad and \qquad \frac{\partial}{\partial Z} \equiv \frac{\partial}{\partial z} \tag{3.3}$$

Since there is no rotation of axes, $u = U$ and $v = V$. Depending on equation (3.3) and expanding the ∇ operator relative to curvilinear earth coordinates as

$$\begin{aligned} \nabla &= \mathbf{i}\frac{\partial}{\partial X} + \mathbf{j}\frac{\partial}{\partial Y} + \mathbf{k}\frac{\partial}{\partial Z} \\ &= \mathbf{i}m_x\frac{\partial}{\partial x} + \mathbf{j}m_x\frac{\partial}{\partial y} + \mathbf{k}\frac{\partial}{\partial z} \end{aligned} \tag{3.4}$$

The divergence of any three dimensional vector $\mathbf{V} = u\mathbf{i} + u\mathbf{j} + u\mathbf{k}$ is therefore given by

$$\nabla \cdot \mathbf{V} = m_x \frac{\partial u}{\partial x} + m_y \frac{\partial v}{\partial y} + \frac{\partial w}{\partial z} = m_x m_y \left(\frac{\partial u/m_y}{\partial x} + \frac{\partial v/m_x}{\partial y} \right) + \frac{\partial w}{\partial z} \tag{3.5}$$

Since the spatial variation of map scale factors($m's$) is very small, $m's$ can be treated as constant i.e. $m_x \approx m_y$. Using this assumption equation (3.5) can be rewritten as

$$\nabla \cdot \mathbf{V} = m^2 \left(\frac{\partial u/m}{\partial x} + \frac{\partial v/m}{\partial y} \right) + \frac{\partial w}{\partial z} \tag{3.6}$$

Applying this for the horizontal wind speeds $\mathbf{V}_h = u\mathbf{i} + v\mathbf{j}$

$$\nabla \cdot \mathbf{V}_h = m^2 \left(\frac{\partial u/m}{\partial x} + \frac{\partial v/m}{\partial y} \right) \tag{3.7}$$

3.2.2 Momentum Equations

Substituting equations (3.7) and (3.4) into the dynamic equations (2.60) for the divergence and the gradient terms respectively, the horizontal momentum equations due to the eastward and northward motions rewritten as

$$\begin{aligned} \frac{\partial p^* u}{\partial t} = & -m^2 \left(\frac{\partial p^* uu/m}{\partial x} + \frac{\partial p^* vu/m}{\partial y} \right) - \frac{p^* u\dot{\sigma}}{\partial \sigma} - mp^* \left[\frac{RT_v}{(p^* + p_t/\sigma)} \frac{\partial p^*}{\partial x} + \frac{\partial \phi}{\partial x} \right] \\ & + fp^* v + F_H u + F_V u, \end{aligned} \tag{3.8}$$

and

$$\begin{aligned} \frac{\partial p^* v}{\partial t} = & -m^2 \left(\frac{\partial p^* uv/m}{\partial x} + \frac{\partial p^* vv/m}{\partial y} \right) - \frac{p^* v\dot{\sigma}}{\partial \sigma} - mp^* \left[\frac{RT_v}{(p^* + p_t/\sigma)} \frac{\partial p^*}{\partial y} + \frac{\partial \phi}{\partial y} \right] \\ & + fp^* u + F_H v + F_V v, \end{aligned} \tag{3.9}$$

where u and v are the eastward and northward components of velocity, T_v is virtual temperature, ϕ is geopotential height, f is the Coriolis parameter, R is the gas constant for dry air, $m = \frac{distance\ on\ grid}{actual\ distance\ on\ earth}$ is the map scale factor for either the Polar Stereographic, Lambert Conformal, or Mercator map projections, $\dot{\sigma} = \frac{d\sigma}{dt}$, and F_H and F_V represent the effects of horizontal and vertical diffusion, and $p^* = p_s - p_t$.

3.2.3 Continuity and Sigma dot ($\dot{\sigma}$) Equations

Substituting equation (3.7) into the continuity equation (2.14) for the divergence term,

$$\frac{\partial p^*}{\partial t} = -m^2 \left(\frac{\partial p^* u/m}{\partial x} + \frac{\partial p^* v/m}{\partial y} \right) - \frac{\partial p^* \dot{\sigma}}{\partial \sigma} \tag{3.10}$$

The vertical integral of this Equation is used to compute the temporal variation of the surface pressure in the model, which is given by:

$$\frac{\partial p^*}{\partial t} = -m^2 \int_0^1 \left(\frac{\partial p^* u/m}{\partial x} + \frac{\partial p^* v/m}{\partial y} \right) d\sigma \tag{3.11}$$

After calculation of the surface-pressure tendency $\frac{\partial p^*}{\partial t}$, the vertical velocity in sigma coordinates $\dot{\sigma}$ is computed at each level in the model from the vertical integral of equation (3.11)

$$\dot{\sigma} = -\frac{1}{p^*} \int_0^\sigma \left[\frac{\partial p^*}{\partial t} + m^2 \left(\frac{\partial p^* u/m}{\partial x} + \frac{\partial p^* v/m}{\partial y} \right) \right] d\sigma', \tag{3.12}$$

where σ' is a dummy variable of integration and $\dot{\sigma}(\sigma = 0) = 0$.

3.2.4 Thermodynamic Equation and Equation for Omega (ω)

Substituting equations (3.7) into the thermodynamic energy equations (2.82) for the divergence term, the thermodynamic energy equation becomes

$$\begin{aligned} \frac{\partial p^* T}{\partial t} = -m^2 \left(\frac{\partial p^* u T/m}{\partial x} + \frac{\partial p^* v T/m}{\partial y} \right) - \frac{\partial^* T \dot{\sigma}}{\partial \sigma} + \frac{R T_v \omega}{c_{pm}(\sigma + \frac{p_t}{p_{ast}})} \\ + \frac{p^* Q}{c_{pm}} + F_H T + F_V T \end{aligned} \tag{3.13}$$

where c_{pm} is the specific heat for moist air at constant pressure, Q is the diabatic heating, $F_H T$ represents the effect of horizontal diffusion, $F_V T$ represents the effect of vertical mixing and dry convective adjustment, and ω is

$$\omega = p^* \dot{\sigma} + \sigma \frac{dp^*}{dt} \tag{3.14}$$

where

$$\frac{dp^*}{dt} = \frac{\partial p^*}{\partial t} + m \left(u \frac{\partial p^*}{\partial x} + v \frac{\partial p^*}{\partial y} \right) \tag{3.15}$$

$c_{pm} = c_p(1 + 0.8 q_v)$ c_p is the specific heat at constant pressure for dry air and q_v is the mixing ratio of water vapor.

3.2.5 Hydrostatic Equation

The hydrostatic equation is used to compute the geopotential heights from the virtual temperature T_v ,

$$\frac{\partial \phi}{\partial \ln(\sigma + \frac{p_t}{p^*})} = -RT_v \left[1 + \frac{q_c + q_r}{1 + q_v}\right]^{-1}, \tag{3.16}$$

where $T_v = T(1 + 0.608q_v), q_v, q_c$, and q_r are the water vapor, cloud water or ice, and rain water or snow, mixing ratios.

Chapter 4

Model Description

4.1 Regional model description

The latest version of the ICTP's Regional Climate Model version 4 (RegCM4) is used in this study. RegCM4 is a primitive equation, sigma vertical coordinate, RCM based on the hydrostatic version of the dynamical core of NCAR/PSUs mesoscale meteorological model MM5 (Grell *et al.*, 1994). Radiation is represented by the CCM3 parameterization of Kiehl *et al.* (1996) and the planetary boundary layer (PBL) scheme is represented by the parameterization of Holtslag *et al.* (1990). Interactions between the land surface and the atmosphere are described using the Biosphere Atmosphere Transfer Scheme (BATS) of Dickinson *et al.* (1993) which states the role of vegetation and interactive soil moisture in modifying the surface-atmosphere exchanges of momentum, energy, and water vapor. The Zeng *et al.* (1998) scheme is used to represent fluxes from water surfaces that describes all stability conditions and includes a gustiness velocity to account for the additional flux induced by boundary layer scale variability.

Resolvable precipitation processes are treated with the sub-grid explicit moisture scheme (SUBEX) of Pal *et al.* (2000). SUBEX is a physically based parameterization that includes variation at the sub-grid scale of clouds, cloud water accretion, and evaporation of raindrops. SUBEX was developed to treat non-convective cloud and precipitation processes in RegCM replacing the older simple explicit moisture (SIMEX) scheme. SUBEX calculates the auto-conversion of cloud water to rainwater, accretion, evaporation, and cloud fraction at each grid point. The cloud fraction (CF) equation adopted by Pal *et al.*

(2000) may be stated as follows:

$$CF = 1 - \sqrt{1 - \frac{RH - RHmin}{RH_{max} - RH_{min}}} \tag{4.1}$$

where RH is the grid point relative humidity, RH_{min} is the relative humidity threshold where cloud starts to form, and RH_{max} is the relative humidity where CF reaches one. The cloud fraction equation allows SUBEX to treat part of each grid box as cloud free.

Convective precipitation is parameterized based on the Grell *et al.* (1994) scheme applying the Fritsch & Chapell (1980) closure assumption(FC). The Grell scheme is an entraining plume model considering clouds as two steady-state circulations, an updraft and a downdraft. Mixing occurs between the cloudy air and the environment at the bottom and at the top of the cloud while the mass flux is constant with height in the updraft (m_b) and downdraft (m_0). The originating levels of the updraft and downdraft are given by the levels of maximum and minimum ambient moist static energy, respectively. Activation of the scheme occurs when a parcel attains moist convection. Condensation within the updraft occurs as a saturated air parcel is lifted. The originating mass flux of the downdraft is a function of the updraft mass flux. The parameter β relates the updraft to the downdraft, dependent on wind shear, and represents the re-evaporation of convective condensate in the downdraft, where $1 - \beta$ is the precipitation efficiency. Precipitation is given by

$$P = I_1 * m_b(1 - \beta) \tag{4.2}$$

where I_1 is the normalized updraft condensate (Davis *et al.*, 2009).

FC assumes that clouds remove the available buoyant energy for convection in a given timescale, which is given by

$$m_b = \frac{ABE}{NA\tau} \tag{4.3}$$

where ABE is the available buoyant energy for convection, NA is the rate of change of ABE per unit m_b and τ is the ABE removal time scale. In general Grell-FC relates convection to the degree of instablity.

4.2 Data sets for initial and boundary conditions

The initial and boundary forcing for the RegCM4 simulation are obtained from the third generation of the European Center for Medium-Range Weather Forecasts (ECMWF) Re-

analysis datasets product ERA-interim (ERAIN) which is $1.5^o \times 1.5^o$ gridded reanalysis data (Sylla *et al.*, 2009).

The oceanic surface forcing was set using the observed sea surface temperature (SST) from the optimum interpolation SST (OISST) weekly dataset (OI_WK) (Reynolds & Smith, 1994).

4.3 Validation data

The university of East Anglia Climate Research Unit (CRU) precipitation data and Global Precipitation Climatology Project (GPCP) monthly precipitation are used to evaluate RegCM4 simulations. The CRU dataset, which is built on a 0.5^o latitude-longitude grid and available monthly for 1901-2009, is based on measurements in stations located over all land areas including oceanic islands, interpolated to a regular grid (Tchotchou & Kamga, 2009). The GPCP monthly precipitation analysis (Adler *et al.*, 2003; Huffman *et al.*, 2009) is a globally complete, monthly estimate of surface precipitation at $2.5^o \times 2.5^o$ latitude-longitude resolution that spans the period 1979 to the present. It is a merged, monthly analysis that employs precipitation estimates from low-orbit satellite SSM/I and SSMIS microwave data to perform a calibration, that varies by month and location, of geosynchronous-orbit satellite infrared (IR) data in the latitude band 40^oN-S. At higher latitudes the SSM/I and SSMIS microwave estimates are combined with estimates based on the TIROS Operational Vertical Sounder or the Atmospheric Infrared Sounder (calibrated by gauges over land and microwave estimates over ocean at lower latitudes) to provide globally complete satellite-only precipitation estimates. These multi-satellite estimates are combined with rain-gauge analyses (over land) in a two-step process that adjusts the satellite estimates to the large-scale bias of the gauges and then combines the adjusted satellite and gauge fields with weighting by inverse error variance. The monthly product is typically produced about two months after the end of the observation month.

4.4 Lateral boundary conditions

Any model calculates output parameters from a set of initial conditions, boundary conditions, input data, and model equations. This section discusses different lateral boundary schemes.

The numerical treatment of the lateral boundaries is a complex but very important aspect of the regional climate model. For this reason, there are five types of lateral boundary schemes (LBSs) that can be used in regional climate model version 4 (RegCM4). The five types of lateral boundary condition schemes used in this regional climate simulation are the fixed, time-dependent, sponge, and flow relaxation (linear and exponential flow relaxation) schemes.

4.4.1 Fixed LBSs

This is the simplest method that will not allow time variation of any atmospheric model variable (u) at the lateral boundaries during the simulation process which is given by

$$\frac{\partial u}{\partial t} + c\frac{\partial u}{\partial x} = 0 \tag{4.4}$$

This method is not suitable for the long-time scale research because of that, information outside from domain of interest cannot be imported to the simulated region inside. To minimize this effect of lateral boundaries, the lateral boundary should be apart from the domain of interest as far as possible.

4.4.2 Time dependent LBSs

This boundary conditions consist of large-scale time-varying tendencies linearly combined with model calculated tendencies. It is necessary to interpolate the large-scale tendencies in time and space inorder to obtain the boundary condition tendencies.

From Perkey & Kreitzberg (1976), the prediction for any dependent atmospheric model variable u can be written as

$$u_n(I) = u_p(I) + W(I)\frac{\partial u_m}{\partial t}|_I \nabla t + [1 - W(I)]\,\frac{u_{ls}}{\partial t}|_I \nabla t \tag{4.5}$$

where the subscript n and p denotes the new value after the boundary condition and previous value at a former time. ls denote the large-scale tendency of u, m denote the model calculated tendency, and W(I)'s are the weighting coefficients which is described

as

$$W(I) = \begin{cases} 0.0 \text{ for I= the boundary grid points} \\ 0.4 \text{ for I=the boundary-1 grid points} \\ 0.7 \text{ for I=the boundary-2 grid points} \\ 0.9 \text{ for I=the boundary-3 grid points} \\ 1.0 \text{ for I=all other interior grid points} \end{cases} \tag{4.6}$$

Thus, the value at the boundaries is completely specified by the large scale imposed value. If $\partial u_{ls}/\partial t$ is zero, the above equations will reduced to the sponge boundary condition.

4.4.3 Sponge LBSs

An outgoing waves that pass out of the region of interest without reflection can be considered as good behaved waves. As with all absorbing-layer approaches to open boundary conditions, the computational domain is extended beyond the domain of interest to include an absorbing zone within which the governing equations are modified by the addition of dissipative terms. The computational boundary becomes the outer boundary of the absorbing layer, and the interface between the domain of interest and the absorbing layer marks a transition in the nature of the equations that are to be solved.

From Lavelle & Thacker (2008) the evolution of an initially motionless Gaussian-shaped fluid is described by the linear shallow-water wave equations:

$$\begin{aligned} \frac{\partial h}{\partial t} + \frac{\partial (Hu)}{\partial x} + \frac{\partial (Hv)}{\partial y} &= 0, \\ \frac{\partial u}{\partial t} + g\frac{\partial h}{\partial x} - fv &= 0, \\ \frac{\partial v}{\partial t} + g\frac{\partial h}{\partial y} + fu &= 0, \end{aligned} \tag{4.7}$$

where h is surface elevation, u and v are components of the velocity in the x-and y-direction, respectively, t is time, H is the basin depth, g is the acceleration due to gravity, and f is the Coriolis parameter accounting for the influence of earth's rotation on the flow.

Good results can be anticipated using perfectly matched layers, as they are designed to prevent reflections of outgoing waves. The perfectly matched layer can be derived from a complex coordinate transformation, which can be summarized by the replacements (

Lavelle & Thacker, 2008):

$$\begin{aligned} \frac{\partial}{\partial x} &\rightarrow \frac{\partial}{\partial x} \Big/ \left(1 + \sigma_x \frac{\partial^{-1}}{\partial t}\right), \\ \frac{\partial}{\partial y} &\rightarrow \frac{\partial}{\partial y} \Big/ \left(1 + \sigma_y \frac{\partial^{-1}}{\partial t}\right), \end{aligned} \tag{4.8}$$

where $\frac{\partial^{-1}}{\partial t}$ is the temporal anti-derivative operator, and σ_x and σ_y are the absorption coefficients across the x and y directions respectively and are also functions of x and y, they grow from zero within the region of interest, absorbing waves more strongly the deeper they penetrate into the layer. For absorbing layers crossing the x-axis, the first equation of equation (4.8) should be used; for those crossing the y-axis, the second equation of equation (4.8); and for the corners, both should be used (see Figure 4.1). The thickness of the layer and the strength of the absorption affect the chances that the wave might reflect at the outer boundary.

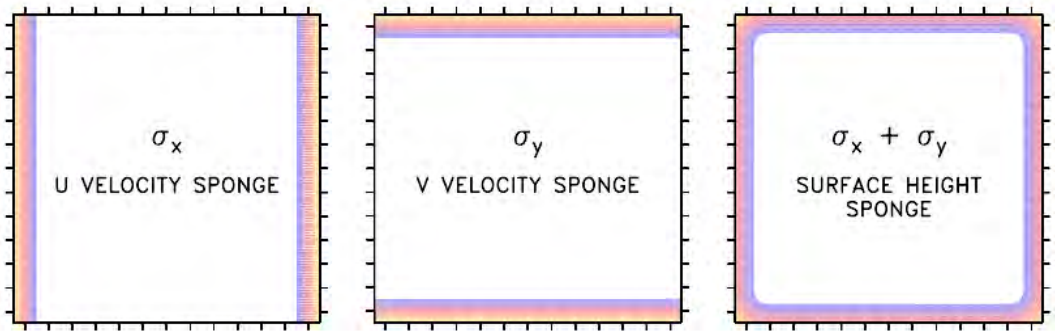

Figure 4.1: Contours of absorption coefficients for the perfectly matched layers, which are the same as those for the pretty good sponge. There is no absorption of the component of velocity parallel to the boundaries, and the rate at which the normal component is absorbed increases with distance into the absorbing zone. Surface height is absorbed at all open boundaries, and the sum $\sigma_x + \sigma_y$ has contribution from both terms only in the corners (Lavelle & Thacker, 2008).

When applied to shallow-water wave equations linearized about the no-flow state for

a perfectly matched layer yields

$$\begin{aligned}
&\frac{\partial h}{\partial t} + \frac{\partial (Hu)}{\partial x} + \frac{\partial (Hv)}{\partial y} = -\left(\sigma_x + \sigma_y\right) h - \sigma_x \sigma_y q_h - \sigma_y \frac{\partial (Hq_u)}{\partial x} - \sigma_x \frac{\partial (Hq_v)}{\partial y}, \\
&\frac{\partial u}{\partial t} + g\frac{\partial h}{\partial x} - fv = -\sigma_x u + \sigma_x f q_v, \\
&\frac{\partial v}{\partial t} + g\frac{\partial h}{\partial y} + fu = -\sigma_y v - \sigma_y f q_u,
\end{aligned} \qquad , \tag{4.9}$$

The terms on the left-hand side of the equations correspond to the original shallow-water wave equations, while those on the right are the modifications for the perfectly matched layers. The temporal anti-derivative operators in (4.8) necessitate new fields q_h, q_u, and q_v, which are governed by additional equations

$$\begin{aligned}
\frac{\partial q_h}{\partial t} &= h - \lambda q_h, \\
\frac{\partial q_u}{\partial t} &= u - \lambda q_u, \\
\frac{\partial q_v}{\partial t} &= v - \lambda q_v,
\end{aligned} \tag{4.10}$$

where the positive parameter λ has been introduced to control instability.

It is instructive to compare the perfectly matched layer to a simpler formulation like

$$\begin{aligned}
\frac{\partial h}{\partial t} + \frac{\partial (Hu)}{\partial x} + \frac{\partial (Hv)}{\partial y} &= -\sigma \left(h - h_e\right), \\
\frac{\partial u}{\partial t} + g\frac{\partial h}{\partial x} - fv &= -\sigma \left(u - u_e\right), \\
\frac{\partial v}{\partial t} + g\frac{\partial h}{\partial y} + fu &= -\sigma \left(v - v_e\right),
\end{aligned} \tag{4.11}$$

The absorption coefficient σ of the simple sponge acts on all variables, whereas by distinguishing between σ_x and σ_y the perfectly matched layer prevents absorption of v at x boundaries and absorption of u at y boundaries. Second, the simple sponge introduces no new fields. The absorption coefficient σ varies with x or y as appropriate, increasing with distance into the absorbing layers. While the simple sponge introduces a stable complex frequency via the transformation $\partial/\partial t \to \partial/\partial t + \sigma$.

If the auxiliary fields of the perfectly matched layer were all set to zero, equation (4.10) is not needed, and the remaining terms of equation (4.9), when generalized to allow for

an external solution, describe the pretty good sponge (Lavelle & Thacker, 2008):

$$\begin{aligned} \frac{\partial h}{\partial t} + \frac{\partial (Hu)}{\partial x} + \frac{\partial (Hv)}{\partial y} &= -\left(\sigma_x + \sigma_y\right)\left(h - h_e\right), \\ \frac{\partial u}{\partial t} + g\frac{\partial h}{\partial x} - fv &= -\sigma_x\left(u - u_e\right), \\ \frac{\partial v}{\partial t} + g\frac{\partial h}{\partial y} + fu &= -\sigma_y\left(v - v_e\right), \end{aligned} \tag{4.12}$$

Like the perfectly matched layer, only u and h are absorbed in the x-direction, and v and h in the y-direction, with σ_x varying with x and σ_y varying with y.

For all three methods boundary conditions must be specified at the outer limit of the absorbing zone. One possibility is to use radiation conditions to terminate the sponge layer, but if there has been sufficient absorption, that should not be necessary. With strong absorption the solution is forced toward the external solution, and as the increase over the last grid cell can be regarded as achieving an infinite absorption rate, the external solution can provide values at the boundary.

4.4.4 Flow relaxation LBSs

The principle of relaxation is that the flow is relaxed to the large-scale values in a buffer zone near the boundaries. The relaxation boundary scheme consists of progressively constraining the main prognostic variables of the regional model to match the corresponding large scale values in a buffer zone next to the lateral boundaries. The Newtonian relaxation factor and diffusive relaxation factor terms are commonly added to the internal model tendency for any atmospheric variable (Giorgi *et al.*, 1993; Marbaix *et al.*, 2003), which is described as:

$$\frac{\partial u}{\partial t} = ... - N(u_m - u_{LS}) + D\nabla^2(u - u_{LS}), \tag{4.13}$$

where $u_m = u_m(x, y, z, t)$ is one of the model variables for which information is incorporated from the large-scale, while u_{LS} is the equivalent variable from the large-scale (LS) data, with x = distance (perpendicular) to the boundary; $N = N(x)$ is the Newtonian relaxation factor; and $D = D(x)$ is the diffusive relaxation factor.

The Newtonian relaxation (Marbaix *et al.*, 2003), continuously removes a fraction of the difference between the model and large-scale forcing. Mass and waves enter the

domain correctly because the modeled field is equal to the forcing at the boundary, and departures from that situation are only damped in the buffer zone. On the other hand, for outgoing perturbations the relaxation provides a progressive damping toward the large-scale condition. Intuitively, this damping explains that the noise problem that may result from over-specification is mitigated.

The diffusive relaxation term is also based on the difference between the regional model and the forcing data, but it's effect is to diffuse that difference horizontally. Note that this is not the same as the diffusive boundary zone in which the diffusion term is applied to the model solution. In the diffusive relaxation scheme, the diffusion is applied to the difference between modeled and large-scale fields. This is important because the purely diffusive scheme may degrade the incoming flow and is very sensitive to numerical shortcomings (Marbaix *et al.*, 2003). In contrast, relaxation diffusion should have the advantages of the Newtonian relaxation explained above. The Newtonian term is included in all models using a relaxation formulation, and most models also include the diffusive relaxation term (Davies, 1983; Giorgi *et al.*, 1993).

The Newtonian relaxation factor N(j) can be stated as a function of the number of relaxation points (s) and the number of grid points (j) from the lateral boundaries (Giorgi *et al.*, 1993; Marbaix *et al.*, 2003) as:

$$N(j) = \begin{cases} \frac{s+1-j}{s-1}, \rightarrow \text{for } \textbf{linear relaxation} \text{ scheme} \\ \exp\left(\frac{2-j}{M}\right), \rightarrow \text{for } \textbf{exponential relaxation} \text{ scheme} \end{cases} \tag{4.14}$$

where M is a constant.

4.5 Experiment design and methodology

The experiment domain and surface elevation for RegCM4 simulations is shown in Fig. 4.2c which covers most of the African continent found between -40 west to 80 east and 26 north to 25 south and exhibits very complex and high terrains (more than 2,000m) especially in the Ethiopian highland regions. This domain includes the Indian ocean that contributes the main source of east African rainfall. The domain contains the domain of interest that includes ten east African countries (Sudan, Eritrea, Ethiopia, Djibouti, Somalia, Kenya, Uganda, Burundi, Rwanda, and Tanzania) and comprises $20^0E - 52^0E$

and $12^0S - 22^0N$ shown in Fig. 4.2a which are nested in the larger domain. The domain of interest for the simulation has been divided into elven sub-regions (clusters) for the analysis presented as shown in Fig. (4.2b). The analysis will be handled to all the elven clusters. The experiment lateral boundaries are set far away from the domain of interest in order to reduce the influence of the time-dependent inflow/outflow boundary conditions over the domain and to be able to capture the important aspects of extra-tropical systems that influence the African climate. This domain includes large topographies that exhibit some complex terrains like Ethiopian and Kenyan highlands.

For this study, five different simulations of the east African present-day rainfall climatology are performed with RegCM4 using ERAIN at the boundaries for the five different lateral boundary condition schemes as stated above. The model is integrated for 20 years from January 1989 through December 2008 at a spatial horizontal resolution of 60 km with 18 vertical levels and 224×96 grid cells. The domain cartography is projected using Normal Mercator (NORMER).

The results obtained from all the five simulation experiments are compared with the observed variables obtained from East Anglia Climate Research Unit (CRU) and Global Precipitation Climatology Project (GPCP) to determine the statistical evaluations which are briefly explained in section 4.6. The statistics are then compared to differentiate those errors originating from RegCM4 lateral boundary condition schemes. The model statistics are investigated on an inter-annual time scale and are computed for the entire east Africa for each subregions.

4.6 Statistical Measures

Different statistical measures have been used to evaluate the performance of different climate models quantitatively. Willmott *et al.* (1985) and Segele *et al.* (2008) provides an analysis of the suitability of several of these measures. In this study, the model performance is evaluated against observations using several statistical techniques, such as the bias, root mean square error (RMSE), correlation, and correlation significance error.

The bias is given by

$$Bias = \overline{M} - \overline{O} \tag{4.15}$$

where $\overline{M}$ is the mean of the modeled values and $\overline{O}$ is the mean of the observed climatology.

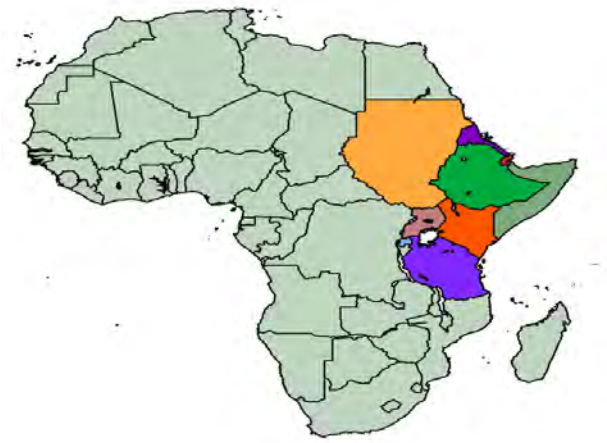

a

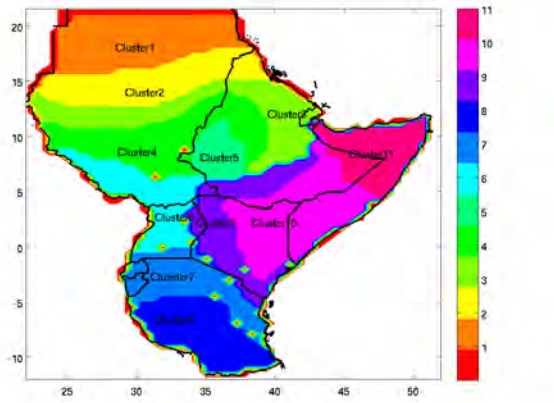

b

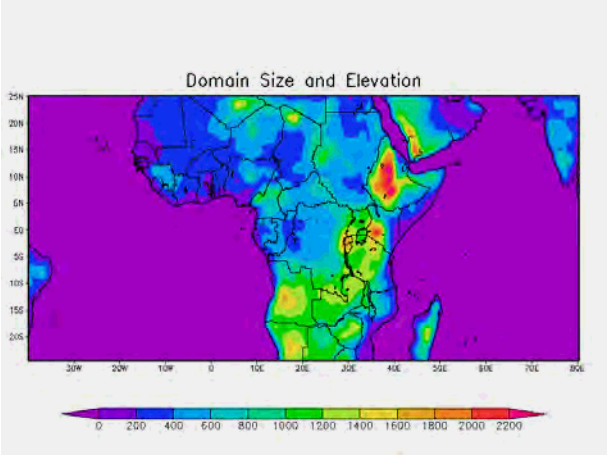

c

Figure 4.2: East African a) countries b) classification of climatic echo-regions, and c) model domain showing national boundaries and surface elevation (m) for RegCM4 at 60 km horizontal resolution

The root mean square error (RMSE) is a frequently used measure of the differences between values predicted by a model and the values actually observed from the variables being modeled. The RMSE is given by

$$RMSE = \sqrt{\frac{1}{N}\sum_{i=1}^{N}(O_i - M_i)^2} \tag{4.16}$$

where N is the number of observed (O) and modeled (M) values being compared. Here, N is the number of RegCM4 grid cells in the domain. Climatological values are used in calculating the RMSE.

In order to evaluate the spatial agreement between modeled and observation variables quantitatively, the pattern correlation coefficient R has been used. Correlation indicates the strength of a linear relationship between two variables as shown in Equation (4.17), between observed and simulated fields simply as the correlation of a series of data points from the observed field with corresponding values from the modeled field at a fixed time:

$$\rho_p = \frac{\sum(O_i - \overline{O})(M_i - \overline{M})}{\sqrt{(\sum(O_i - \overline{O})(\sum M_i - \overline{M})}} \tag{4.17}$$

Chapter 5

Data Analysis

5.1 Rainfall Climatology

This chapter examines the rainfall climatologies that are obtained from the RegCM4 simulation for five different lateral boundary schemes (LBSs) using ERA-interim (ERAIN) as a lateral boundary forcing dataset. The results of model rainfall climatologies from all LBSs are compared with GPCP and CRU rainfall for the mean, seasonal mean, annual mean, and inter-annual time scale.

5.1.1 Mean Rainfall Climatology

In this section the simulated, CRU and GPCP rainfall climatologies are averaged over the whole domain of simulation for 20 years (1989-2008). The spatial distribution of each averaged simulation rainfall climatologies are compared with observed rainfall over the entire domain. The simulated monthly rainfall climatology is derived from five independent model runs using RegCM4 for five different LBSs. The GPCP and CRU rainfall climatologies have been used to derive the observed climatology. The comparison of the simulated mean rainfall climatologies with the GPCP and CRU mean rainfall climatologies are shown in Figs. 5.1 - 5.5 for exponentially flow relaxation, sponge, time dependent, linearly flow relaxation and fixed LBSs (upper panels) with the corresponding biases (lower panels) with respect to GPCP and CRU respectively.

Fig. 5.1 shows the distribution of mean rainfall climatology for GPCP (a), CRU (b), the exponential LBS (c), and the bias of exponential LBS from GPCP (d) and

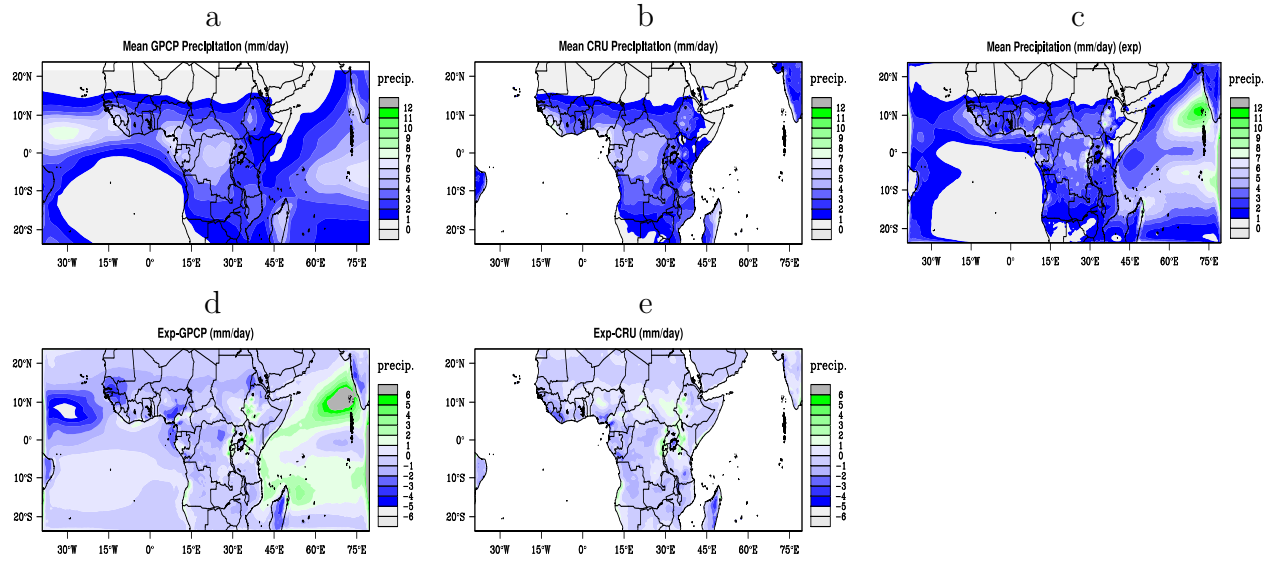

Figure 5.1: Mean 1989-2008 rainfall from GPCP (a), CRU (b), Exponential (c), Exponential minus GPCP differences (d), and Exponential minus CRU difference (e)

CRU (e) over the entire domain averaged for 20 years (1989-2008). The exponential LBS rainfall climatology reproduces the structure of spatial distribution of the observed rainfall climatologies very well. The exponential LBSs overestimates over east African highlands and Indian ocean, although it underestimates over central Africa, southeast Tanzania, and over the convergence zone of Atlantic ocean. The exponential LBS shows a significant wet bias over west and southwest part of Ethiopia, Kenyan highland, Burundi, Rwanda ans western Uganda. It also shows large dry bias over the convergence zone of Atlantic ocean, west African coast, Nigeria, Cameron coast, northeast Ethiopia and over Madagascar. For the remaining part of the the domain the bias is insignificant.

The sponge LBS (see Fig. 5.2) also reproduces the structure of observed mean rainfall climatology spatial distribution over most areas of the domain and captures a relatively higher rainfall patterns over the convergence zone of Atlantic and Indian ocean than the exponential LBS. The rainfall bias is relatively low over peak rainfall regions as compared to the bias shown in exponential LBS. The sponge LBS also captures a wet bias over the region of low rainfall than the exponential LBS which shows a dry bias over this regions.

On the other-hand, the time dependent LBS of Fig. 5.3 shows the same feature in reproducing the observed mean rainfall distributions as the the exponential and sponge

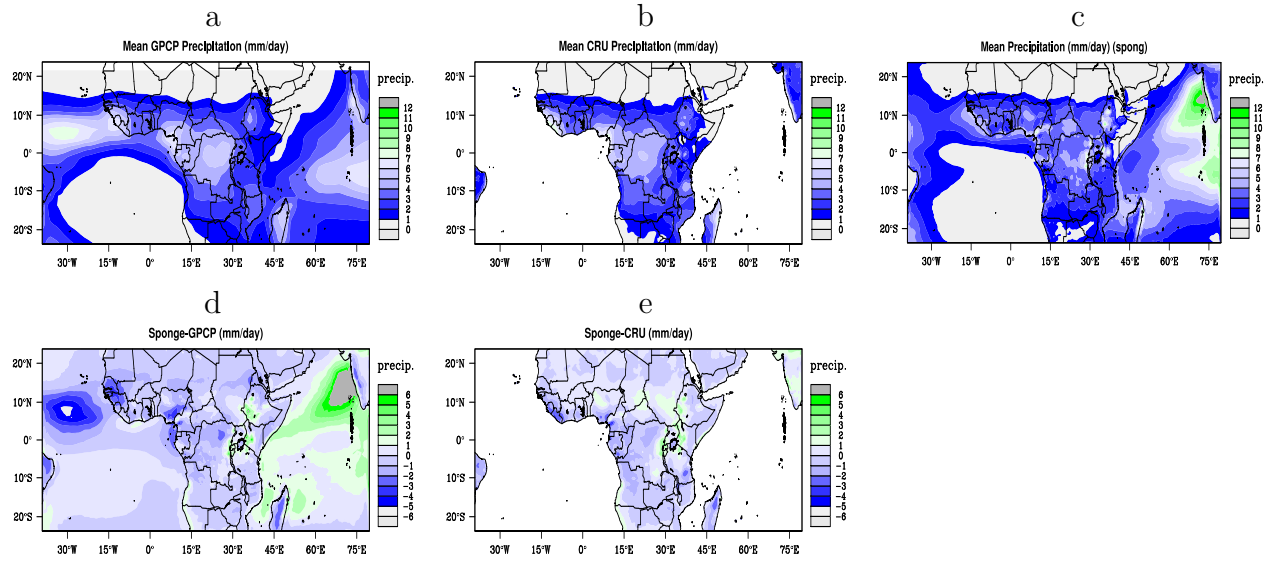

Figure 5.2: Mean 1989-2008 rainfall from GPCP (a), CRU (b), Sponge (c), Sponge minus GPCP differences (d), and Sponge minus CRU difference (e)

LBSs over most regions. However, the time dependent LBS overestimates over some equatorial Africa countries especially over Ethiopian highlands and underestimates over the convergence zone of Atlantic ocean as compared to the exponential and sponge LBSs. This LBS captures larger biases over the mentioned regions and shows a dryer bias over some part of Somalia and Tanzania. The time dependent LBS also shows high disturbances at the boundaries of the domain. This disturbances might be due to the reflection of long waves at the boundary. This reflection might also be due to the time dependent LBS that does not allow the time variation of field variable at the boundary grid point.

The linear relaxation LBS shown in Fig. 5.4 also captures the observed mean rainfall climatology spatial distributions. However, this LBS shows extremely large wet bias over the buffer zone which is not captured by any of the other LBS. This might be due to the incapability of the linear relaxation LBS in removing the disturbances that enter from the large scale region to the simulation domain in the buffer zone. This may lead to wrong result when applying for small domain in which the simulation of interest is too near to the buffer zone than the one used here.

The simulated mean rainfall climatology generated using the fixed LBS (Fig. 5.5) shows more or less the same feature like that of the time dependent LBS. This similar

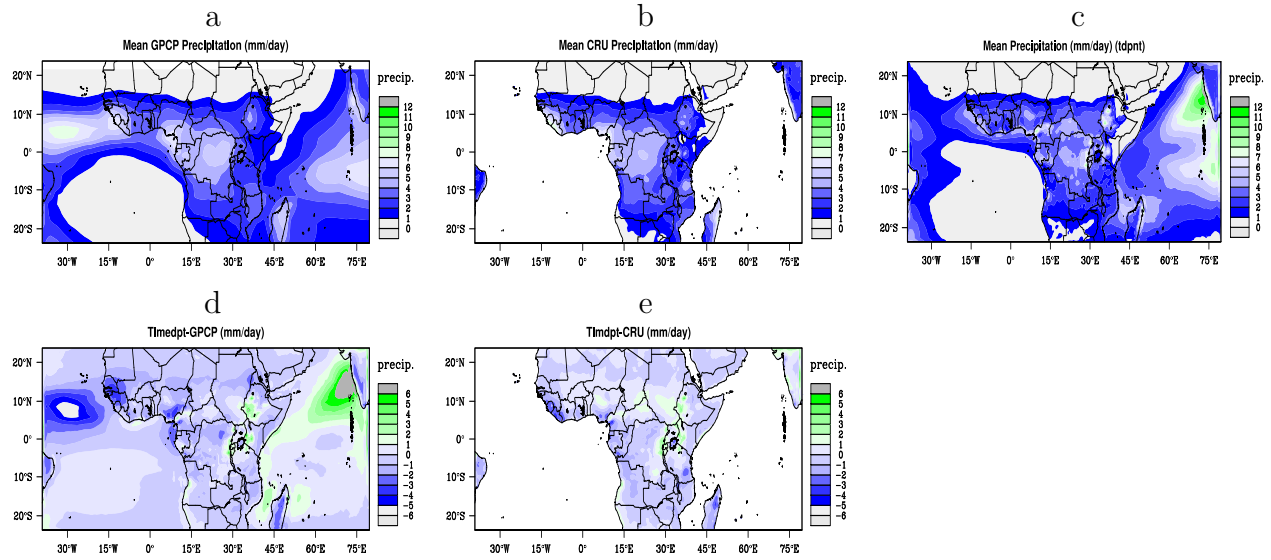

Figure 5.3: Mean 1989-2008 rainfall from GPCP (a), CRU (b), Time Dependent (c), Time Dependent minus GPCP differences (d), and Time Dependent minus CRU difference (e)

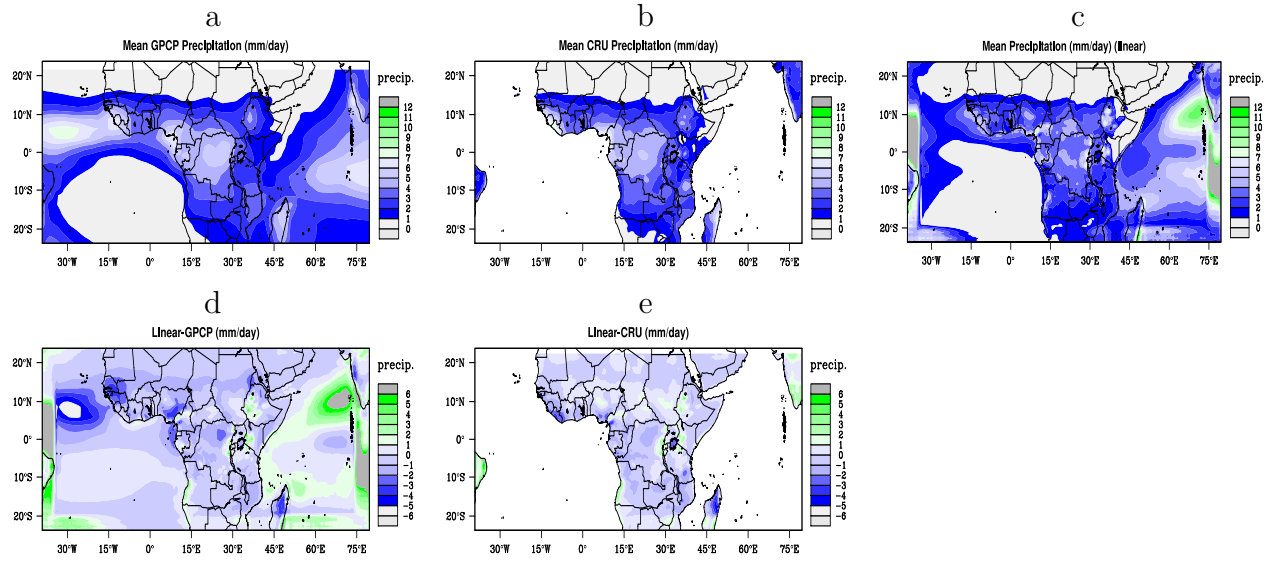

Figure 5.4: Mean 1989-2008 rainfall from GPCP (a), CRU (b), Linear (c), Linear minus GPCP differences (d), and Linear minus CRU difference (e)

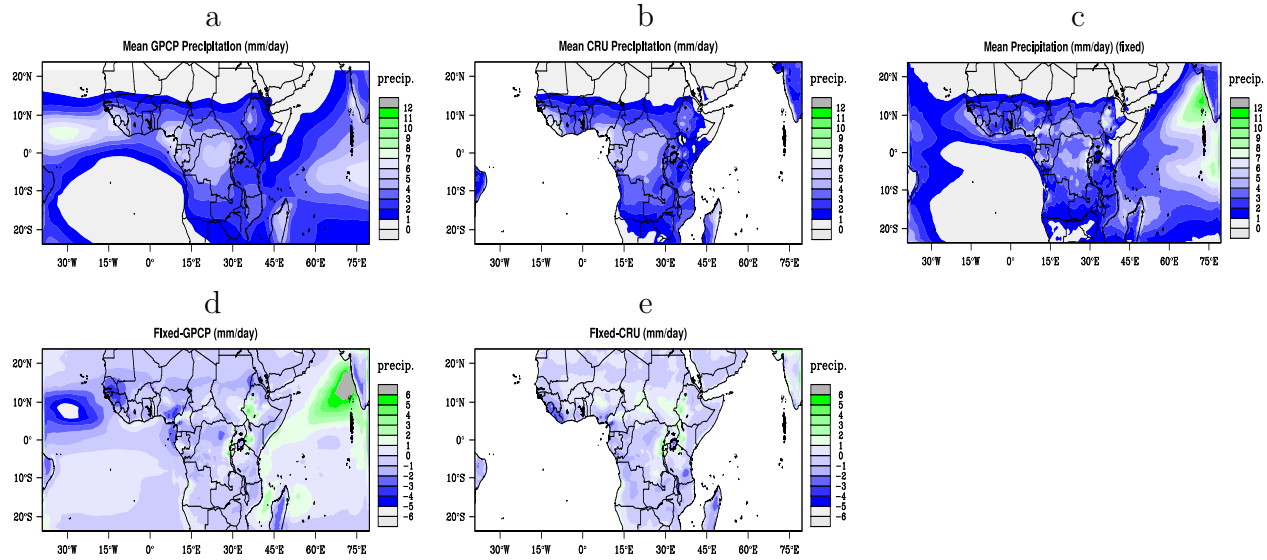

Figure 5.5: Mean 1989-2008 rainfall from GPCP (a), CRU (b), Fixed (c), Fixed minus GPCP differences (d), and Fixed minus CRU difference (e)

features might arose from the nature of the two LBSs in which both of them do not allow the time variation of model variables at the boundary grid points. However, the results with the time dependent LBS is not bad which might be due to the larger domain in which the model can make its own circulation inside the domain.

Overall, the simulated mean rainfall climatologies for all the five LBSs capture the regions of maximum rainfall located over and near the equatorial region of the domain that is consistent with the observed rainfall climatology. However, unlike the observed climatology, relatively drier conditions are simulated over eastern parts of Kenya, north eastern and south eastern parts of Ethiopia, the convergence zone of Atlantic ocean, Eritrea, south Tanzania, and over southwest of Somalia in all cases. It is also shown that the simulated mean rainfall climatologies using all the five LBSs capture a strong wet bias over the entire Indian ocean. Significant differences between simulated and observed rainfall amounts also exist over south Sudan, Ethiopian and Kenyan highlands. This large biases especially over the convergence zone of Atlantic ocean (large dry bias) and Indian ocean (large wet bias) may be the incapability of RegCM4 with 60km horizontal resolution to capture the strong mesoscale circulation systems and the subsequent strong conventions there. All the simulated mean rainfall climatologies show both wet and dry biases over

different region of the domain. The bias of the simulated mean rainfall climatologies from GPCP are larger than the biases from CRU. The larger bias of the simulated mean rainfall climatologies with respect to the GPCP climatology may be due to the coarse resolution of GPCP in representing the finer scale climatologies. There is also a difference between the model runs where, the sponge and exponentially flow relaxation LBS simulates relatively higher rainfall amounts over the convergence zone of Atlantic ocean, Indian ocean,and some part of Tanzania as compared with the amount of rainfall simulated in fixed, time dependent, and linearly flow relaxation LBS. Among the RegCM4 simulations, the linear relaxation LBS shows high disturbance at the lateral boundaries. Although it is low, there is also disturbance at the boundaries in case of exponential, time dependent, and fixed LBS. The sponge LBS shows that the disturbance at the boundaries is insignificant. As a result, the sponge LBS captures an overall good mean rainfall climatologies that are shown in the observed rainfall climatologies than the rest LBSs. The differences between the simulated mean rainfall climatologies at the boundaries and interior of the domain is due to the differences between the LBS's adjustment of the large scale tendencies at the buffer zone towards the center of the simulation domain.

5.1.2 Seasonal Mean Rainfall Climatology

In this section the mean seasonal cycle of simulated spatial rainfall distributions superimposed with the corresponding near surface wind vector (10m wind) and the observed rainfall has been examined for June-August (JJA), September-November (SON), December-February (DJF), and March-May (MAM). The bias of the simulated mean seasonal rainfall climatologies from the observed GPCP and CRU mean seasonal rainfall climatologies has been discussed for each season.

In JJA the observed rainfall is located mostly north of the equator and equatorial Africa following the migration of ITCZ which reaches its northernmost position in JJA. Figs. 5.6 - 5.10 show the comparison of the JJA mean rainfall climatologies (upper panel) and bias (lower panel) of the exponential, sponge, time dependent, linear and the fixed LBSs with the observed rainfall climatologies respectively. During JJA both GPCP and CRU captures the peak rainfall pattern around the Guinea highlands, at the boarder of Nigeria and Cameron, and Ethiopian highlands. The peak values are related to orographic features and convection of dry and moist Easterlies. GPCP does

not show any heavy rainfall over the boarder of Nigeria and Cameron and Ethiopian highlands, even the region of maximum rainfall is small over the Guinea highlands. This might be attributed to its coarse resolution to capture the fine scale rainfall distributions. The GPCP and CRU rainfall patterns are well captured by RegCM4 rainfall over most regions of the domain. The width of the rain belt (although it is slightly narrower) and location of maximum and minimum rainfall are well represented in the simulation, but the intensity is slightly overestimated over Ethiopian highlands, southern Sudan, southern Chad, Nigeria, Cameron, Kenya highlands, and Indian ocean. IN JJA the simulated rainfall shows a relatively large wet bias over Ethiopian highlands, west Kenya, and south Sudan while the dry bias are located over the northern part of the democratic republic of Congo, northeast of Ethiopia relative to both GPCP and CRU. It has been also shown that the simulated rainfall shows a dry bias north of equator (around 12^o-18^oN) and over the convergence zone of Atlantic ocean relative to GPCP (it might be related to coare resolution of GPCP), especially over the convergence zone of Atlantic, Senegal, northwest Guinea, Guinea-Bissau, southern boarder of Mauritania, southwest Mali, and over the Sudan and Eritrea boarder, the bias is large which is not shown relative to CRU. The JJA rainfall is well represented by the simulated rainfall using the sponge LBS with a relatively low bias from both GPCP and CRU (especially over Ethiopian highlands) as compared to the other LBSs.

During SON the ITCZ starts moving towards south resulting the decrease in the strength as well as the intensity of rainfall north of equator and equatorial Africa. Figs. 5.11 - 5.15 show the southward motion of SON rainfall with ITCZ for each of the five LBSs and observations. During SON the rainfall distribution is very sparse over the whole domain relative to the JJA rainfall pattern which is mainly confined over central Africa and coast of Guinea. RegCM4 simulations have well reproduced the observed SON rainfall, although there are some overestimation over western Ethiopia, central African tropical forest and underestimation over the convergence zone of Atlantic ocean, Sierra Leone, Equatorial Guinea, Cameron coast, and Somalia. From the simulated rainfall, the exponential and sponge LBS are good at reproducing the observed rainfall pattern especially over the convergence zone of Atlantic ocean. The bias of the simulated SON rainfall relative to both GPCP and CRU shows almost similar pattern with small difference on the peak values of both wet and dry bias. However, the sponge LBS captures narrower regions over the region of peak both wet and dry biases than the remaining LBSs. In

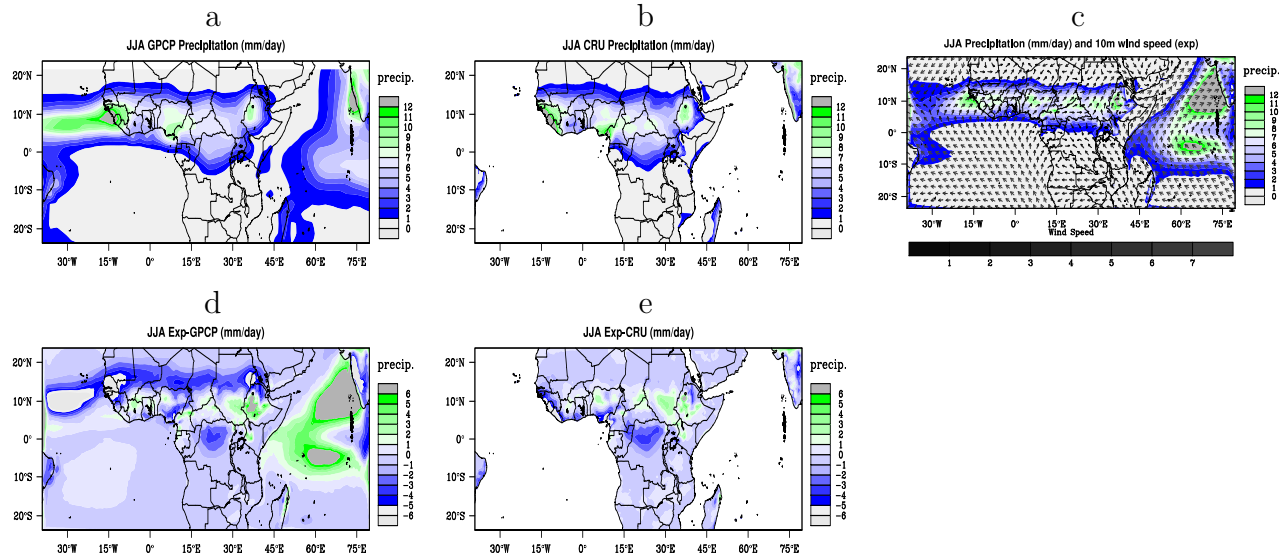

Figure 5.6: The JJA Mean 1989-2008 rainfall from GPCP (a), CRU (b), exponential (c), exponential minus GPCP differences (d), and exponential minus CRU difference (e)

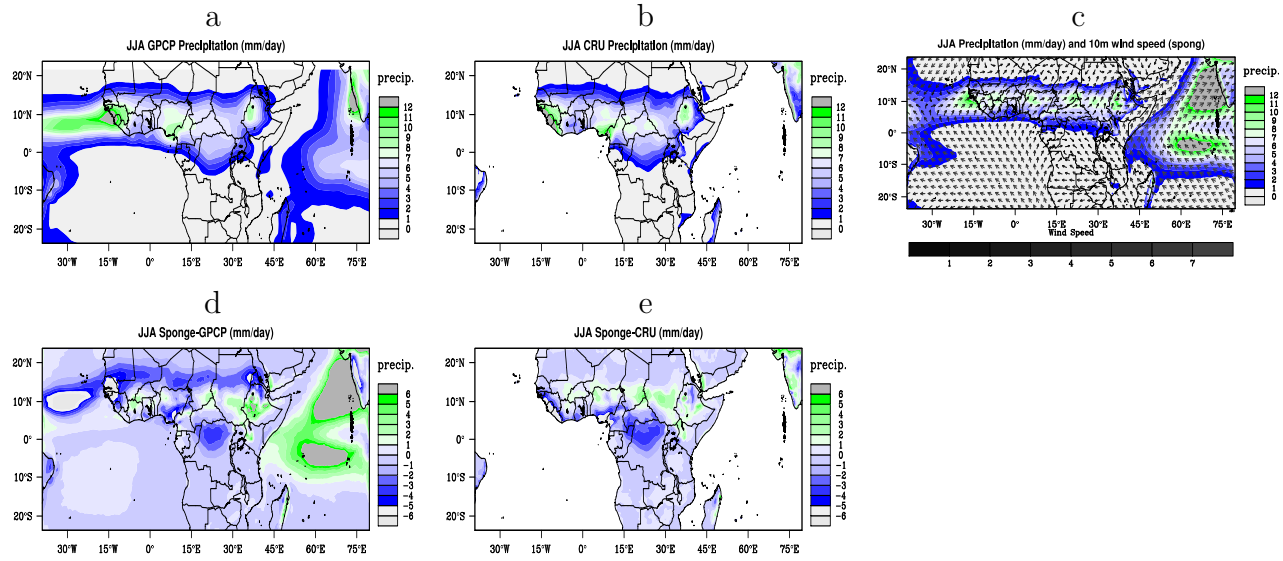

Figure 5.7: The JJA Mean 1989-2008 rainfall from GPCP (a), CRU (b), sponge (c), sponge minus GPCP differences (d), and sponge minus CRU difference (e)

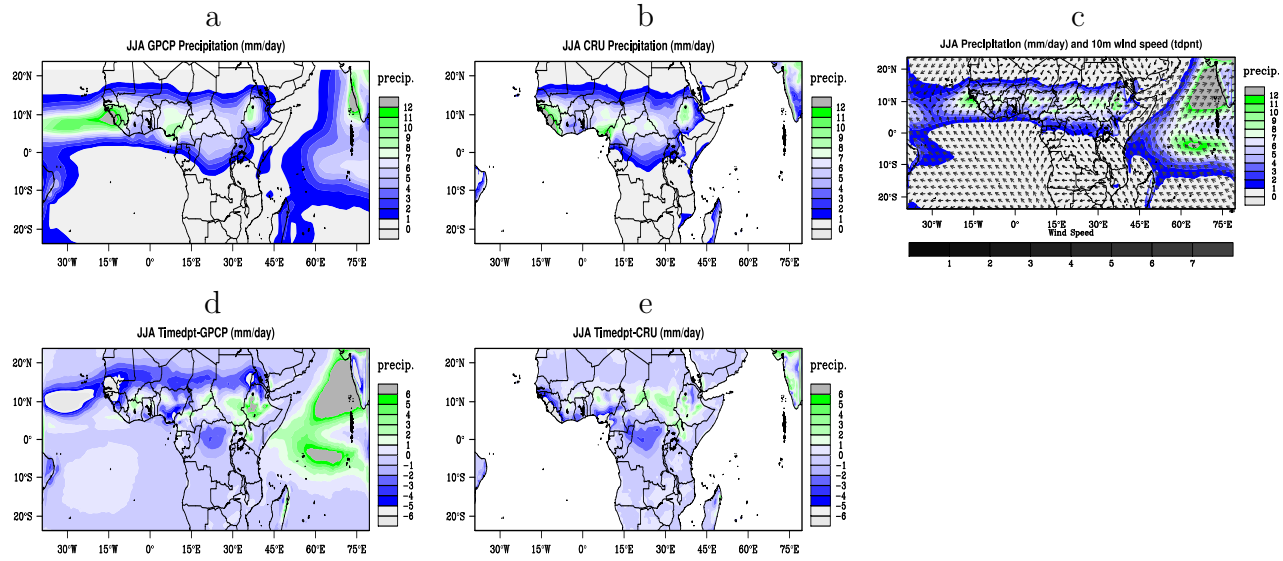

Figure 5.8: The JJA Mean 1989-2008 rainfall from GPCP (a), CRU (b), time dependent (c), time dependent minus GPCP differences (d), and time dependent minus CRU difference (e)

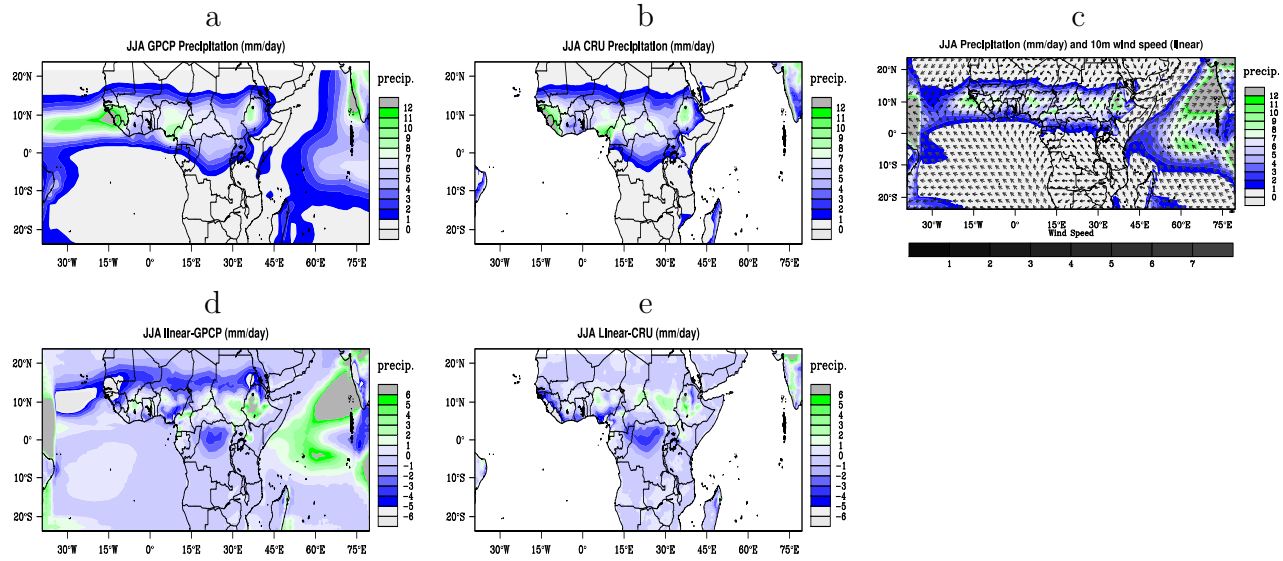

Figure 5.9: The JJA Mean 1989-2008 rainfall from GPCP (a), CRU (b), linear (c), linear minus GPCP differences (d), and linear minus CRU difference (e)

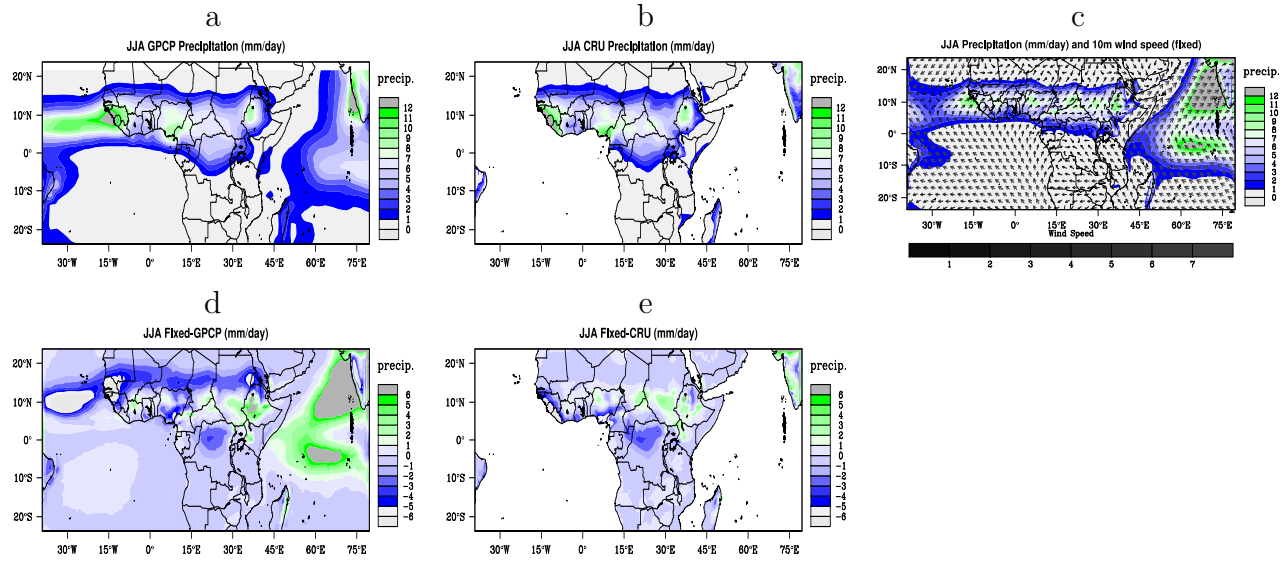

Figure 5.10: The JJA Mean 1989-2008 rainfall from GPCP (a), CRU (b), fixed (c), fixed minus GPCP differences (d), and fixed minus CRU difference (e)

SON, the peak wet biases are mostly confined over east Africa countries in particular over highland regions, where as the peak dry biases are located over the coast of Cameron, Gabon, and Liberia mostly over lowland regions.

In DJF the observed rainfall is located mostly south of the equator following the ITCZ which reaches its southernmost potion in DJF. Figs. 5.16 - 5.20 illustrate the region of the DJF mean rainfall climatologies for the observed and all five LBSs. This rainfall pattern is associated with moist southeasterly winds over the southern Indian Ocean and dry north-easterlies over the northern Indian Ocean converging over South Equatorial Africa and generating intense convection there. The RegCM4 output reproduces the major features of DJF precipitation south of equator over the convection regions of ITCZ. However, the model is drier than observed in the convergence zone of the equatorial Atlantic, Malawi, Mozambique and Madagascar. RegCM4 simulations also shows wetter features over Democratic republic of Congo, Burundi, and in the Indian Ocean north of Madagascar. The dry bias is connected to weaker easterlies from the north and south Atlantic while the wet bias seems to be associated with stronger easterlies in the Indian Ocean. Over the southern part of African continent the main precipitation bands are well captured by RegCM4 simulations. In this season all the simulated rainfall capture almost

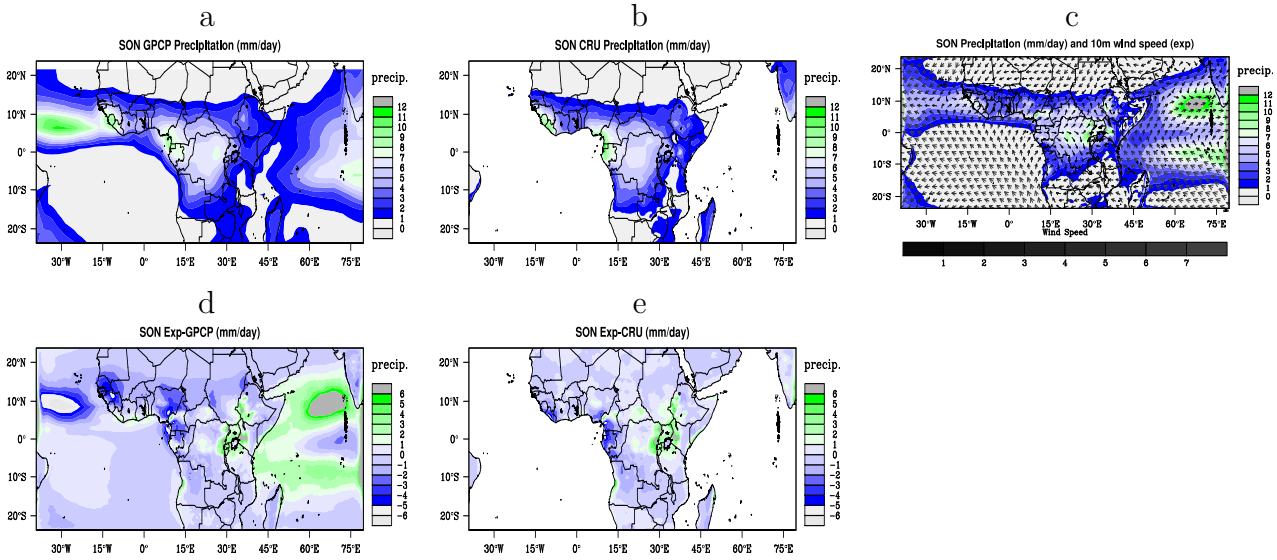

Figure 5.11: The SON Mean 1989-2008 rainfall from GPCP (a), CRU (b), exponential (c), exponential minus GPCP differences (d), and exponential minus CRU difference (e)

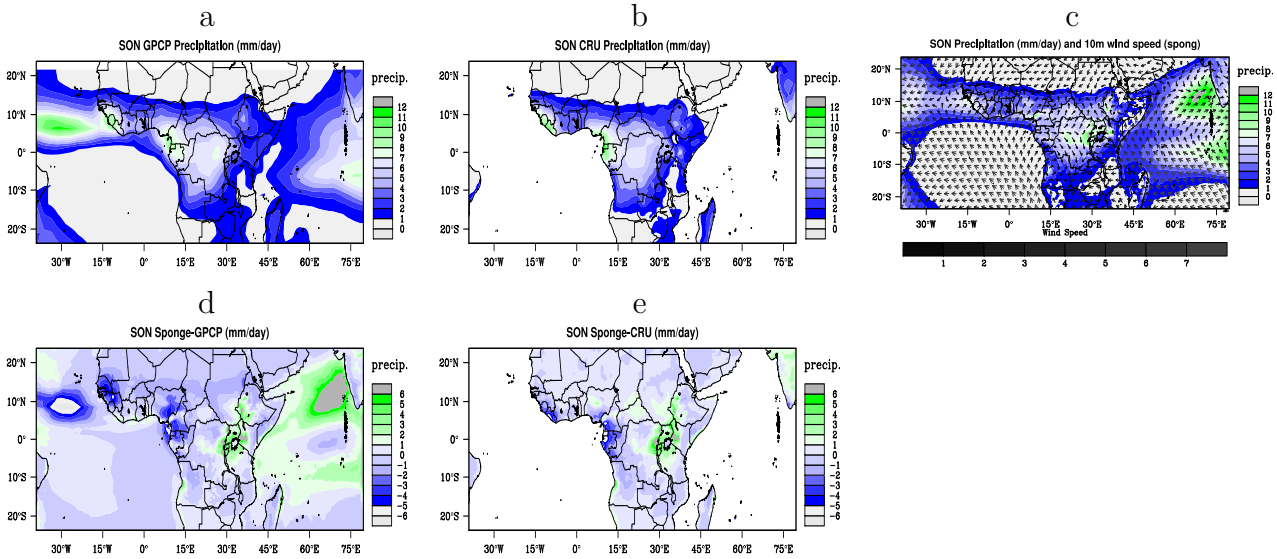

Figure 5.12: The SON Mean 1989-2008 rainfall from GPCP (a), CRU (b), sponge (c), sponge minus GPCP differences (d), and sponge minus CRU difference (e)

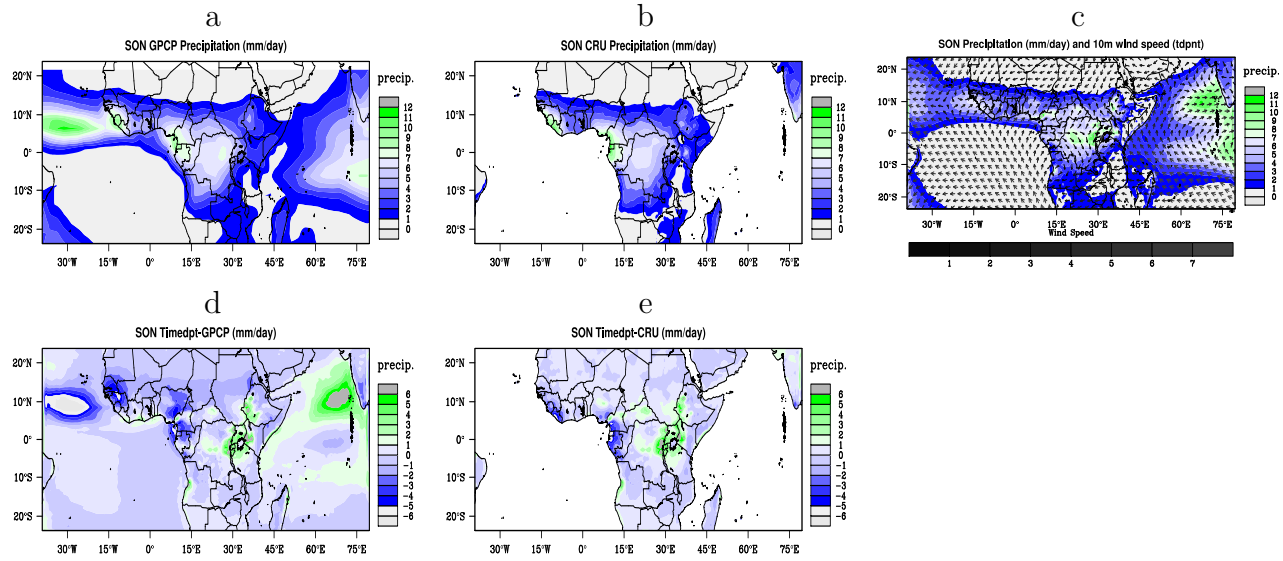

Figure 5.13: The SON Mean 1989-2008 rainfall from GPCP (a), CRU (b), time dependent (c), time dependent minus GPCP differences (d), and time dependent minus CRU difference (e)

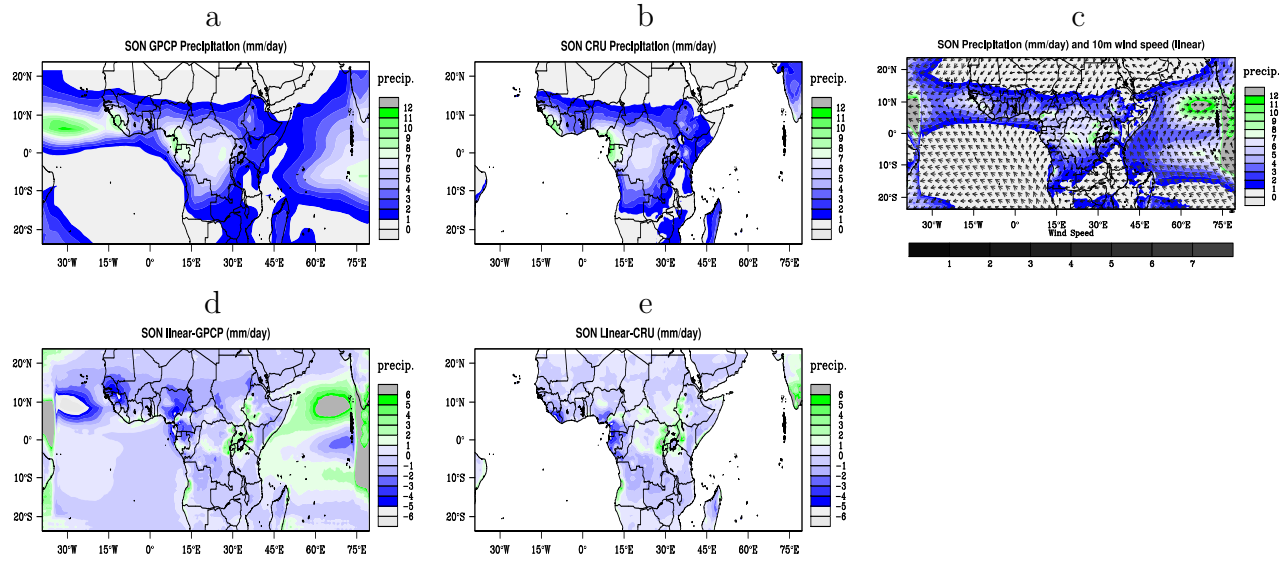

Figure 5.14: The SON Mean 1989-2008 rainfall from GPCP (a), CRU (b), linear (c), linear minus GPCP differences (d), and linear minus CRU difference (e)

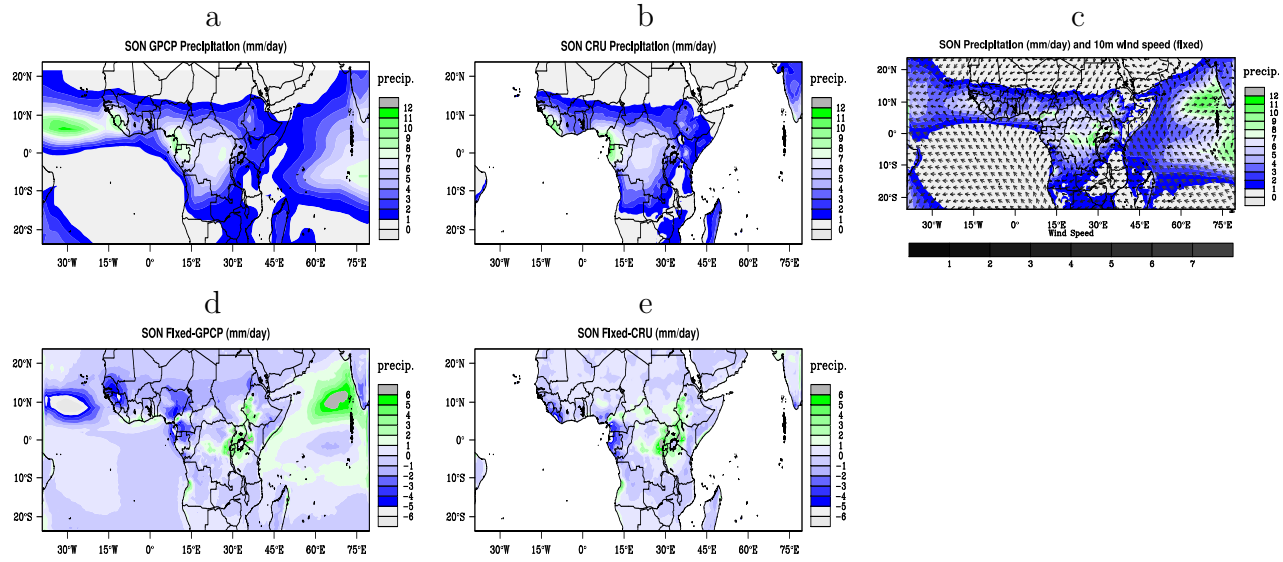

Figure 5.15: The SON Mean 1989-2008 rainfall from GPCP (a), CRU (b), fixed (c), fixed minus GPCP differences (d), and fixed minus CRU difference (e)

similar region of peak wet bias, while the sponge LBS captures a relatively small regions of peak dry biases with lower weight than the rest of the LBSs.

Unlike SON, MAM is the period for ITCZ moving northward with the corresponding decrease in rainfall weight on the southern parts of the domain. During MAM, the maximum rainfall mainly confined to the Cameron, equatorial Guinea, Gabon, the democratic republic Congo, southeast Tanzania, and southwest of Ethiopia. Like SON, the MAM rainfall distribution is sparse indicating that the strength of the MAM rainfall is weaker than the SON rainfall over most regions. The regional model simulations reproduces the MAM rainfall with slight overestimation over Cameron highlands, southwest Ethiopia, Kenyan highlands, and Cote D'Ivoire coast. RegCM4 also captures dry areas over the horn of Africa, Tanzania, and Madagascar, although all simulations lose the peak rainfall over southeast Tanzania. The biases also show similar features like the other seasons with sponge LBS captures small regions of peak dry bias.

Overall, RegCM4 simulations reproduce the seasonal mean spatial distribution of both the GPCP and CRU. The study also shows that RegCM4 captures the observed rainfall pattern over highland regions with slight overestimation and underestimates over the lowlands. It is also shown that, RegCM4 highly underestimates the observed rainfall over

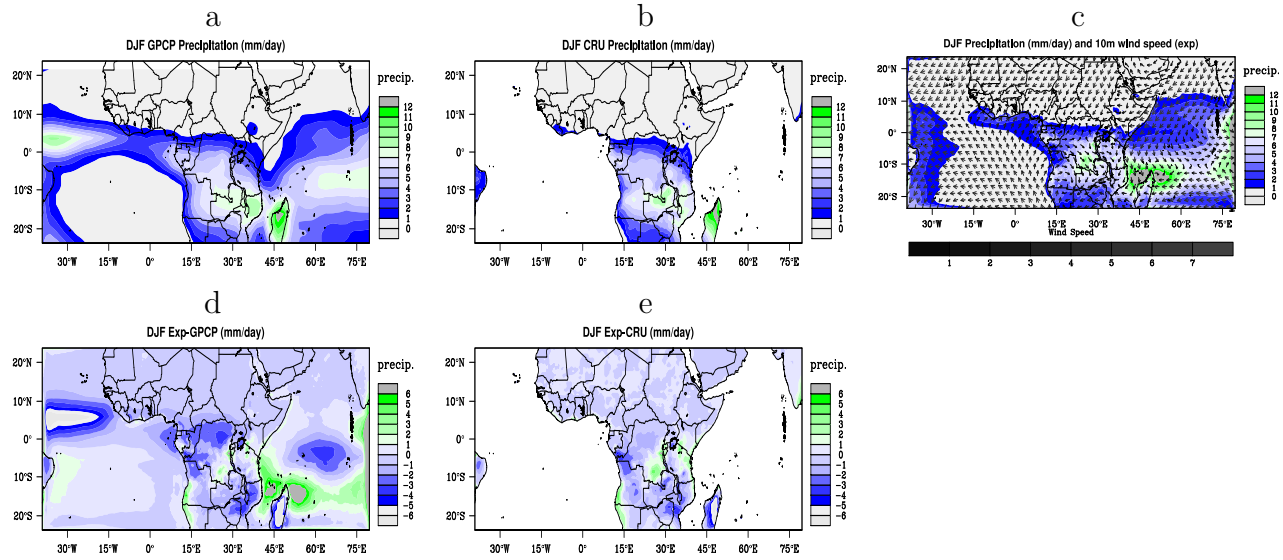

Figure 5.16: The DJF Mean 1989-2008 rainfall from GPCP (a), CRU (b), exponential (c), exponential minus GPCP differences (d), and exponential minus CRU difference (e)

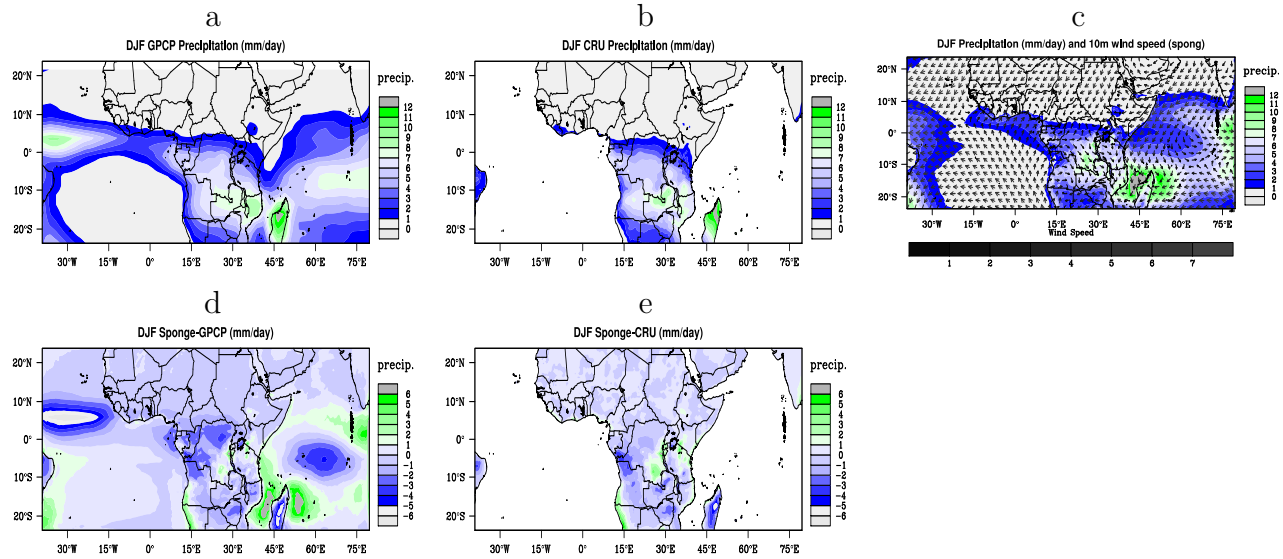

Figure 5.17: The DJF Mean 1989-2008 rainfall from GPCP (a), CRU (b), sponge (c), sponge minus GPCP differences (d), and sponge minus CRU difference (e)

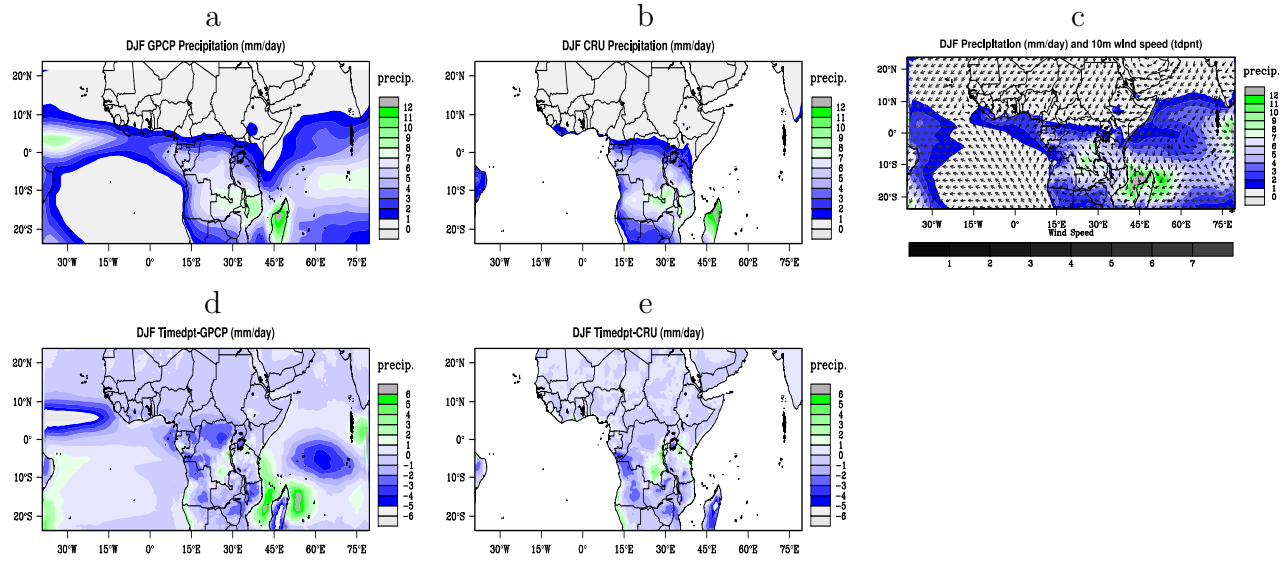

Figure 5.18: The DJF Mean 1989-2008 rainfall from GPCP (a), CRU (b), time dependent (c), time dependent minus GPCP differences (d), and time dependent minus CRU difference (e)

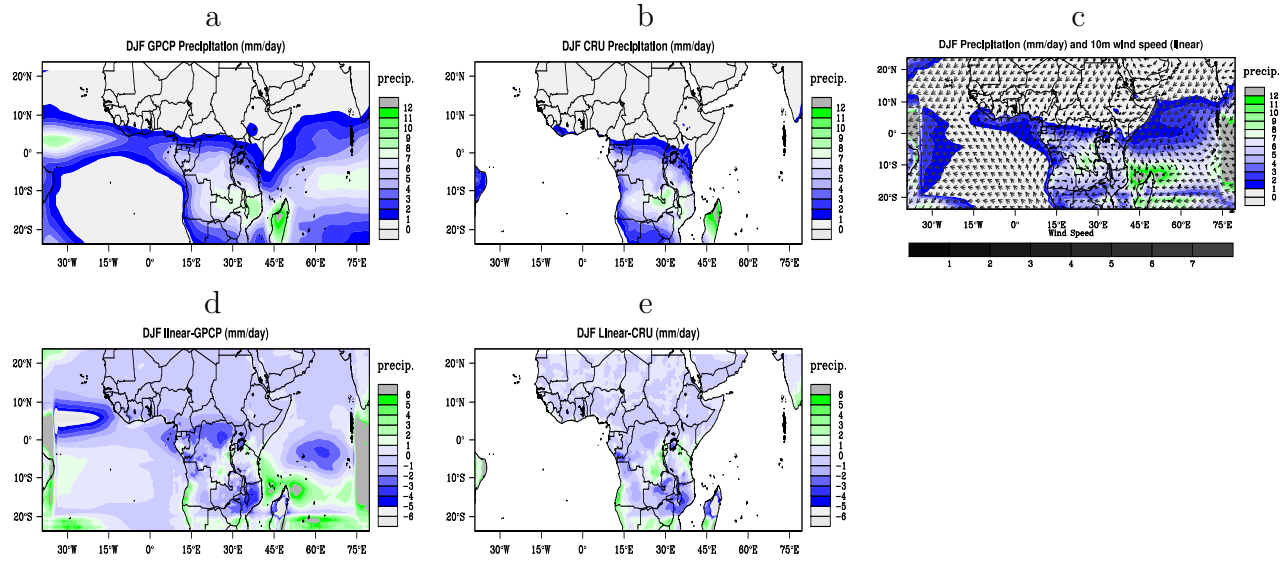

Figure 5.19: The DJF Mean 1989-2008 rainfall from GPCP (a), CRU (b), linear (c), linear minus GPCP differences (d), and linear minus CRU difference (e)

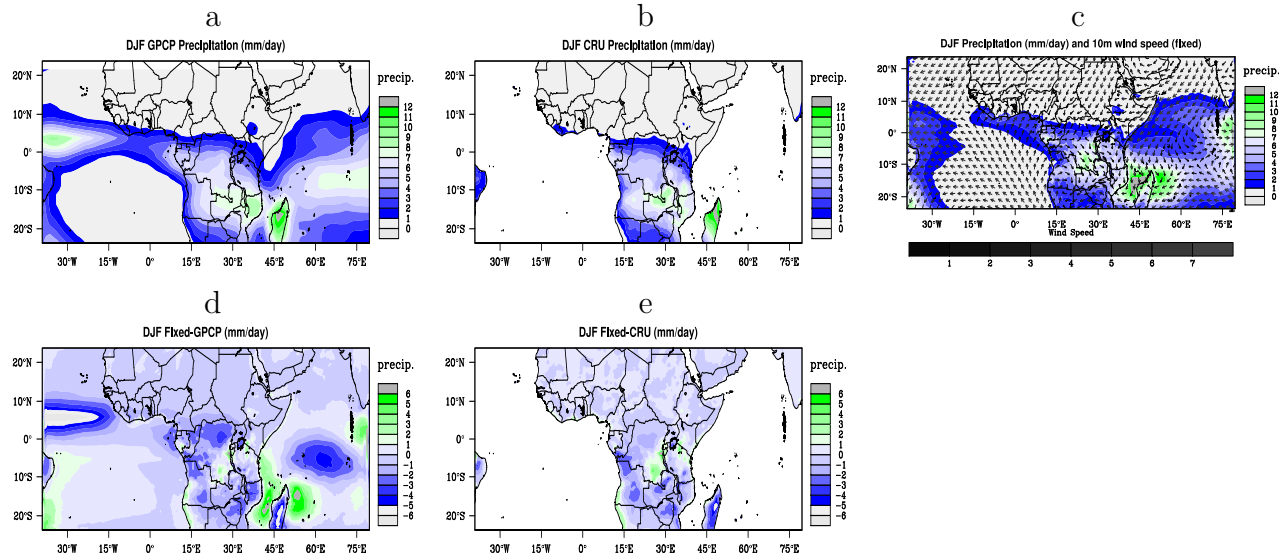

Figure 5.20: The DJF Mean 1989-2008 rainfall from GPCP (a), CRU (b), fixed (c), fixed minus GPCP differences (d), and fixed minus CRU difference (e)

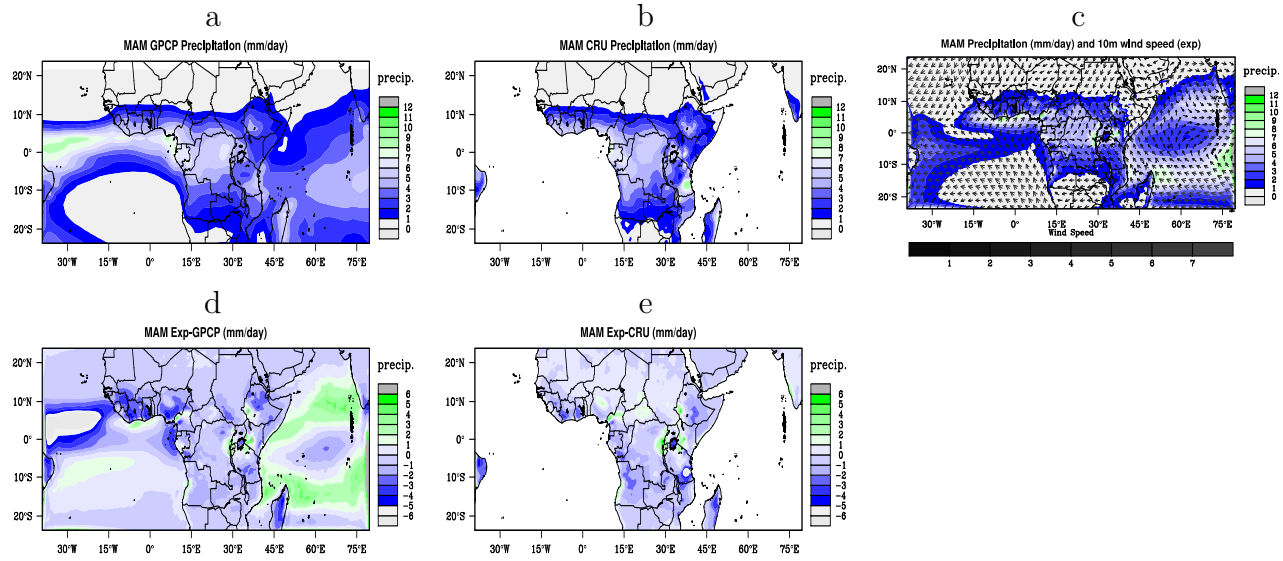

Figure 5.21: The MAM Mean 1989-2008 rainfall from GPCP (a), CRU (b), exponential (c), exponential minus GPCP differences (d), and exponential minus CRU difference (e)

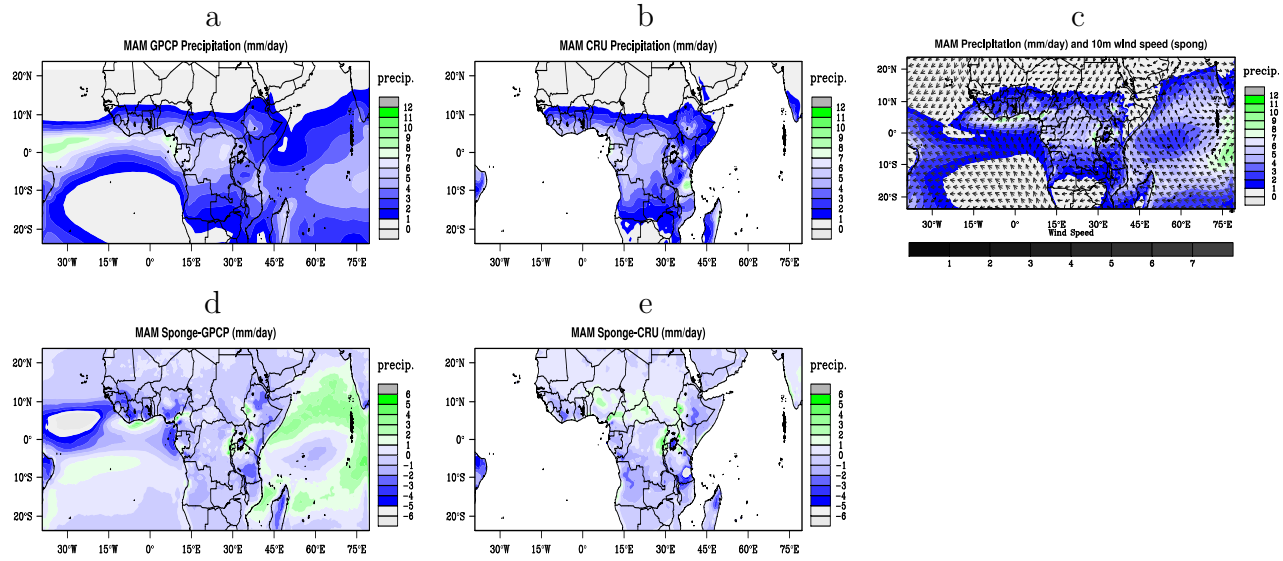

Figure 5.22: The MAM Mean 1989-2008 rainfall from GPCP (a), CRU (b), sponge (c), sponge minus GPCP differences (d), and sponge minus CRU difference (e)

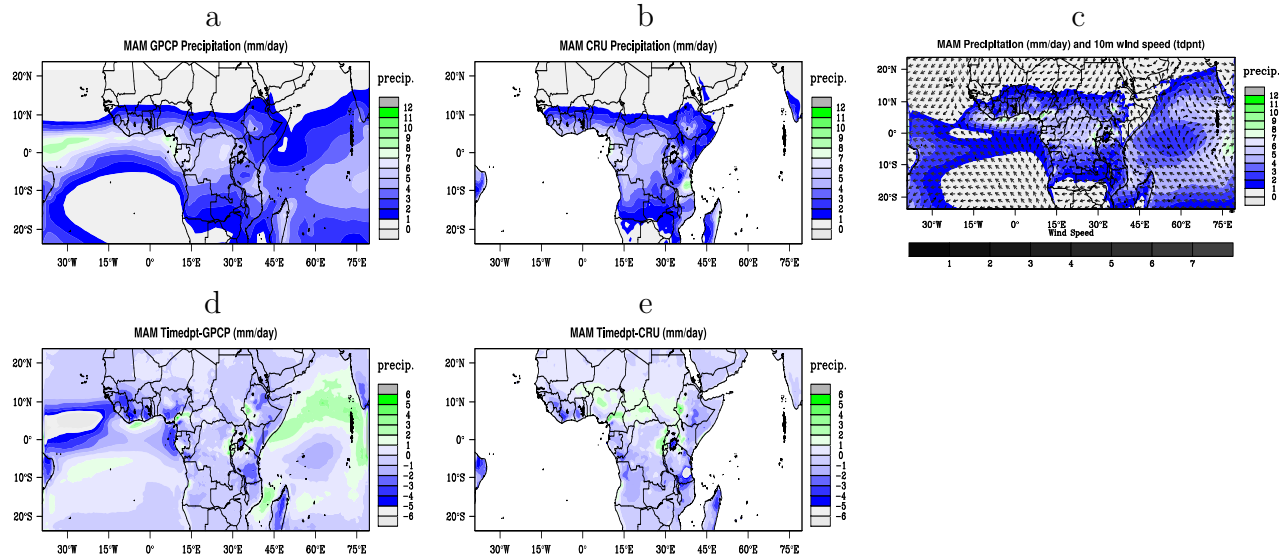

Figure 5.23: The MAM Mean 1989-2008 rainfall from GPCP (a), CRU (b), time dependent (c), time dependent minus GPCP differences (d), and time dependent minus CRU difference (e)

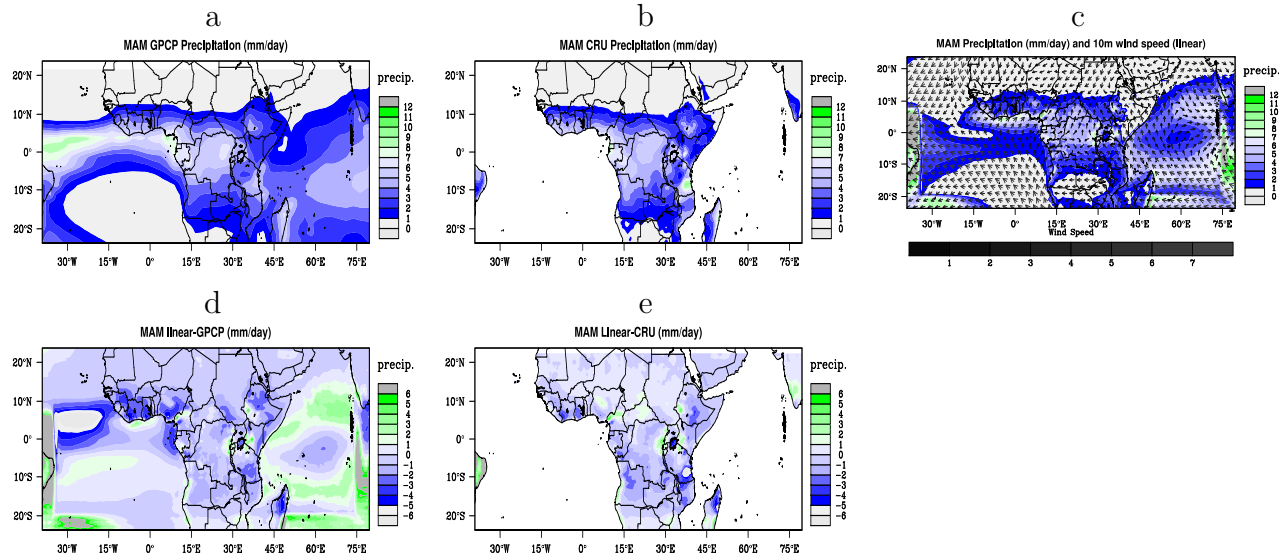

Figure 5.24: The MAM Mean 1989-2008 rainfall from GPCP (a), CRU (b), linear (c), linear minus GPCP differences (d), and linear minus CRU difference (e)

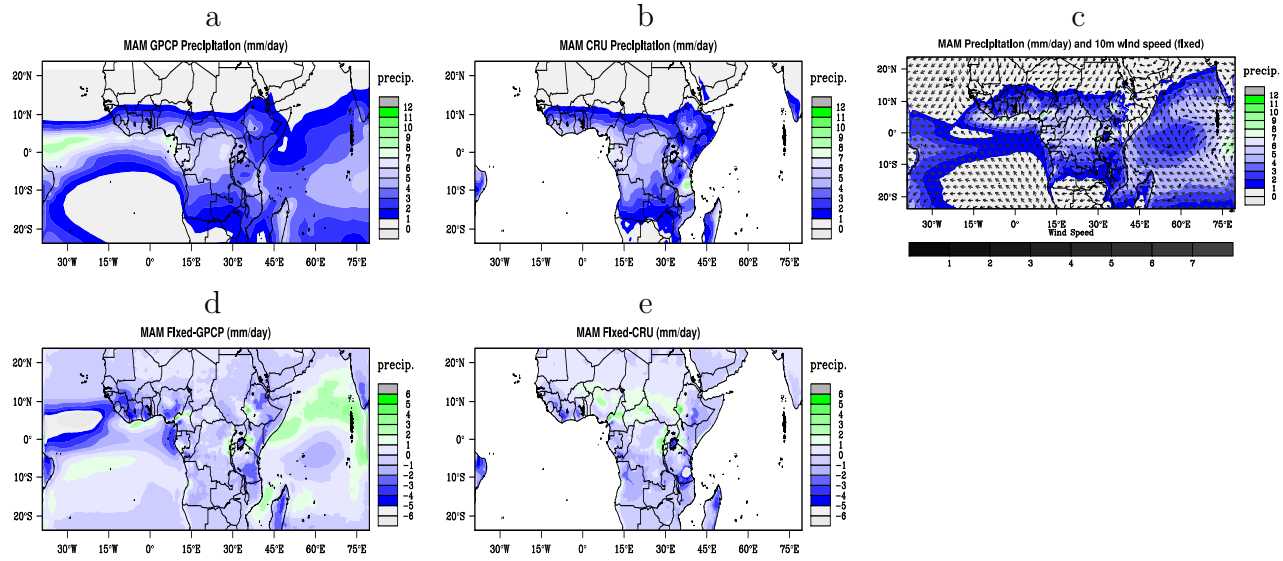

Figure 5.25: The MAM Mean 1989-2008 rainfall from GPCP (a), CRU (b), fixed (c), fixed minus GPCP differences (d), and fixed minus CRU difference (e)

the convergence zone of the Atlantic ocean. The exponential and sponge LBSs show a relatively good performance in reproducing the observed rainfall especially over the convergence zone of Atlantic ocean. In addition to the seasonal mean spatial distribution, the season mean spatial differences has shown good performance with slight underestimation and overestimation that may arise due to the complex orographic features and mesoscale convections that are difficult to capture with a 60km horizontal resolution.

5.2 Temporal Variability of Rainfall

5.2.1 Mean Annual Cycle

This section describes the mean annual cycles of RegCM4 simulated rainfall climatologies over each subregions of east Africa shown in Fig. 4.2b. The simulated rainfall climatologies have been compared with observed GPCP and CRU rainfall climatologies. The annual cycle values are averaged for each sub-region of east Africa over the whole simulation and observation periods.

Both GPCP and CRU annual cycle peaks in August over cluster 1 through 4 defined in fig. 5.26 a - d respectively. All RegCM4 simulations reproduce the observed peak in August (except cluster 1) but RegCM4 tends to under-predict its magnitude. RegCM4 reproduces the observed annual cycle over cluster 4 (Fig. 5.26d) with slight difference in magnitude.

Over cluster 5 (Fig. 5.26e), GPCP annual cycle peaks in July but CRU and all RegCM4 simulations annual cycle peaks in August. Fig. 5.26e shows that, cluster 5 has long rainy season that ranges from May-October. During this long rainy season, RegCM4 simulations over-predict with significant difference in magnitude as compared to both observations, while for the remaining seasons, RegCM4 under-predicts with slight difference in magnitude relative to GPCP and in good agreement with CRU. The same features is found over cluster 6 (Fig. 5.26f), except GPCP and CRU annual cycle peak shift to August and that of RegCM4 simulations shifts to September with overall long rainy season spanning April-October. Over this subregion, the RegCM4 simulations captured very well the observed CRU rainfall during May-September rainy season.

According to GPCP mean annual cycle, clusters 7 (Fig. 5.26g), 9 (Fig. 5.26i), and 10 (Fig. 5.26j) show the first mean peak value in April and the second peak in November

while CRU shows its peak value at different month but in the same season except that it shows the second peak in December over cluster 7. In general, all this clusters are characterized by a bimodal rainy season during MAM and SON. RegCM4 simulations in Fig. 5.26g and Fig. 5.26i reproduce the observed mean annual cycle very well with slight underestimation during MAM and overestimation during JJA and SONwith respect to GPCP, but these simulations reproduce the CRU rainfall more accurately. Although RegCM4 simulations in Fig. 5.26j reproduce the observed mean annual peaks during MAM and SON (especially the CRU annual trend), it underestimates for both seasons. Among this clusters, cluster 9 (Fig. 5.26i) shows a relatively moderate mean annual rainfall pattern. Similarly, cluster 11 (Fig. 5.26k) shows a bimodal observed rainfall characteristics during MAM and SON with the first maximum peaks in may and the second in October. Although RegCM4 simulations reproduce the first and the second annual peaks during MAM and SON, simulations from time dependent and sponge LBSs tends to produce a trimodal trend. The bimodal structure of rainfall is associated with a northsouth oscillation of the ICTZ.

Cluster 8 (Fig. 5.26h) is the only east African subregion characterized by a single rainy season during DJF. Over this subregion, RegCM4 underestimates during January-July and overestimates during September-December relative to GPCP and underestimates over the whole year relative to CRU.

Overall, RegCM4 simulations from all LBSs perform well in reproducing the observed seasonal cycle of rainfall over most east African subregions, except for a strong underestimates of the magnitude of the peak over clusters 1, 2, and 3. The mean annual cycle of RegCM4 simulations are found to be capable of producing phases and magnitudes of peak mean annual cycles of both GPCP and CRU very well.

5.2.2 Inter-annual variability

Because of its complex terrain, land-cover and vegetation, East Africa is characterized by a large spatial inter-annual rainfall variability, with rainfall patterns sometimes varying within very short distances. To examine this inter-annual rainfall variability over such complex regions, different mechanisms has been employed. Fig. 5.27 compares the simulated and observed (CRU and GPCP) inter-annual rainfall climatology over all the eleven homogeneous climate subregions to evaluate the ability of RegCM4 to capture the unique

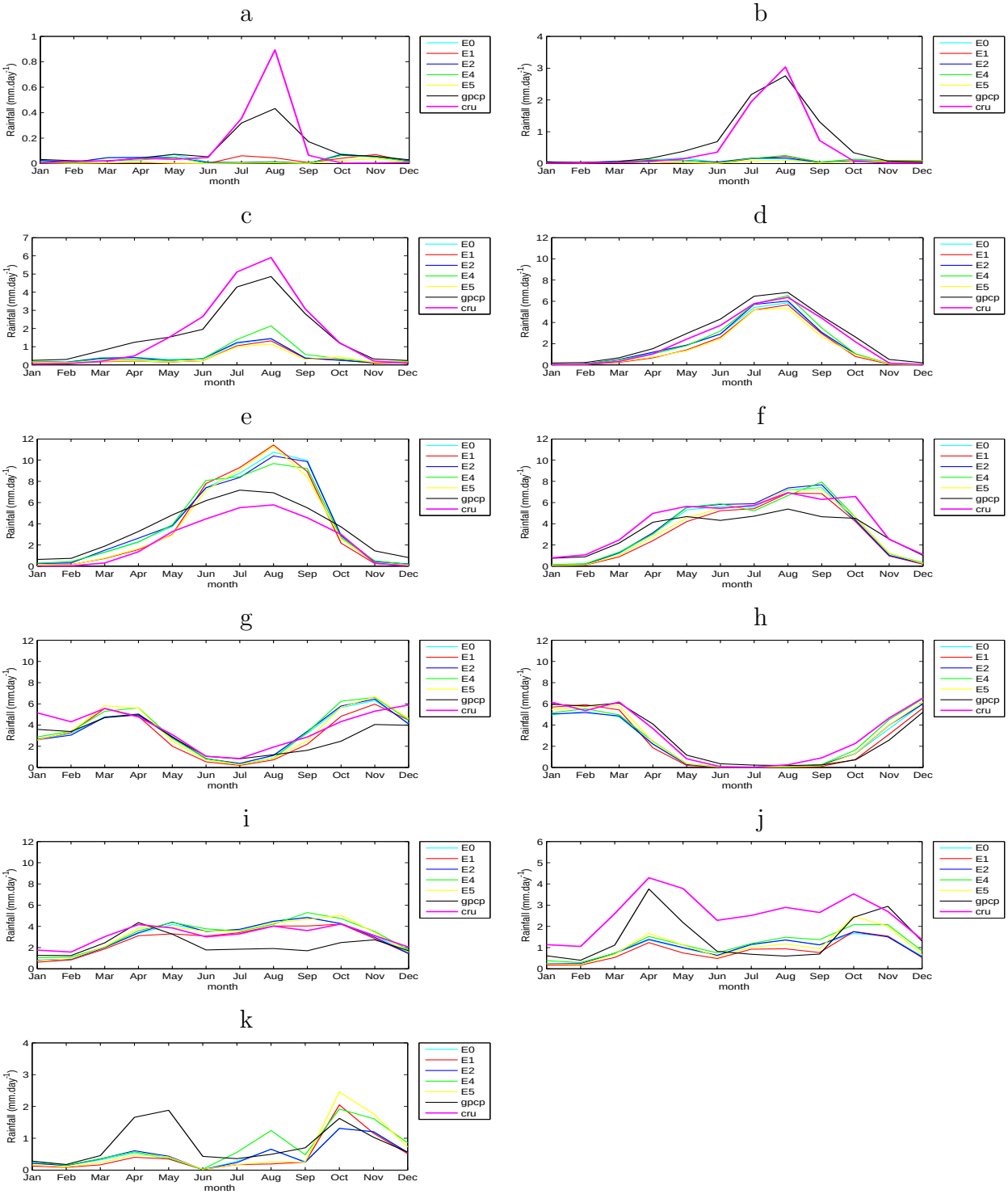

Figure 5.26: Mean annual cycle of rainfall climatology over cluster1 (a), cluster2 (b), cluster3 (c), cluster5 (d), cluster6 (e), cluster7 (f), cluster8 (g), cluster9 (h), cluster10 (i), and cluster11 (k)

spatial characteristics of rainfall over East Africa. The model climatology is derived from 20 years (1989-2008) of RegCM4 simulations. Similarly the observed (CRU and GPCP) climatologies are derived over the same period. The homogeneous climate sub_regions are used for cluster analysis to demarcate East Africa into eleven homogeneous climate sub_regions. The eleven sub_regions selected for our model evaluation are shown in Fig. 4.2b. The spatial averages are derived from the 1989-2008 time series (see Fig. 5.27). Table 5.1 summarizes the correlation coefficients, correlation significance error, RMSE, and bias with respect to GPCP for each LBSs over each subregions respectively, which is taken as a measure of inter-annual rainfall variability. Fig. 5.28 also shows the variation of the correlation coefficients (upper left panel), correlation significance error (upper right panel), RMSE (lower left panel), and bias (lower right panel) with respect to GPCP for each LBSs across the climate sub_regions of East Africa respectively.

In clusters one, two, nine, ten, and eleven the simulated inter-annual rainfall variability poorly agree with observations for all LBSs with correlation coefficients below 0.5 with respect to GPCP except that, the linear relaxation LBS has a correlation coefficient 0.57 over cluster two. Over these sub-regions the simulated rainfall captures a negative (dry) bias except that over cluster ten exhibits a wet bias. Especially, over cluster one, the statistical results obtained are less significant. However, the model fairly reproduces the observed inter-annual rainfall variability over the remaining clusters for all LBSs with correlation coefficients above 0.6 (see Table 5.1). Among these sub-regions, cluster three, four, and eight show a dry bias whereas regions five, six, and seven produce a wet bias, although linear relaxation LBS has a dry bias over cluster six. From all sub-regions, cluster five shows a relatively high RMSE. The statistical results over all these sub-regions are highly significant.

The failure of the model to consistently reproduce the observed rainfall variability over these clusters may be attributed to a number of factors, such as inadequate representation of land and ocean surface processes, deficiency in the model's convection, clouds and radiation physics parameterizations; problems associated with the vertical coordinate system (σ-p coordinates) in representing the sharply changing complex topographical features. Also the 60-km spatial resolution used in the present study may not be possibly fine enough to effectively capture the spatial and temporal structure of precipitation over the complex and steep escarpments over complex terrain.

Inorder examine the effectiveness of the LBSs used in this study in reproducing the observed rainfall variability, the model variables of each LBSs has been compared relative to each other, taking the observed variables as a reference. As Table 5.1 and Fig. 5.28 show, the simulated rainfall has been examined with respect to GPCP. The statistical values over the eleven subregions have different values for different LBSs. For example, the linear flow relaxation LBS has an overall good correlation coefficients with high significant level over all the elven clusters. This LBS also shows a dry bias over most sub-regions. Similarly, the sponge and exponential LBSs also show good agreement with the observed, except the correlation over cluster one is less significant.

Overall, Figs. 5.27 - 5.28, and Tables 5.1 indicate that, except for a few cases, all the LBSs are able to reproduce the observed inter-annual rainfall variability. However, a few exceptions occur, especially over north Sudan, south-east Ethiopia, and the Somalia regions where the correlations are relatively low. For a large domain such as the one used here, the boundary forcing may not be strong near these regions and local model-simulated processes may become dominant. Although the correlations are low, the spatial distribution of rainfall is in line with that of the other regions, indicating that there is relative differences.

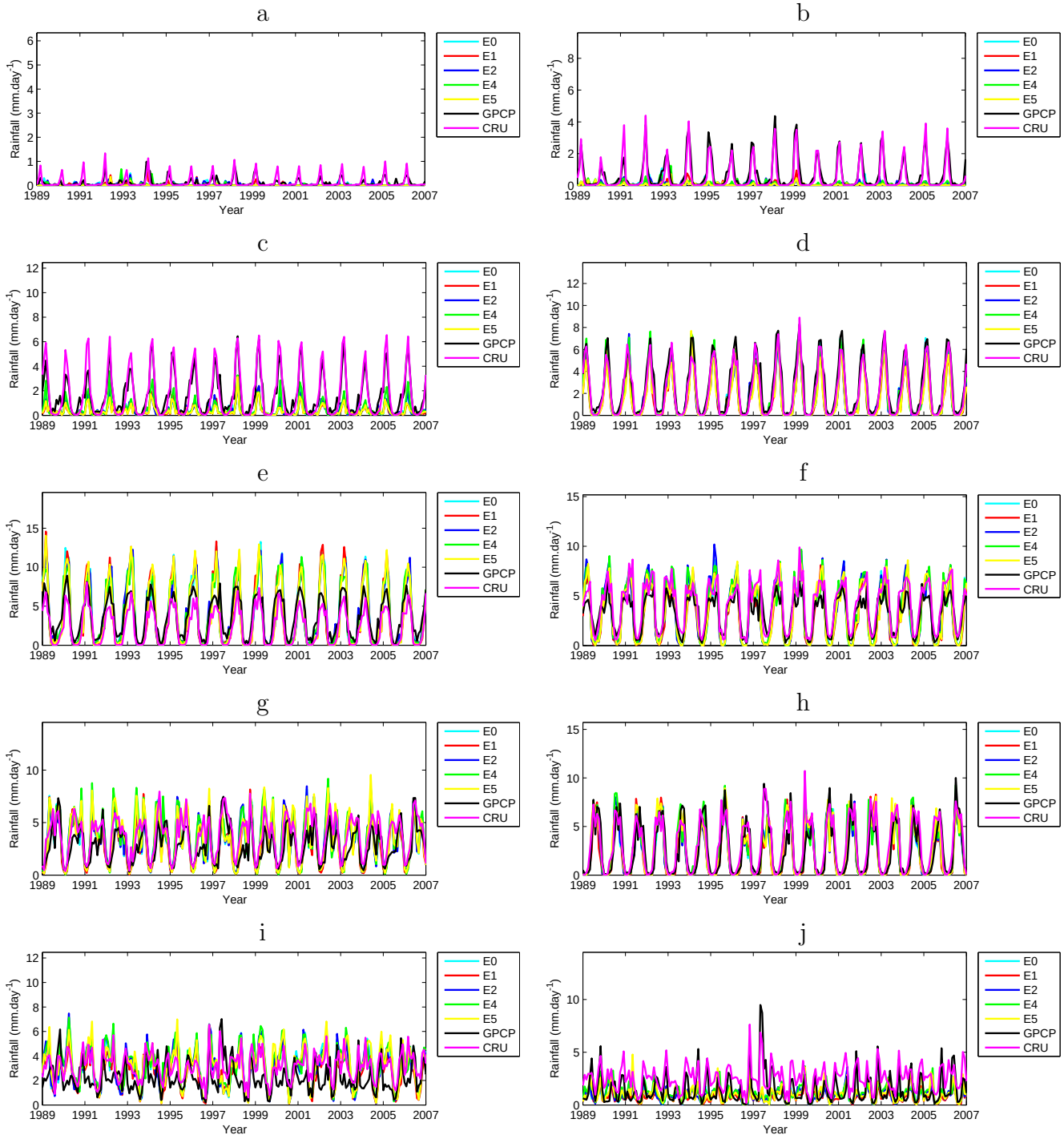

Figure 5.27: Mean inter-annual variability of rainfall climatology over cluster1 (a), cluster2 (b), cluster3 (c), cluster5 (d), cluster6 (e), cluster7 (f), cluster8 (g), cluster9 (h),and cluster10 (i)

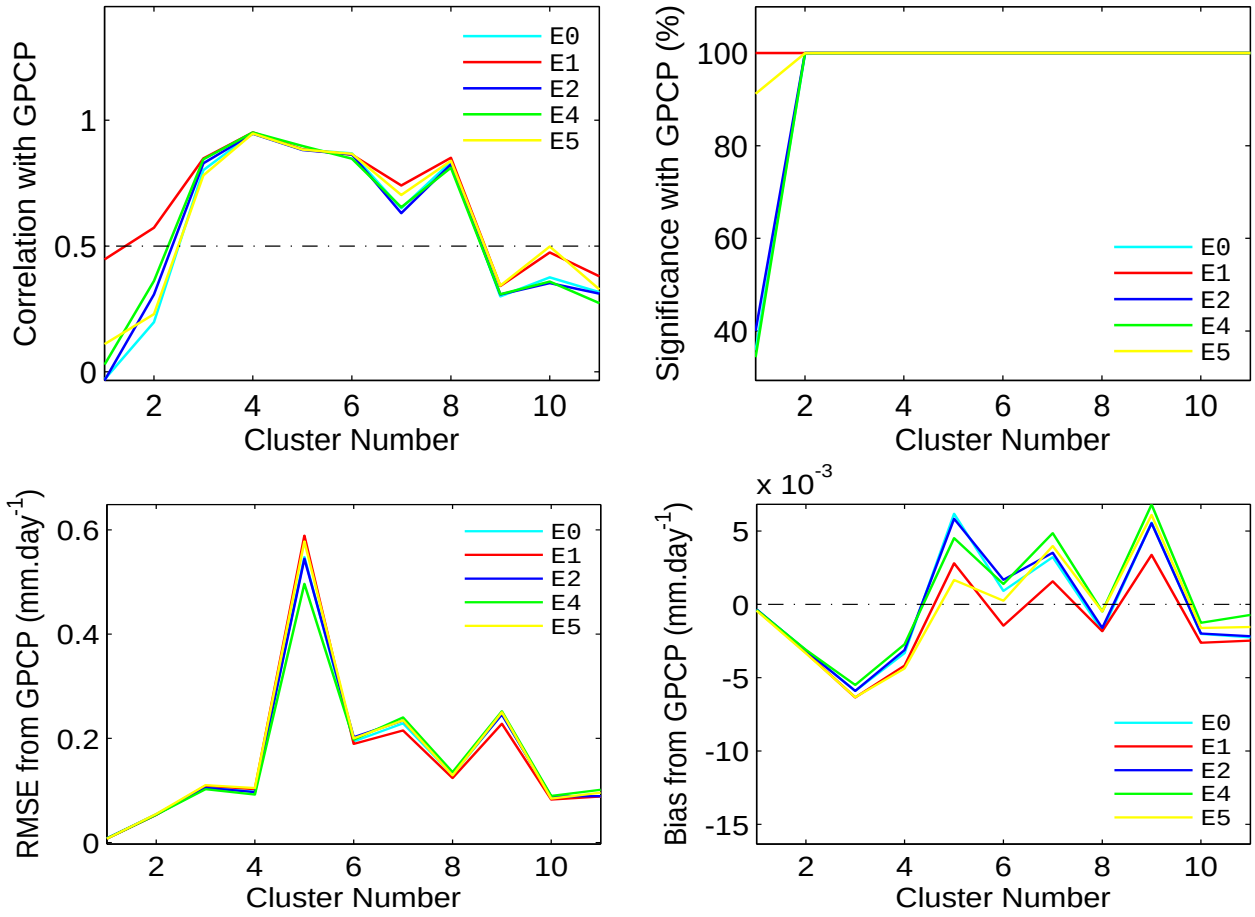

Figure 5.28: Representation of Correlation coefficients, Significance, RMSE, and Bias of RegCM4 simulation with respect to GPCP in each sub-region

Cluster Statistics with GPCP											
	1	2	3	4	5	6	7	8	9	10	11
	Correlation										
E0	-0.030	0.198	0.802	0.948	0.884	0.868	0.650	0.835	0.300	0.376	0.316
E1	0.447	0.573	0.848	0.951	0.885	0.864	0.741	0.851	0.341	0.475	0.380
E2	-0.034	0.307	0.829	0.947	0.882	0.864	0.631	0.825	0.307	0.353	0.311
E4	0.029	0.361	0.845	0.952	0.898	0.847	0.654	0.812	0.308	0.358	0.273
E5	0.110	0.229	0.781	0.947	0.884	0.867	0.703	0.839	0.342	0.498	0.327
	Significance										
E0	0.358	0.998	1.000	1.000	1.000	1.000	1.000	1.000	1.000	1.000	1.000
E1	1.000	1.000	1.000	1.000	1.000	1.000	1.000	1.000	1.000	1.000	1.000
E2	0.401	1.000	1.000	1.000	1.000	1.000	1.000	1.000	1.000	1.000	1.000
E4	0.344	1.000	1.000	1.000	1.000	1.000	1.000	1.000	1.000	1.000	1.000
E5	0.912	1.000	1.000	1.000	1.000	1.000	1.000	1.000	1.000	1.000	1.000
	RMSE										
E0	0.008	0.054	0.106	0.097	0.548	0.194	0.229	0.130	0.246	0.088	0.088
E1	0.007	0.053	0.109	0.102	0.589	0.189	0.215	0.124	0.228	0.083	0.088
E2	0.008	0.054	0.105	0.097	0.545	0.202	0.234	0.133	0.246	0.088	0.089
E4	0.008	0.054	0.103	0.092	0.496	0.198	0.240	0.135	0.252	0.089	0.101
E5	0.007	0.055	0.110	0.105	0.578	0.200	0.234	0.129	0.250	0.084	0.096
	Bias										
E0	-0.000	-0.003	-0.006	-0.003	0.006	0.001	0.003	-0.002	0.006	-0.002	-0.002
E1	-0.000	-0.003	-0.006	-0.004	0.003	-0.001	0.002	-0.002	0.003	-0.003	-0.002
E2	-0.000	-0.003	-0.006	-0.003	0.006	0.002	0.004	-0.002	0.006	-0.002	-0.002
E4	-0.000	-0.003	-0.006	-0.003	0.005	0.001	0.005	-0.000	0.007	-0.001	-0.001
E5	-0.000	-0.003	-0.006	-0.004	0.002	0.000	0.004	-0.000	0.006	-0.002	-0.002

Table 5.1: Correlation coefficients, Significance, RMSE, and Bias of RegCM4 simulation with respect to GPCP in each sub-region

Chapter 6

Conclusion

In this study the performance of RegCM4 LBSs are evaluated in reproducing the observed rainfall climatology of mean, seasonal and annual cycle, and inter-annual variability over a large domain covering most of the African continent, with the model being driven by the recently produced ERA-interim reanalysis dataset. The results from each LBSs are analyzed spatially over the whole domain and averaged over east Africa for elven climate sub-regions shown in Fig. 4.2b. The domain used in this study is set large which allows more freedom for the regional model to produce its own circulations and it reduces the strength of disturbances from the lateral boundaries, especially in the middle of the domain.

Simulated mean and seasonal mean rainfall climatologies are generally consistent with observations. RegCM4 captures the spatial variability of rainfall, the northsouth migration of the ITCZ and the associated low level circulation. Maxima are well represented over complex terrains, although the model tends to overestimate rainfall over tropical high elevation mountain areas. The regional model tends to overestimate rainfall over south Sudan and Ethiopian highlands in JJA and over the equatorial tropical forest in SON. RegCM4 also overestimates over east African highlands in MAM.

The mean annual cycles over different climate subregions show that the equatorial regions are characterized by two rainy seasons associated with the northsouth migration of the ITCZ (clusters seven, nine, ten, and eleven), while the regions far away from the equator have only one rainy season related to the onset and evolution of regional monsoon circulations. RegCM4 reproduces well the amplitude and phase of rainy and dry seasons for all the subregions except for a few cases when the magnitude of the

peaks is overestimated. In particular, the regional model is shown to perform better over sub-region four than the remaining sub-regions in reproducing the observed mean annual rainfall climatology over the entire months consistently.

Finally, the RegCM4 simulation captures relatively well the inter-annual rainfall variability over most subregions analyzed, both in terms of statistical values and individual time series with an exceptions over subregion one where the correlations with observed rainfall climatology and the corresponding significance levels are low, but the errors of statistical variability is also low. This might be due to the local model processes which perform the most important aspect than the lateral boundary forcing and LBSs in determining the rainfall variability.

Overall, the simulation analysed here indicates a relatively good performance of the RegCM4 over a large African domain encompassing most of the African continent and adjacent oceans. Part of this relatively good performance may be due to the use of ERA-interim to produce improved lateral boundary conditions. Choice of domain, convection scheme and some parameter values also contributed to this improvement. An important point regarding model validation is that two different observational datasets (one from GPCP which has coarse resolution and the second from CRU which is highly resolved) is used. In most areas the simulated rainfall climatologies show a good level of agreement (especially with the CRU), but in some areas they show a relatively wide spread (especially over subregion one and two). However, the Sponge as well as exponential LBSs reproduce the observed rainfall climatology very well, although there some deficiencies. This might be due to a substantial uncertainty in observed estimates of rainfall which should be taken into account when evaluating climate models over the African continent.

References

Adler, R.F., Huffman, G.J., Chang, A., Ferraro, R., Xie, P., Janowiak, J., Rudolf, B., Schneider, U., Curtis, S., Bolvin, D., Gruber, A., Susskind, J., Arkin, P. & Nelkin, E. (2003). The version-2 global precipitation climatology project (gpcp) monthly precipitation analysis (1979-present). *J. Hydrometeor.*, **4**. 3, 35

Anthes, R.A. (1977). A cumulus parameterization scheme utilizing a one dimensional cloud model. *Department of Meteorology, The Pennsylvania State University,University of Park 16802*, **105**. 24

Anyah, R.O. & Semazzi, F.H.M. (2007). Variability of east african rainfall based on multiyear regcm3 simulations. *International Journal of Climatology*. 1, 2

Bowden, J.H. & Semazzi, F.H.M. (2007). Empirical analysis of intraseasonal climate variability over the greater horn of africa. 1

Briegleb, B.P. (1992). Delta-eddington approximation for solar radiation in the ncar community climate. *J. Geophys. Res.*, **97**. 24

Davies, H.C. (1983). Limitation of some common lateral boundary schemes used in regional nwp models. *Laboratory atmospheric physics ETH, Honggerberg,8093 Zurich*, **111**. 2, 41

Davis, N., Bowden, J., Semazzi, F., Xie, L. & Onol, B. (2009). Customization of regcm3 regional climate model for eastern africa and a tropical indian ocean domain. *American Meteorological Society*, **22**. 1, 2, 34

Dickinson, R., Henderson-Sellers, A. & Kennedy, P. (1993). Biosphere-atmosphere transfer scheme (bats) version 1e as coupled to the ncar community climate model. *National center for atmospheric research, Boulder, Colorado*. 24, 33

Dickinson, R.E., Kennedy, P.J., Henderson-Sellers, A. & Wilson, M. (1986). Biosphere-atmosphere transfer scheme (bats) for the ncar community climate model,. *Tech. Rep. NCARE/TN-275+STR, National Center for Atmospheric Research.*. 23, 24

Dickinson, R.E., Errico, R.M., Giorgi, F. & Bates, G.T. (1989). A regional climate model for the western united states. *Climatic Change*, **15**. 23

Diffenbaugh, N.S. (2009). Influence of modern land cover on the climate of the united states. *Purdue Climate Change Research Center, Purdue University*. 1

Emanuel, K.A. (1991). A scheme of representing cumulus convection in large-scale models. *Center for meteorological and physical oceanography, Massachusetts institute of technology, cambridge, Massachusetts*. 25

Emanuel, K.A. & Zivkovic-Rothman, M. (1999). Development and evaluation of a convection scheme for use in climate models. *Atmospheric and Environmental Research, Inc., Cambridge, Massachusetts*, **56**. 25

Fritsch, J.M. & Chapell, C.F. (1980). Numerical prediction of convectively driven mesoscal pressure systems. part2: Mesoscale model. *Atmospheric physics and Chemistry Laboratory, NOAA, Boulder, CO 80303*, **37**. 34

Gianotti, R.L., Zhang, D. & Eltahir, E.A.B. (2012). Assessment of the regional climate model version 3 over the maritime continent using different cumulus parameterization and land lurface schemes. *Journal of Climatology*, **25**. 2

Giorgi, F. (1989). Two-dimensional simulations of possible mesoscale effects of nuclear war fires. *J. Geophys.Res.*, **94**. 23

Giorgi, F. (1990). Simulation of regional climate using a limited area model nested in general circulation model. *National center for atmospheric research, Boulder, Colorado*. 23

Giorgi, F., Marinucci, M.R. & Bates, G.T. (1993). Development of a second generation regional climate model (regcm2). part2: Convective processes and assimilation of lateral boundary conditions. *National center for atmospheric research, Boulder, Colorado*, **121**. 40, 41

Giorgi, F., T.Bates, G. & Nieman, S.J. (1993a). The multiyear surface climatology of a regional atmospheric model over the western united states. *National center for atmospheric research, Boulder, Colorado*, **6**. 23, 24

Giorgi, F., T.Bates, G. & Marinucci, M.R. (1993b). Development os a second-generation regional climate model (regcm2). part1:boundary-layer and radiative transfer process. *National center for atmospheric research, Boulder, Colorado*, **121**. 23, 24

Giorgi, F., Francisco, R. & Pal, J. (2003b). Effects of a subgrid-scale topography and land use scheme on the simulation of surface climate and hydrology. part i: Effects of temperature and water vapor disaggregation. *Abdus Salam International Centre for Theoretical Physics, Trieste, Italy*, **4**. 25

Grell, G.A. (1993). Prognostic evaluation of assumption used by cumulus parameterizations. *National center for atmospheric research, Boulder, Colorado*, **121**. 24

Grell, G.A., Dudhia, J. & Stauffer, D.R. (1994). A description of the fifth-generation penn state/ncar mesoscale model (mm5). *National center for atmospheric research, Boulder, Colorado*. 23, 24, 26, 33, 34

Hack, J.J., Boville, B.A., Briegleb, B.P., Kifhi, J., Rasch, P.J. & Williamson, D.L. (1993). Description of the ncar community climate model (ccm2). *National center for atmospheric research, Boulder, Colorado*. 24

Holton, J.R. (2004). *An introduction to Dynamic meteorology*. Elsevier Academic Press. 5

Holtslag, A., Bruijn, E.D. & Pan, H.L. (1990). A high resolution air mass transformation model for short-range weather forcasting. **118**. 24, 33

Hsie, E.Y., Anthes, R.A. & Keyser, D. (1984). Numerical simulation of frontogenesis in a moist air atmospher. *National center for atmospheric research, Boulder, Co 80307*, **41**. 24

Huffman, G.J., Adler, R., Bolvin, D.T. & Gu, G. (2009). Improving the global precipitation record: Gpcp version 2.1. *Geophys. Res. Lett.*, **36**. 3, 35

Jacobson, M.Z. (2005). *Fundamentals of atmospheric modeling*. Cambridge University Press,, New York. 5

Kiehl, J.T., Hack, J.J., Bonan, G.B., Boville, B.A., Briegleb, B.P., Williamson, D.L. & Rasch, P.J. (1996). Description of the ncar community climate model (ccm3). *National Center For Atmospheric Research Boulder, Colorado*. 24, 33

Lavelle, J. & Thacker, W. (2008). A pretty good sponge: Dealing with open boundaries in limited-area ocean models. *Ocean Modelling 20 270292*. ix, 2, 37, 38, 40

Marbaix, P., Gallee, H., Brasseur, O. & Ypersele, J.P.V. (2003). Lateral boundary conditions in regional climate models: A detailed study of the relaxation procedure. **131**. 3, 40, 41

Pal, J.S., Small, E.E. & Eltahir, E.A.B. (2000). Simulation of regional-scale water and energy budgets: Representation of subgrid cloud and precipitation processes within regcm. **105**. 25, 33

Perkey, D.J. & Kreitzberg, C.W. (1976). A time dependent lateral boundary scheme for limited-area primitive equation models. *Drexel university, Philadelpkia, Pa. 19104*, **104**. 36

Reynolds, R. & Smith, T. (1994). Improved global sea surface temperature analyses using optimum interpolation. *J Climate*, **7**. 35

Richardson, M.I., Toigo, A.D. & Newman, C.E. (2007). Planetwrf: A general purpose, local to global numerical model for planetary atmospheric and climate dynamics. *Journal of Geophysical Reserch*, **112**. 29

Segele, Z.T., Leslie, L.M. & Lamb, P.J. (2008). Evaluation and adaptation of a regional climate model for the horn of africa: rainfall climatology and interannual variability. 1, 42

Sylla, M.B., Coppola, E., Mariotti, L., Giorgi, F., Ruti, P.M., DellAquila, A. & Bi, X. (2009). Multiyear simulation of the african climate using a regional climate model (regcm3) with the high resolution era-interim reanalysis. 1, 2, 35

Tchotchou, L.A.D. & Kamga, F.M. (2009). Sensitivity of the simulated african monsoon of summers 1993 and 1999 to convective parameterization schemes in regcm3. 3, 35

Willmott, C.J., Ackleson, S.G., Davis, R.E., Feddema, J.J., Klink, K.M., Legates, D.R., O'Donnel, J. & Rowe, C.M. (1985). Statistics for the evaluation and comparison of models. 42

Zeng, X., Zhao, M. & Dickinson, R.E. (1998). Intercomparison of bulk aerodynamic algorithms for the computation of sea surface fluxes using toga coare and tao data. *Institute of Atmospheric Physics, The University of Arizona, Tucson, Arizona*, **11**. 25, 33

Declaration

This thesis is my original work, has not been presented for a degree in any other University and that all the sources of material used for the thesis have been fully acknowledged.

Name: **Tamene Mekonnen**

Signature:

Place and time of submission: Addis Ababa University, June 2012

This thesis has been submitted for examination with my approval as University advisor.

Name: **Dr. Gizaw Mengitu**

Signature: